Doctoral Dissertation

博士論文

# Studies on Abundance and Emission Strengths of Anthropogenic Iron Oxide Aerosols Using Laser-Induced Incandescence Technique

（レーザー誘起白熱法を用いた人為起源酸化鉄エアロゾルの大気中の動態研究及び排出強度推定）

A Dissertation Submitted for the Degree of Doctor of Philosophy

December 2019

令和元年 12 月博士（理学）申請

Department of Earth and Planetary Science, Graduate School of Science,
The University of Tokyo

東京大学理学系研究科

地球惑星科学専攻

Atsushi Yoshida

吉田 淳

# Abstract

Iron-containing aerosols in the atmosphere are considered to play important roles in the Earth's climate. They absorb solar radiation as black carbon (BC) and brown carbon (BrC) do, resulting in a positive radiative forcing. Irons in aerosols are also an essential nutrient for phytoplankton and their deposition to the surface ocean is considered to affect the carbon cycle through the absorption of carbon dioxide into the ocean. Thus, iron aerosols affect the climate on both short time scales as light-absorbers and long time scales as nutrient sources for the ocean ecosystem.

It has been considered that mineral dust emitted from the arid area is a main component of atmospheric iron aerosols. Recently, the existence of anthropogenic iron aerosols such as fuel combustion has been reported. However, the abundance and behaviors of anthropogenic iron aerosols in the atmosphere, as well as their radiation effects have not been examined due to a lack of reliable observations. In most of the previous studies, iron aerosols were measured by the collection of particles on filers and subsequently analyzed in laboratories. Although these methods provide useful information on the chemical component and shape of iron aerosols, they cannot provide concentrations and size distributions with a sufficiently high time resolution that is required for statistical analyses. As a consequence, emission inventories of anthropogenic aerosols, that are required to evaluate their impacts on the climate, are compiled only by accumulating from individual emission sources (bottom-up method) and they are considered to have significant uncertainties. To improve the emission inventories, reliable and statistically enough observational data that can constrain the emission strength (top-down method) are needed.

In this study, I developed a new technique to measure light-absorbing iron oxide particles ($FeO_x$) including magnetite and hematite using a laser-induced incandescent (LII) technique. In this technique, a mass of individual $FeO_x$ particles (170-2100 nm) can be quantified by

measuring the incandescence light emitted from the particle in the laser beam. Furthermore, the scattering cross section and the position where the incandescence starts in the laser beam (incandescence onset position) are measured to evaluate the mixing state of $FeO_x$ aerosols with other aerosol compounds (volatile or non-volatile) and to determine $FeO_x$ chemical components (e.g., magnetite and hematite). From these information one can classify the detected $FeO_x$ particles into anthropogenic (combustion) and natural origins (mineral dust). Thus, the developed LII technique has made it possible for the first time to estimate a mass (size), size distribution, and mixing state with a high temporal resolution (1–60 mins) under typical atmospheric conditions.

Using the developed LII technique, in situ measurements of $FeO_x$ aerosols were made at Cape Hedo, Okinawa Island in April 2017. Air likely affected by sources over the Asian continent was frequently sampled due to prevailing northwesterlies. Based on the single-particles quantities measured by the LII, most of the observed $FeO_x$ aerosols were found to be anthropogenic; a number fraction of mineral dust particles (known as Kosa) was below 10% during this experiment. Temporal variation of $FeO_x$ aerosols was well captured and the statistically significant data enabled to obtain clear positive correlations between the mass concentrations of $FeO_x$ and BC ($R^2 = 0.717$) and of $FeO_x$ and CO ($R^2 = 0.718$) in air originating from China. These correlations indicate that the emission sources of $FeO_x$ aerosols are spatially similar to those of BC and CO in China.

In this study, I used the observed slope of the correlation between $FeO_x$ and BC (CO) as a scaling factor for global BC (CO) emission data in literature in order to estimate global anthropogenic iron emissions. As a result, the global emission strength of anthropogenic iron aerosols was estimated to be 1.4-3.4 FeTg/yr. This is the first estimate using the top-down method. Uncertainties in these estimates are discussed in this thesis.

In order to understand the abundance of $FeO_x$ aerosols in wide-area, I also acquired and analyzed $FeO_x$ data in East Asian (area influenced by air from the Asian continental), urban

city in Japan, and the Arctic regions. Most of the $FeO_x$ aerosols observed in these regions were anthropogenic based on the single-particles quantities measured by the LII. Among all observations, the shapes of $FeO_x$ number size distributions are similar. Mass concentrations of $FeO_x$ aerosols were 20-50% of those of BC. Furthermore, in all observations, it was found that the $FeO_x$ aerosol concentration showed a positive correlation with BC and CO. These facts suggest that the source of anthropogenic $FeO_x$ aerosols in the Northern Hemisphere likely spreads over a wide area as well as that of BC and CO.

The new method that I have developed was also applied to estimate $FeO_x$ emission sources in urban areas. As a result, the vehicle is suggested to be an important source of anthropogenic $FeO_x$ aerosols rather than steel and power plants.

The novel dataset of $FeO_x$ aerosols that I obtained in East Asia was used to constrain global model simulation for evaluating the radiative forcing of anthropogenic FeOx aerosols as well as their possible impacts on the iron supply to the ocean. In this simulation, $FeO_x$/BC mass ratio and particle size distribution obtained in the dataset were used to constrain the anthropogenic iron emissions. As a result, an atmospheric burden of anthropogenic iron aerosols was estimated to be approximately 7.7 times that estimated in the previous study. The simulation showed that a level of the radiative forcing of anthropogenic $FeO_x$ aerosols can be similar to that of BrC. In addition, the deposition flux of anthropogenic iron to the surface southern ocean was estimated to be 6.5 times of that estimated in the previous study.

To conclude, a series of reliable measurements in this study indicate that most of the light-absorbing $FeO_x$ aerosols are anthropogenic origin and they likely play more important roles for the processes related to the climate than previously thought. Further improvement of $FeO_x$ measurement techniques are important to reduce uncertainties in quantification of $FeO_x$ concentration and size distribution. In addition, further observations including ground and aircraft measurements especially in southern hemisphere are also important to understand the abundance, transport and removal of iron aerosols and their impact on climate.

# Contents

# 1 General introduction

## 1.1 Atmospheric aerosols

Atmospheric aerosols are suspensions of liquid or solid particles in a gas medium. Aerosols exhibit great variety in their microphysical properties (i.e., size, composition, and shape) depending on their source. In turn, these microphysical properties affect the optical and hygroscopic properties of individual particles. Aerosols play an important role in the climate by directly or indirectly influencing the radiative budget [IPCC 2013].

Dark-colored aerosols efficiently absorb solar radiation and heat the atmosphere. Shortwave absorption by dark aerosols also affects the formation patterns and lifetimes of clouds and thus impacts the hydrological cycle [*Menon et al.*, 2002; *Ming et al.*, 2010]. Furthermore, dark aerosols deposited onto snow and ice reduce the surface albedo [e.g., *Hansen & Nazarenko*, 2004]. Black carbon (BC), brown carbon (BrC), and iron (iron oxide) in mineral dust have been reported as major contributors to the absorption of solar radiation [*Moosmüller et al*., 2009].

Among these contributors, iron aerosols are also important in ocean biogeochemistry because iron is an essential nutrient for phytoplankton [*Martin & Fitzwater*, 1988]. The supply of iron from the atmosphere affects the primary productivity of phytoplankton in the surface ocean layers, particularly in high-nutrient low-chlorophyll regions [*Martin et al*., 1991, *Jickells et al*., 2005]. The growth of phytoplankton absorbs carbon dioxide from the atmosphere. Therefore, iron aerosols play an important role in the global carbon cycle in addition to atmospheric radiation.

## 1.2 Iron aerosols

Iron (Fe) is one of the most ubiquitous elements on Earth. Iron is found in various

materials, such as soil, rock, and coal, and is used by humans for production and power generation. Iron aerosols are emitted to the atmosphere by both natural and anthropogenic processes.

Natural Fe aerosols (mineral dust) are emitted by wind erosion (surface creep, saltation, and suspension) of soil in arid and semi-arid regions (Figure 1-1) [*Acosta-Martinez et al*., 2015]. Mineral dust contains various mineralogical forms of Fe, which are classified as structural iron and free iron (iron oxide) [*Zhang et al*., 2015]. Structural iron is trapped in the crystal lattice of aluminosilicate minerals such as feldspar and clays (e.g., biotite and illite), while iron oxide refers to discrete oxide and iron hydroxide. Sixteen distinct iron oxide components have been observed in nature [*Cornell & Schwertmann*, 2004]; however, hematite ($\alpha$-$Fe_2O_3$), goethite (FeOOH), magnetite ($Fe_3O_4$), and ferrihydrite ($5Fe_2O_3 \cdot 9H_2O$) are the primary forms of iron oxide [*Guo & Burnard,* 2013, *Formenti et al.,* 2014]. Notably, iron oxides strongly absorb visible light and are generally bound to transparent aluminosilicate (Figure 1-2).

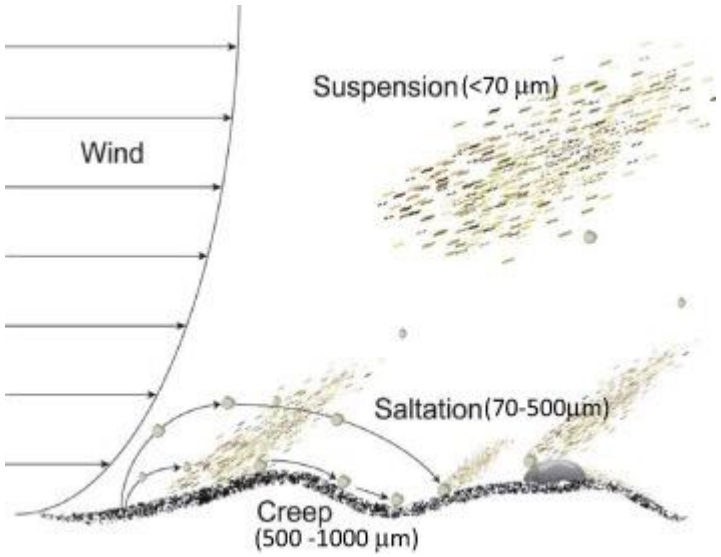


**Figure 1-1.** Mechanisms of dust emission, including suspension, saltation, and creep movement of mineral dust particles, based on the particle diameter.

Anthropogenic iron aerosols are generated in high-temperature environments through human activity [*Liati et al*., 2015, *Sanderson et al.,* 2016], crystallizing from gases, or liquids that have evaporated or melted from iron-containing material. Depending on both the source material and the environmental conditions (e.g., temperature and gas pressure), anthropogenic iron aerosols can arise as magnetite ($Fe_3O_4$), hematite ($Fe_2O_3$), ferrihydrite ($Fe_5HO_8{\cdot}4H_2O$), maghemite ($\gamma$-$Fe_2O_3$), or goethite (FeOOH) [*Magiera et al.*, 2011]. Various anthropogenic sources of iron oxide aerosols have been reported, including coal combustion [*Kutchko et al*., 2006], diesel engine combustion [*Liati et al.*, 2015], waste combustion [*Buonanno et al.*, 2011], steel manufacturing [*Machemer*, 2004], and automotive brake wearing [*Kukutschová et al.*, 2011].

Anthropogenic iron aerosols are categorized into submicron aggregated particles and super-micron spherical fly ash particles (Figure 1-3). Figure 1-4 illustrates the generation of anthropogenic iron aerosols from coal combustion. During combustion, the iron-containing vapor is emitted from combusted coal comprised of iron (e.g., iron sulfide, FeS). As these vapors cool, submicron particles or agglomerated (aggregated) particles form through nucleation, coagulation, and condensation [*Linak et al.*, 2007]. In addition, due to the shedding

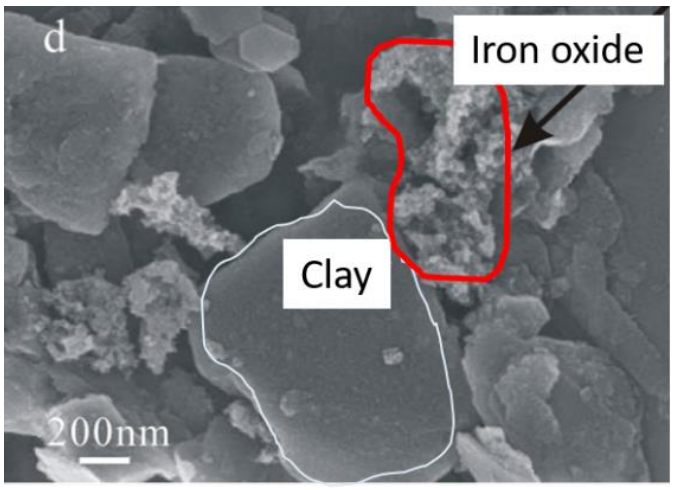


**Figure 1-2**. Scanning electron microscopy (SEM) image of a mineral dust particle consisting of clay and iron oxide [*Zhang et al*., 2015].

of fused ash and char fragmentation during combustion, large spherical fly ash particles containing aluminosilicate and iron oxide are generated [*Kutchko & Kim*, 2006]. Fly ash particles are generally created by coal combustion because coal primarily consists of aluminosilicate.

In addition to natural and anthropogenic iron aerosols, biomass burning also produces iron aerosols [*Guieu et al.,* 2005]. Biomass burning occurs both naturally (wildfire) and anthropogenically (e.g., power generation and residential use). For this reason, iron aerosols emitted from biomass combustion are not included in the natural or anthropogenic iron aerosols considered in this study.

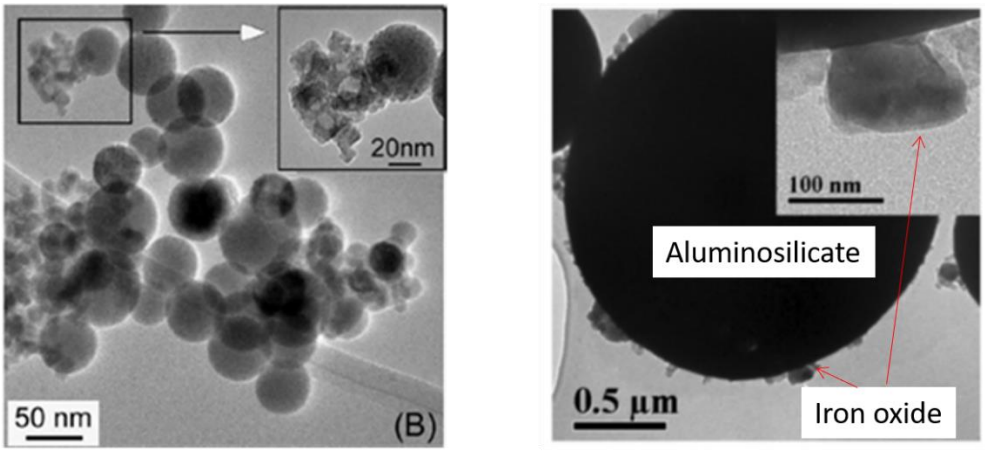


**Figure 1-3.** (Left) Transmission electron microscopy (TEM) image of magnetite nanoparticle aggregates collected from diesel exhaust [*Liati et al.*, 2015]. (Right) TEM image of a fly ash particle produced by coal combustion [*Linak et al.*, 2007].

## 1.3 Measurement of iron aerosols by filtration

Various techniques have been applied to measure iron aerosols sampled by filtration. Iron aerosols collected on filters are generally measured by off-line chemical speciation via bulk or single-particle analyses.

Using single-particle analysis with an electron microscope (e.g., TEM), the detailed structure of aerosols collected on a filter can be examined. Moreover, by coupling energy dispersive X-ray spectroscopy (EDS) with TEM, the elemental composition of a sample can be obtained. Using these techniques, aggregated iron oxide, iron fly ash, and mineral dust aerosols have been identified in the atmosphere, and iron aerosols in the exhaust of combustion sources have been evaluated (Figures 1-2, 1-3) [*Kutchko et al*., 2006, *Chen et al*., 2012, *Linak et al*., 2012, *Liati et al*., 2015, *Li et al*., 2017].

Using bulk analyses with Inductively Coupled Plasma Mass Spectrometry (ICP-MS), Particle Induced X-ray Emission (PIXE), and X-ray Fluorescence (XRF), the iron content of

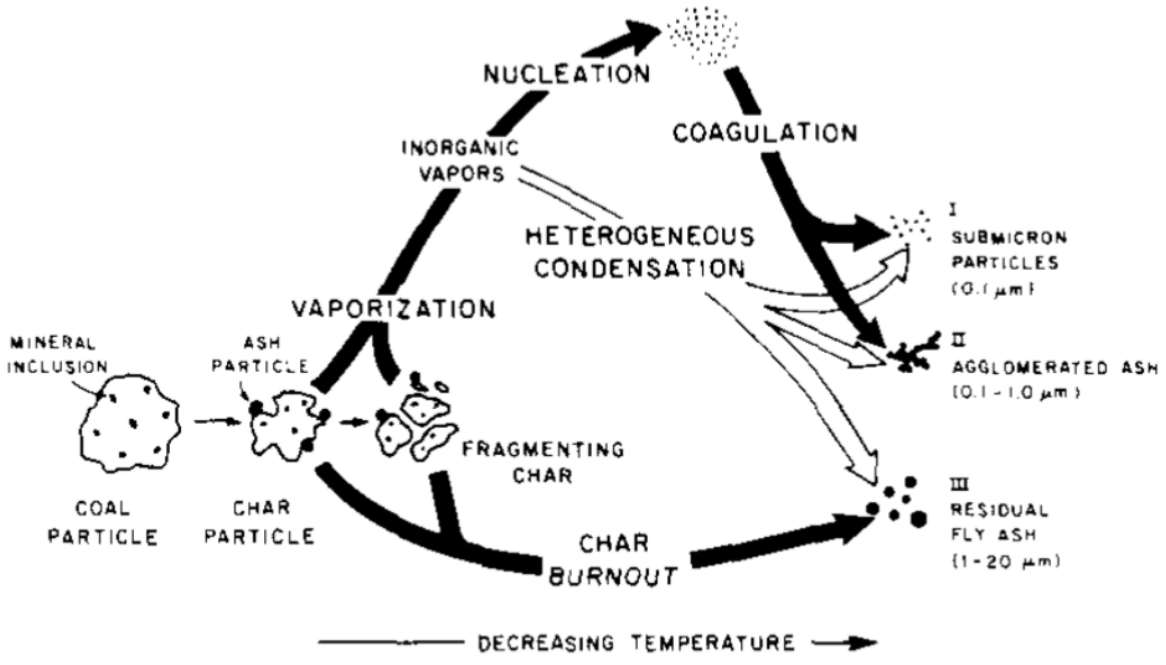


**Figure 1-4.** Particle generation by coal combustion [*Helble et al.,* 1988].

bulk aerosol samples can be measured. These bulk analysis techniques are generally used for measuring atmospheric iron concentrations [*Hsu et al*., 2010, *Xu et al,.* 2011, *Sanderson et al*., 2016]. These techniques are also used to determine the iron content of iron-containing material (e.g., soil and coal) [*Lafon et al,.* 2006, *Linke et al.,* 2006, *Tewalt et al*., 2010] and of fly ash particles created by fuel combustion [*Reddy et al*., 2005, *Vassilev et al.*, 2010], which provide the basis for emission inventories of iron aerosols (Section 1.4). By collecting size-resolved aerosols using a cascade impactor, the size distribution of iron aerosols can be measured [*Sanderson et al*. 2016]. Bulk analyses provide information regarding the quantitative abundance of iron aerosols; however, the time resolution of iron aerosol concentrations measured by filtration tends to be low (~1–10 day) due to the long sampling time required to collect a sufficient quantity of particles on the filter. For this reason, few studies have been reported on the abundance or size distribution of iron aerosols in the atmosphere compared to reports on iron particles in the exhaust of anthropogenic sources, where particles are densely distributed.

## 1.4 Emission strength and global abundance of iron aerosols

The global abundances of natural and anthropogenic iron aerosols have been estimated using aerosol transport models in order to evaluate their radiative effects and deposition flux on the surface ocean [*Luo et al,.* 2008, *Ito et al.,* 2013, *Wang et al*., 2015, *Ito et al*., 2018]. In particular, the emission strength of iron aerosols from each source is an important input parameter for the simulations. To date, bottom-up methods have been used to estimate the emission strengths of iron aerosols. For natural iron aerosols, mineralogical data maps [*Journet et al*., 2014] and local meteorological conditions (e.g., wind velocity and humidity) are combined. For anthropogenic (combustion) iron aerosols, bottom-up methods integrate emission strengths from individual sources based on the following formula [*Wang et al*., 2015]:

$$E = a \cdot b \cdot c \cdot (1 - f) \cdot \Sigma_{x=1} J_x \cdot \left[\Sigma_{y=1} A_y \cdot \left(1 - R_{x,y}\right)\right], \quad (1.1)$$

where $x$ is the particle size discretized into $n$ bins, $y$ is a specific control device (e.g., cyclone, scrubber, electrostatic precipitator), $a$ is the rate of fuel consumption, $b$ is the completeness of combustion (defined as the fraction of fuel burnt), $c$ is the Fe content of the fuel, $f$ is the fraction of Fe retained in the residual ash relative to the amount of Fe in the burnt fuel, $J_x$ is the fraction of Fe emitted for particle size $x$, $A_y$ is the fraction of a specific control device, and $R_{x,y}$ is the removal efficiency of control device $y$ for particle size $x$. Table 1-1 shows the emission strengths of iron aerosols, as estimated by the bottom-up method. For anthropogenic iron aerosols, the combustion of fossil fuel, particularly coal, provides the greatest contribution to emission. For example, *Wang et al.* (2015) estimated that ~80% of combustion iron emission (anthropogenic and biomass burning) in $PM_{10}$ arises from coal combustion, while *Ito et al.* (2018) estimated that 59% of anthropogenic iron aerosol emission is derived from energy generation. Iron aerosol emission from transportation (engine combustion and brake wearing) is negligibly low or not considered in bottom-up studies.

Using these emission strengths, the atmospheric abundance of iron aerosols and their deposition rates can be estimated. Although the emission strength and atmospheric burden of

**Table 1-1.** Global emission strength (Tg Fe/yr) of iron aerosols estimated by bottom-up methods.

| | Anthropogenic* | Biomass burning* | Mineral dust | Base year |
|---|---|---|---|---|
| *Ito et al.* 2013 | 0.51 | 1.15 | 74 | 2001 |
| *Luo et al.* 2008 | 0.66 | 1.07 | 55 | 1996 |
| *Wang et al.* 2015 | 0.87 | 0.48 | 41 | 2001 |
| *Ito et al.* 2018 | 1.91 | 0.79 | | Recent |

*For particles with an aerodynamic diameter less than 10 μm ($PM_{10}$)

anthropogenic iron aerosols are much lower than those of natural iron aerosols (Table 1), anthropogenic iron aerosols must be considered in ocean biogeochemistry because combustion iron aerosols have a higher solubility in seawater (high bioavailability) than mineral dust aerosols [*Chen et al*., 2012, *Myriokefalitakis et al*., 2015]. Two factors are considered to cause the high solubility of anthropogenic iron aerosols: the small particle size, because nano- to submicron-scale anthropogenic iron particles have a higher solubility than super-micron particles [*Cornell & Schwertmann*, 2004], and acid dissolution, because acids from anthropogenic gases (e.g., sulfate) condensing onto anthropogenic iron particle surfaces increase the solubility of iron [*Li et al.,* 2017].

In addition to iron deposition on the surface ocean, the light absorption of natural iron aerosols (mineral dust) has been evaluated from an emission inventory of mineral dust estimated by a bottom-up method [e.g., *Luo et al*., 2003]. *Bond et al.* (2013) calculated the global average absorption aerosol optical depth of mineral dust as 0.00094, which is approximately 40% of that of BC (0.00212). However, light absorption by anthropogenic iron oxide aerosols has not yet been studied. Although the atmospheric burden of anthropogenic iron oxide aerosols is much less than that of mineral dust (Table 1-1), magnetite, which is a primary chemical component of anthropogenic iron oxide, more strongly absorbs visible light than goethite and hematite, which are the primary chemical components of natural iron oxide. Thus, it is important to evaluate the radiative effect of anthropogenic iron oxide aerosols.

## 1.5 Purpose of this study

Iron aerosols play an important role in the Earth's climate on both short time scales as light-absorbers and long time scales as nutrient sources for the ocean ecosystem through the global carbon cycle. However, estimates of climate effects based on model simulations have large uncertainties due to a lack of quantitative observational data for iron aerosols, particularly anthropogenic aerosols. Although bottom-up methods enable researchers to evaluate the

relative contribution of individual emission sources and regions, it is not clear that the various emission sources of anthropogenic iron aerosols are considered. Moreover, no observational data have been provided in previous studies on emission strength. Thus, the emission strength must be estimated by a top-down method, where observational data are used as constraints, as is often performed for estimating the emission strength of greenhouse gases [*Hosely et al.,* 2018].

As mentioned in Section 1.3, iron measurements are based on filtration (off-line chemical speciation techniques); thus, it is difficult to obtain a statistical amount of quantitative observational data. Moreover, there have been few studies on the size distribution of iron aerosols in the atmosphere, although the size distribution of iron particles in combustion exhaust has been studied [*McElroy et al*., 1982, *Linak et al*., 2000]. To complement off-line filtration-based techniques, a rapid real-time method for measuring size-resolved concentrations with less detailed chemical information is desirable for determining the atmospheric abundance of (anthropogenic) iron aerosols over a wide spatial range for comparison with global models and top-down methods for estimating the emission strength.

In this study, I developed a laser-induced incandescence (LII) technique and established a novel method for measuring light-absorbing iron oxide aerosols (Chapter 2). This method can be applied to measure the concentration, size distribution, and mixing state of iron oxide aerosols with other aerosol compounds (e.g., sulfates and organics) on a short time scale (1–60 min). Using the developed LII technique, I observed iron oxide aerosols at Cape Hedo, located in the East Asia continental outflow, and demonstrated that most of the measured aerosols originate from anthropogenic sources (Chapter 3). I also found that the concentration of $FeO_x$ aerosols was strongly correlated with that of BC and CO. Based on the correlation slopes, I estimated the emission strength of anthropogenic iron aerosols using a top-down method, as an initial approach for estimating the emission strength of iron aerosols. In addition to the Hedo observation, I also obtained and analyzed iron oxide aerosols from the East Asian continental

outflow, an urban city, and an Arctic region to more fully evaluate the abundance and microphysical properties (size distribution and mixing state) of anthropogenic iron oxide aerosols in the northern hemisphere (Chapter 4). Finally, I worked with co-investigators to examine the abundance and climate impact of anthropogenic iron aerosols (Chapter 5). Based on the detailed analysis of $FeO_x$ aerosols in urban cities, we propose that vehicles are an important source of anthropogenic iron oxide aerosols (Section 5.1). In addition, a model simulation of anthropogenic iron aerosols based on the $FeO_x$ datasets measured by the developed LII method is presented (Section 5.2).

## References


Acosta-Martinez, V., Van Pelt, S., Moore-Kucera, J., Baddock, M. C., & Zobeck, T. M. (2015). Microbiology of wind-eroded sediments: Current knowledge and future research directions. *Aeolian Research*, *18*, 99-113.

Buonanno, G., Stabile, L., Avino, L., & Belluso, E. (2011). Chemical, dimensional and morphological ultrafine particle characterization from a waste-to-energy plant, *Waste Management*, *31*(11), 2253-2262, doi:10.1016/j.wasman.2011.06.017

Bond, T., Streets, D., Yarber, K., Nelson, S., Woo, J., & Klimont, Z. (2004), A technology-based global inventory of black and organic carbon emissions from combustion, *Journal of Geophysical Research: Atmospheres 1984 2012*, *109*(D14), doi:10.1029/2003jd003697.

Chen, H., Laskin, A., Baltrusaitis, J., Gorski, C. A., Scherer, M. M., & Grassian, V. H. (2012). Coal fly ash as a source of iron in atmospheric dust. *Environmental science & technology*, *46*(4), 2112-2120.

Cornell, R.M, & Schwertmann, U. (2004). *The Iron Oxides: Structure, Properties, Reactions, Occurrences and Uses, Second Edition*, Wiley, 703 pp. doi:10.1002/3527602097

Formenti, P., Caquineau, S., Chevaillier, S., Klaver, A., Desboeufs, K., Rajot, J. L., ... & Briois, V. (2014). Dominance of goethite over hematite in iron oxides of mineral dust from Western Africa: Quantitative partitioning by X-ray absorption spectroscopy. *Journal of Geophysical Research: Atmospheres*, *119*(22), 12-740.

Gillett, D., & Morales, C. (1979). Environmental factors affecting dust emission by wind erosion. *Saharan dust*, 71-94.

Guieu, C., Bonnet, S., Wagener, T., & Loÿe-Pilot, M. D. (2005). Biomass burning as a source of dissolved iron to the open ocean?. *Geophysical Research Letters*, *32*(19).

Guo, H., & Barnard, A. S. (2013). Naturally occurring iron oxide nanoparticles: morphology, surface chemistry and environmental stability. *Journal of Materials Chemistry A*, *1*(1), 27-42.

Hansen, J., & Nazarenko, L. (2004). Soot climate forcing via snow and ice albedos, *Proceedings of the National Academy of Sciences, 101*(2), 423-428, doi:10.1073/pnas.2237157100

Helble, J., Neville, M., & Sarofim, A. F. (1988). Aggregate formation from vaporized ash during pulverized coal combustion. In *Symposium (International) on Combustion* (Vol. 21, No. 1, pp. 411-417). Elsevier.

Hoesly, R. M., Smith, S. J., Feng, L., Klimont, Z., Janssens-Maenhout, G., Pitkanen, T., Seibert J. J., Vu, L., et al. (2018) Historical (1750–2014) anthropogenic emissions of reactive gases and aerosols from the Community Emissions Data System (CEDS), *Geoscientific Model Development, 11*(1), 369-408, doi:10.5194/gmd-11-369-2018.

Hsu, S. C., Wong, G. T., Gong, G. C., Shiah, F. K., Huang, Y. T., Kao, S. J., ... & Hung, C. C. (2010). Sources, solubility, and dry deposition of aerosol trace elements over the East China Sea. *Marine Chemistry*, *120*(1-4), 116-127.

Intergovernmental Panel on Climate Change (IPCC) (2013). Climate Change 2013: The Physical Science Basis. Contribution of Working Group I to the 5th Assessment Report of the IPCC. Cambridge University Press, Cambridge, UK.

Ito, A. (2013). Global modeling study of potentially bioavailable iron input from shipboard aerosol sources to the ocean, *Global Biogeochemical Cycles*,*27*(1), 1-10, doi:10.1029/2012GB004378

Ito, A., G. Lin, & J. Penner (2018), Radiative forcing by light-absorbing aerosols of pyrogenetic iron oxides, *Scientific Reports, 8*(1), 7347, doi:10.1038/s41598-018-25756-3.

Jickells, T., An, A. S., Anderson, K. K., Baker, A. R., Bergametti, G., Brooks, N., Cao, J. J., Boyd, P. W., et al. (2005). Global Iron Connections Between Desert Dust, Ocean Biogeochemistry, and Climate, *Science*, *308*(5718), 67-71, doi:10.1126/science.1105959

Journet, E., Balkanski, Y., & Harrison, S. P. (2014). A new data set of soil mineralogy for dust-

cycle modeling. *Atmospheric Chemistry and Physics*, *14*(8), 3801-3816.

Kukutschová, J., Moravec, P., Tomášek, V., Matějka, V., Smolík, J., Schwarz, J., Seidlerová, J., Šafářová, K., & Filip, P. (2011). On airborne nano/micro-sized wear particles released from low-metallic automotive brakes, *Environmental Pollution*, *159*(4), 998-1006, doi:10.1016/j.envpol.2010.11.036

Kutchko, B., & Kim, A. (2006). Fly ash characterization by SEM–EDS, *Fuel*, *85*(17-18), 2537-2544, doi:10.1016/j.fuel.2006.05.016

Lafon, S., Sokolik, I. N., Rajot, J. L., Caquineau, S., & Gaudichet, A. (2006). Characterization of iron oxides in mineral dust aerosols: Implications for light absorption. *Journal of Geophysical Research: Atmospheres*, *111*(D21).

Li, W., Xu, L., Liu, X., Zhang, J., Lin, Y., Yao, X., ... & Harrison, R. M. (2017). Air pollution–aerosol interactions produce more bioavailable iron for ocean ecosystems. *Science advances*, *3*(3), e1601749.

Liati, A., Pandurangi, S. S., Boulouchos, K., Schreiber, D., & Dasilva, Y. A. R. (2015). Metal nanoparticles in diesel exhaust derived by in-cylinder melting of detached engine fragments. *Atmospheric environment*, *101*, 34-40.

Linke, C., Möhler, O., Veres, A., Mohácsi, Á., Bozóki, Z., Szabó, G., and Schnaiter, M.: Optical properties and mineralogical composition of different Saharan mineral dust samples: a laboratory study (2006), *Atmospheric Chemistry and Physics*., *6*, 3315-3323, doi:10.5194/acp-6-3315-2006.

Linak, W. P., Miller, C. A., & Wendt, J. O. (2000). Comparison of particle size distributions and elemental partitioning from the combustion of pulverized coal and residual fuel oil. *Journal of the Air & Waste Management Association*, *50*(8), 1532-1544.

Liu, H., Yan, Y., Chang, H., Chen, H., Liang, L., Liu, X., ... & Sun, Y. (2019). Magnetic signatures of natural and anthropogenic sources of urban dust aerosol. *Atmospheric Chemistry and Physics*, *19*(2), 731-745.

Machemer, S. (2004). Characterization of Airborne and Bulk Particulate from Iron and Steel Manufacturing Facilities, *Environmental Science & Technology*, *38*(2), 381-389, doi:10.1021/es020897v

Magiera, T., Jabłońska, M., Strzyszcz, Z., & Rachwal, M. (2011). Morphological and mineralogical forms of technogenic magnetic particles in industrial dusts. *Atmospheric Environment*, *45*(25), 4281-4290.

Martin, J. H., & Fitzwater, S. E. (1988). Iron deficiency limits phytoplankton growth in the north-east Pacific subarctic. *Nature*, *331*(6154), 341.

Martin J. H., Gordon R. M., & Fitzwater, S. E. (1991). The case for iron. *Limnology and Oceanography*, *36*(8), 1793-1802. https://doi.org/10.4319/lo.1991.36.8.1793

McElroy, M. W., Carr, R. C., Ensor, D. S., & Markowski, G. R. (1982). Size distribution of fine particles from coal combustion. *Science*, *215*(4528), 13-19.

Menon, S., Hansen, J., Nazarenko, L., & Luo, Y. (2002). Climate effects of black carbon aerosols in China and India, *Science*, *297*(5590), 2250-2253, doi:10.1126/science.1075159

Ming, Y., Ramaswamy, V., & Persad, G. (2010). Two opposing effects of absorbing aerosols on global mean precipitation, *Geophysical Research Letter*, *37*(13), doi:10.1029/2010GL042895

Moosmüller, H., Chakrabarty, R. K., & Arnott, W. P. (2009). Aerosol light absorption and its measurement: A review, *Journal of Quantitative Spectroscopy and Radiative Transfer, 110*(11), 844–878, doi:10.1016/j.jqsrt.2009.02.035

Myriokefalitakis, S., Daskalakis, N., Mihalopoulos, N., Baker, A. R., Nenes, A., & Kanakidou, M. (2015). Changes in dissolved iron deposition to the oceans driven by human activity: a 3-D global modelling study. *Biogeosciences*, *12*(13), 3973-3992.

Luo, C., Mahowald, N. M., & Del Corral, J. (2003). Sensitivity study of meteorological parameters on mineral aerosol mobilization, transport, and distribution. *Journal of*

*Geophysical Research: Atmospheres*, *108*(D15).

Luo, C., Mahowald, N., Bond, T., Chuang, P., Artaxo, P., Siefert, R., Chen, Y., & Schauer, J. (2008). Combustion iron distribution and deposition, *Global Biogeochemical Cycles*, *22*(1), doi:10.1029/2007GB002964

McElroy, M. W., Carr, R. C., Ensor, D. S., & Markowski, G. R. (1982). Size distribution of fine particles from coal combustion. *Science*, *215*(4528), 13-19.

Myriokefalitakis, S., Daskalakis, N., Mihalopoulos, N., Baker, A. R., Nenes, A., & Kanakidou, M. (2015). Changes in dissolved iron deposition to the oceans driven by human activity: a 3-D global modelling study. *Biogeosciences*, *12*(13), 3973-3992.

Reddy, M. S., Basha, S., Joshi, H. V., & Jha, B. (2005). Evaluation of the emission characteristics of trace metals from coal and fuel oil fired power plants and their fate during combustion. *Journal of Hazardous Materials*, *123*(1-3), 242-249.

Sanderson, P., Su, S. S., Chang, I. T. H., Saborit, J. M., Kepaptsoglou, D. M., Weber, R. J. M., & Harrison, R. (2016). Characterisation of iron-rich atmospheric submicrometre particles in the roadside environment, *Atmospheric Environment, 140,* 167-175, doi:10.1016/j.atmosenv.2016.05.040

Tewalt, S. J., Belkin, H. E., SanFilipo, J. R., Merrill, M. D., Palmer, C. A., Warwick, P. D., Karlsen, A. W., Finkelman, R. B., and Park, A. J.: *Chemical analyses in the World coal quality inventory, version 1*: U. S. Geological Survey Open-File Report 20101196, available at: http://pubs.usgs.gov/of/2010/1196/ (last access: 10 March 2015), 2010.

Vassilev, S. V., Baxter, D., Andersen, L. K., & Vassileva, C. G. (2010). An overview of the chemical composition of biomass. *Fuel*, *89*(5), 913-933.

Wang, R., Balkanski, Y., Boucher, O., Bopp, L., Chappell, A., Ciais, P., ... & Tao, S. (2015). Sources, transport and deposition of iron in the global atmosphere. *Atmospheric Chemistry and Physics*, *15*(11), 6247-6270.

Xu, L., Chen, X., Chen, J., Zhang, F., He, C., Zhao, J., & Yin, L. (2012). Seasonal variations

and chemical compositions of PM2. 5 aerosol in the urban area of Fuzhou, China. *Atmospheric Research*, *104*, 264-272.

Zhang, X. L., Wu, G. J., Zhang, C. L., Xu, T. L., & Zhou, Q. Q. (2015). What is the real role of iron oxides in the optical properties of dust aerosols? *Atmospheric Chemistry and Physics*, *15*(21), 12159-12177.

# 2 Single-particle measurement of $FeO_x$ using a LII technique

## 2.1 Introduction

In this study, I used a single-particle soot photometer (SP2; Droplet Measurement Technologies, Boulder, CO, USA), a commercial instrument implementing laser-induced incandescence (LII) technique with an intracavity Nd:YAG laser ($\lambda$ = 1064 nm). The LII method measures incandescence light from strong light-absorbing and refractory particles passing through the laser beam, such as BC, silicon, nickel, and tungsten [*Stephens et al.,* 2003]. Among these incandescent particles, BC is assumed to be the only species that is abundant in the atmosphere. Thus, the SP2 has been used for the measurement of BC. Moreover, because the SP2 rapidly measures individual particles in real-time, it can be used for rapid real-time measurements of the BC mass and mixing state [*Moteki & Kondo* 2010, *Schwarz et al.,* 2015]. Using the SP2, traceable BC datasets acquired in various field campaigns [*Schwarz et al.,* 2010a] have been used to evaluate global models [*Wang et al.* 2014]. However, iron oxide is also refractory (boiling temperature ~3000 K), and some species, such as magnetite, are strong light-absorbers [*Zhang et al*., 2015]. Therefore, the LII technique is expected to measure iron oxide particles as well as BC.

In this study, I developed the LII technique to measure light-absorbing iron oxide particles. A detailed analysis of the light signals obtained by the LII shows that individual light-absorbing iron oxide particles can be identified and quantified. I also demonstrate that LII signals can be used to determine whether iron oxide particles arise from natural or anthropogenic sources. An evaluation of the mixing state of iron oxide particles is also presented in this section.

## 2.2 Instrument configurations

All of the SP2 configurations used in this study are identical to those described in *Moteki and Kondo* (2010) (Figure 2-1). Incandescence light is detected in the short-wavelength range (300–550 nm: blue band) by an H6779 photomultiplier tube (PMT, Hamamatsu Inc., Japan) without any optical filters and in the long-wavelength band (580–710 nm: red band) by an H6779–02 PMT (Hamamatsu Inc., Japan) equipped with a PB0640–140 bandpass optical filter (Asahi Spectra Inc., Japan). The power flux density at the center of the Gaussian intracavity laser beam was ~$1.5 \times 10^9$ $Wm^{-2}$, as estimated from the peak height of the scattering waveform of a polystyrene latex sphere with a known scattering cross section [*Schwarz et al.* 2010b].

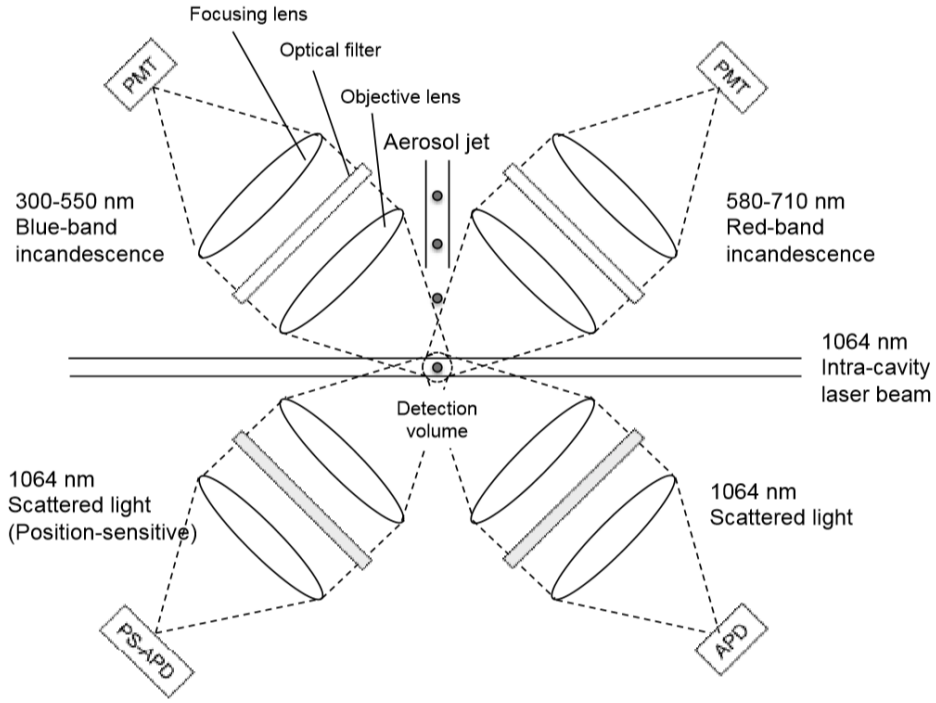


**Figure 2-1.** Schematic diagram of the SP2 optics **[***Moteki & Kondo* 2010**]**. Although the axis of the aerosol jet is perpendicular to the plane containing the optical detectors and the laser beam, it is drawn in parallel for simplicity. PMT, photomultiplier tube; PS-APD, position-sensitive APD.

## 2.3 Theoretical background

Figure 2-2 presents an example of incandescence and scattered light signals obtained by the SP2. The intensity of the scattering and incandescence signals, color ratio, incandescence onset position, and scattering cross section at the onset position in the laser beam are used to identify and quantify $FeO_x$ particles.

All particles passing through the laser beam elastically scatter the light. In addition to scattering, some particles are heated to several thousand Kelvin and then emit detectable black-body radiation in visible light, namely incandescence. The time-dependent intensity of the incandescence signal $S_i(t)$ is described as

$$S_i(t) = \int_{\Delta\Omega}\int_0^{\infty} C_{emit}(d, m, \lambda, shape, \Omega) P_e(T(t), \lambda)\, \eta(\lambda) d\lambda d\Omega, \tag{2.1}$$

where $\lambda$ is the wavelength, $\Omega$ is the direction of radiation propagation, $m$ is the complex refractive index, $d$ is the particle diameter, $T$ is the particle temperature, $C_{emit}$ is the emission cross section, $P_e$ is the Planck function, and $\eta$ indicates the transmissivity of the optical filter and the responsivity of the photodetector. Because $C_{emit}$ is equivalent to the absorption cross section $C_{abs}(-\Omega)$ based on Kirchhoff's law,

$$S_i(t) = \int_{\Delta\Omega}\int_0^{\infty} C_{abs}(d, m, \lambda, shape, -\Omega) P_e(T(t), \lambda)\, \eta(\lambda) d\lambda d\Omega. \tag{2.2}$$

$S_i(t)$ can also be expressed by the absorption efficiency $Q_{abs}$, which is the absorption cross section normalized by the geometrical cross section of the particle ($C_{abs} = \frac{\pi}{4} d^2 Q_{abs}$):

$$S_i(t) = \frac{\pi}{4} d^2 \int_{\Delta\Omega}\int_0^{\infty} Q_{abs}(d, m, \lambda, shape, -\Omega) P_e(T(t), \lambda)\, \eta(\lambda) d\lambda d\Omega. \tag{2.3}$$

It should be noted that $Q_{abs}$ is dependent on the particle size.

The time evolution of $S_i(t)$ is illustrated in Figure 2-2. The signal increases until the

particle temperature reaches the boiling point, $T_{boil}$. Once the particles begin vaporizing, $S_i(t)$ reaches a peak ($t = t_{peak}$) and then decreases monotonically due to vaporization. In this study, the peak incandescence intensity $S_i(t_{peak})$ is used to determine the size of an incandescent particle. Because $T(t_{peak})$ can be approximated as $T_{boil}$,

$$S_i(t_{peak}) = \frac{\pi}{4} d^2 \int_{\Delta\Omega} \int_0^{\infty} Q_{abs}(d, m, \lambda, shape, -\Omega) P_e(T_{boil}, \lambda)\, \eta(\lambda) d\lambda d\Omega. \tag{2.4}$$

Equation 2.4 shows that $S_i(t_{peak})$ is primarily affected by the particle size, refractive index, and boiling point. If the component of incandescent material is known, $S_{inc}(t_{peak})$ provides information on the incandescent particle volume.

The SP2 measures the incandescence intensity in two bands, i.e., in the blue band, $S_{i(b)}$, and the red band, $S_{i(r)}$. In this study, the ratio of these intensities is defined as the color ratio:

$$\begin{aligned} \text{Color ratio} &\equiv \frac{S_{i(b)}}{S_{i(r)}} \\ &= \frac{\int\int_{blue} Q_{abs}(m, \lambda, shape, -\Omega) P_e(T_{boil}, \lambda)\, \eta_{blue}(\lambda) d\lambda d\Omega}{\int\int_{red} Q_{abs}(m, \lambda, shape, -\Omega) P_e(T_{boil}, \lambda)\, \eta_{red}(\lambda) d\lambda d\Omega}. \end{aligned} \tag{2.5}$$

As a rough approximation, if $Q_{abs}$ and $\eta$ are considered to be constant within the considered wavelength range, we obtain

$$\text{Color ratio} \propto \frac{\int\int_{blue} P_e(T_{boil}, \lambda)\, d\lambda d\Omega}{\int\int_{red} P_e(T_{boil}, \lambda)\, d\lambda d\Omega}, \tag{2.6}$$

which indicates that the color ratio can be a proxy of the boiling point. Figure 2-3 shows the relationship between the color ratio and $T_{boil}$ based on Equation (2.6). The color ratio is a monotonically increasing function of $T_{boil}$ because the Planck function $P_e$ follows Wien's displacement law, where $P_e(\lambda)$ reaches its peak at shorter wavelengths for higher temperatures.

To obtain more information regarding the optical properties of the incandescent particle, the incandescence onset position ($t_{oi}$) is introduced in this study. The SP2 can monitor the particle position in the laser beam by measuring the scattering signal with positive-sensitive APD. $t_{oi}$ is defined as the onset timing when an incandescence signal is detected. Although this value is difficult to evaluate theoretically, it reflects the light absorption of the particle: a strongly absorbing particle should begin incandescing early, and vice versa.

In addition to incandescence, the SP2 measures scattered light ($S_s$ in Figure 2-2). $S_s$ is proportional to the scattering cross section of a particle integrated over the solid angle of light collection $C_s$:

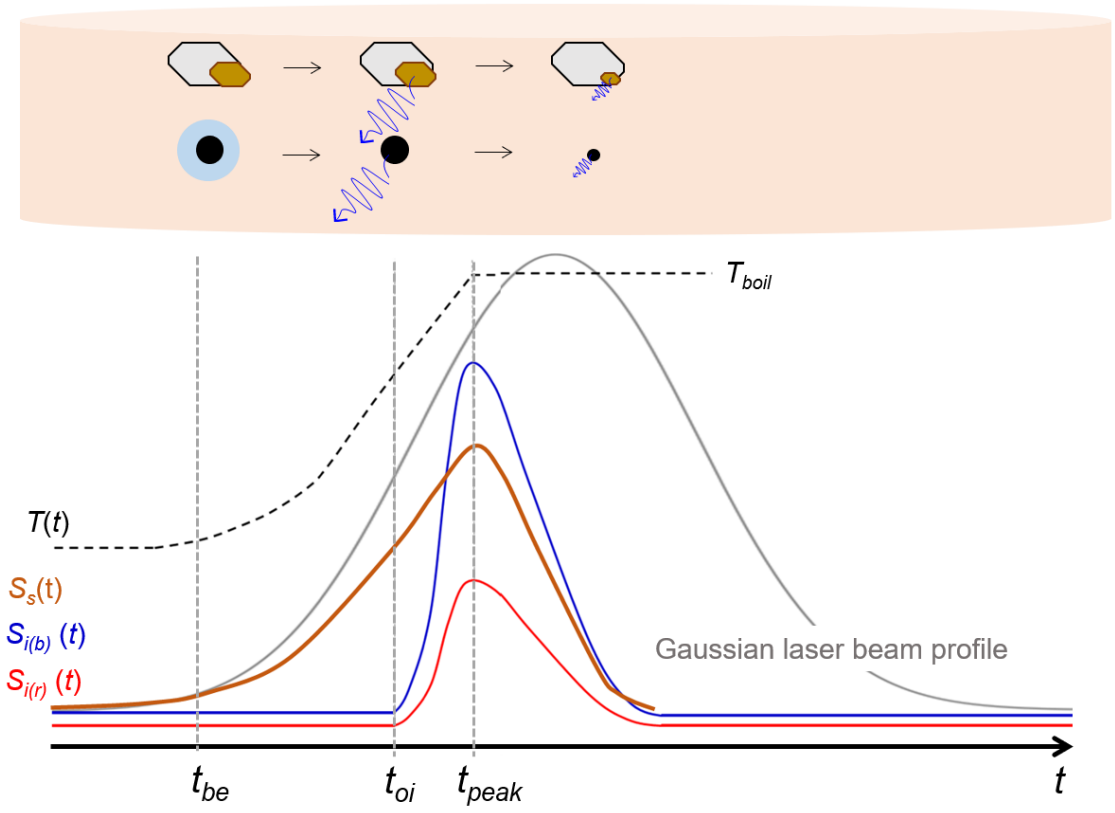


**Figure 2-2.** (Top) Schematic of a particle (natural iron oxide bound to aluminosilicate and anthropogenic iron oxide or BC coated by a volatile component) passing through a Gaussian laser beam. (Bottom) Schematic of incandescence and scattered light signals. $t$, time; $t_{be}$, time before evaporation; $t_{oi}$, time of incandescence onset; $T$(t), particle temperature; $T_{boil}$, boiling point; $S_s(t)$, scattering signal; $S_i(t)$, incandescence signal (blue and red bands).

$$S_s(t) = I(t)C_s(t), \tag{2.7}$$

where $I(t)$ is proportional to the laser power intensity at the particle position ($t$). By measuring $S_s(t)$ and monitoring the particle position in the laser beam, $C_s(t)$ can be estimated. $C_s$ is strongly dependent on the volume of a particle, including its incandescent and non-incandescent components. Here, I focus on the values of $C_s(t)$ at $t = t_{oi}$ and $t_{be}$, where $t_{be}$ is the time before the evaporation of nonrefractory materials such as sulfate and organics. $C_s(t_{oi})$ and $C_s(t_{be})$ reflect the volume of the particle that was affected and not affected by heating due to the laser beam, respectively.

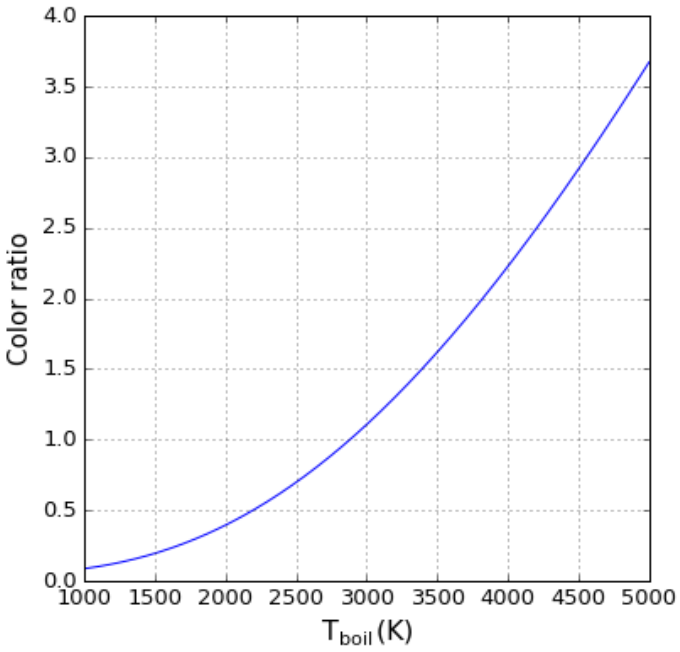


**Figure 2-3.** Color ratio calculated using Equation (2.6). A proportionality coefficient was determined to obtain consistency with the measured color ratio for fullerene soot ($T_{boil}$= 4230 K; *Moteki & Kondo*, 2010).

Iron oxides in mineral dust particles, which are often bound to refractory aluminosilicates, are expected to have large $C_s(t_{oi})$ values, even after heating. Here, I will demonstrate that a large $C_s(t_{oi})$ value is a characteristic feature of mineral dust particles.

I also use the value of $C_s$ to evaluate the mixing states of BC aerosols with other components (e.g. sulfate and organics). The coating material on BC particles evaporates due to the laser beam, reducing the value of $C_s$. Thus, the ratio of two scattering cross sections $C_s(t_{be})/C_s(t_{oi})$ can be used to estimate the thickness of coating materials on BC particles and the degree of atmospheric aging experienced by these particles [*Moteki et al.*, 2014]. Mixing state of $FeO_x$ is discussed in Appendix 2-2.

## 2.4 Laboratory experiment

This section presents experimental results obtained for iron oxide particles using the SP2 (LII). The measured quantities (peak incandescence signal, color ratio, incandescence onset timing, and scattering cross section) are investigated to establish the measurement of iron oxide aerosols using the SP2. The samples used in the laboratory experiment are described in Table 2. Fullerene soot was applied for BC [*Moteki & Kondo,* 2010], and commercially available finely powdered metals and minerals were used for the samples. For mineral dust particles (natural iron oxide), dust from the Taklamakan desert, which is one of the primary mineral dust sources in North China, was used [*Uno et al*., 2009].

All powder samples were aerosolized from a tube-assembled glass flask in an ultrasonic bath, in which the glass was vibrated, thus causing the powder to swirling. Then, aerosolized samples were introduced to the SP2 at particle-free airflow of 1 L $min^{-1}$. In some experiments, the laboratory samples were sorted by mass using an aerosol particle mass analyzer (APM model 3601, Kanomax, Japan; *Tajima et al*., 2011) before being introduced to the SP2 in order to determine the size-resolved probability of incandescence and to derive a relationship between the particle mass and peak incandescence signal intensity. The sorting range of the

APM analyzer was 10–1000 fg.

## 2.5 Results and discussion

### 2.5.1 Incandescent particles

The samples that incandesced in the SP2 in this experiment are listed in Table 2-1. Fullerene soot, a reference material for BC [*Moteki and Kondo*, 2010], incandesces in the SP2 because BC is a strong absorber and has a high boiling point (~4230 K). Magnetite and hematite also incandesce in the SP2, but goethite does not. Goethite is a weakly absorbing material, as reflected by the small imaginary part of its refractive index (Figure 2-4), resulting in a lack of incandescence. In addition, ferrihydrite does not incandesce. Although the refractive index of ferrihydrite has not been studied, the sample used in this study was synthesized as nanosized particles. Thus, the absorption cross section of a particle, whose diameter is much smaller than the laser wavelength ($\lambda$ = 1064 nm), may be too small for the particle to heat and incandesce. Quartz is one of the primary components of mineral dust and does not incandesce, which is consistent with the transparency of aluminosilicate in visible light [*Zhang et al.,* 2015]. In contrast, Taklamakan desert dust particles incandesce in the SP2 because the iron oxides, such

**Table 2-1. List of samples used in the laboratory experiment.**

| Sample name | Information | Incandescence |
|---|---|---|
| Fullerene soot | Alfa Aesar Inc., Stock#40971, Lot#FS12S011 | Yes |
| Magnetite ($Fe_3O_4$) | Kojundo Chemical Laboratory Co., Ltd., Japan | Yes |
| Hematite ($Fe_2O_3$) | Kojundo Chemical Laboratory Co., Ltd., Japan | Yes |
| Goethite (FeOOH) | Kojundo Chemical Laboratory Co., Ltd., Japan | No |
| Quartz ($SiO_2$) | Kojundo Chemical Laboratory Co., Ltd., Japan | No |
| Ferrihydrite ($Fe_5HO_8 \cdot 4H_2O$) | Synthesized | No |
| Taklamakan desert dust | Sampled at 36°25'N, 81°58'E, 2656 m ASL | Yes |

as hematite and magnetite, are bound to aluminosilicate. The ability of the SP2 to detect incandescence signals emitted from some metals, including tungsten, nickel, and aluminum, has been previously reported [*Stephens et al.,* 2003]. However, this study is the first work to demonstrate that the SP2 can detect incandescent light from hematite and magnetite particles. Hereafter, light-absorbing iron oxide particles (magnetite and hematite) that can be detected by the SP2 are defined as $FeO_x$.

Despite their incandescence ability, not all magnetite and hematite particles incandescence because the light absorptivity $Q_{abs}$ strongly depends on the particle size (Figure 2-5 shows an example for a spherical particle). Figure 2-6 shows the probability of incandescence for fullerene soot, magnetite, and hematite. The probability of incandescent is defined as the fraction of incandescent particles among all particles detected by the scattering signal. Almost all fullerene soot particles with a size of 25–300 fg incandesce in the SP2. In contrast, the probabilities of incandescence for magnetite and hematite decrease with decreasing mass, most likely due to the low laser absorption efficiency of the smaller particles (Figure 2-5).

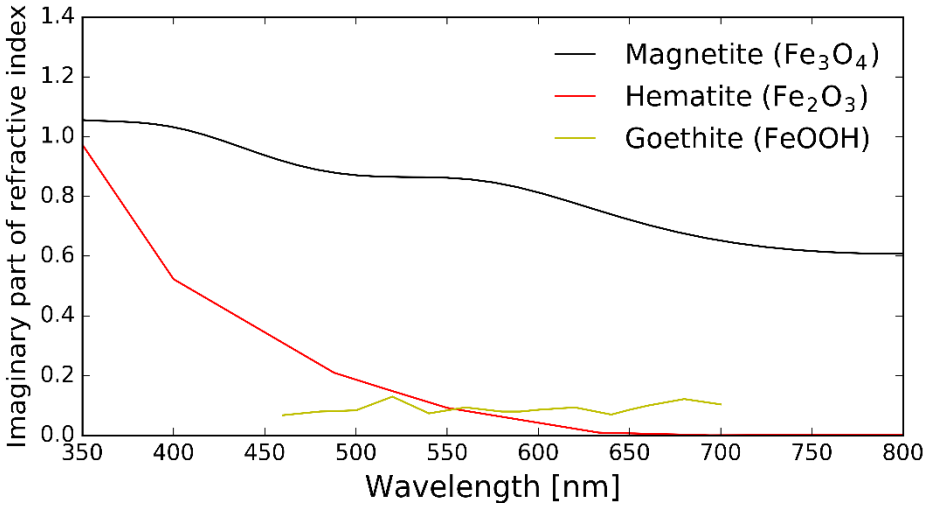


**Figure 2-4.** Imaginary part of the refractive index of magnetite [*Huffman and Stapp*, 1973], hematite [*Shettle and Fenn*, 1979], and goethite [*Bedidi and Cervelle*, 1993].

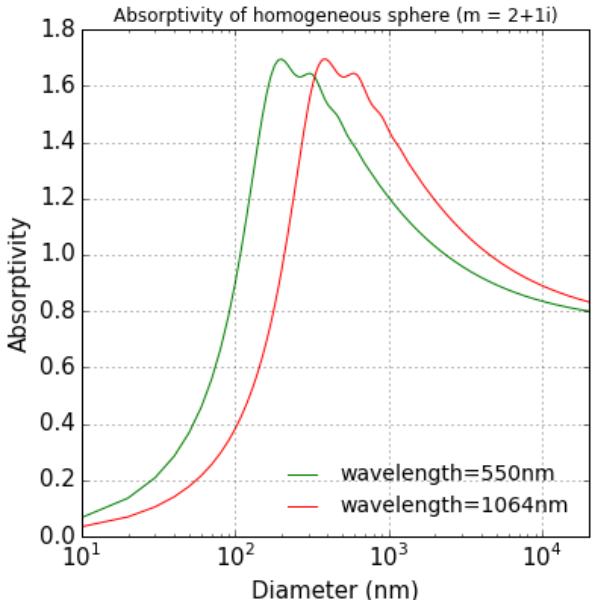


**Figure 2-5.** Calculated absorptivity of a homogeneous sphere with complex refractive index of 2 + 1i using Mie theory (*Bohren & Huffman,* 1983).

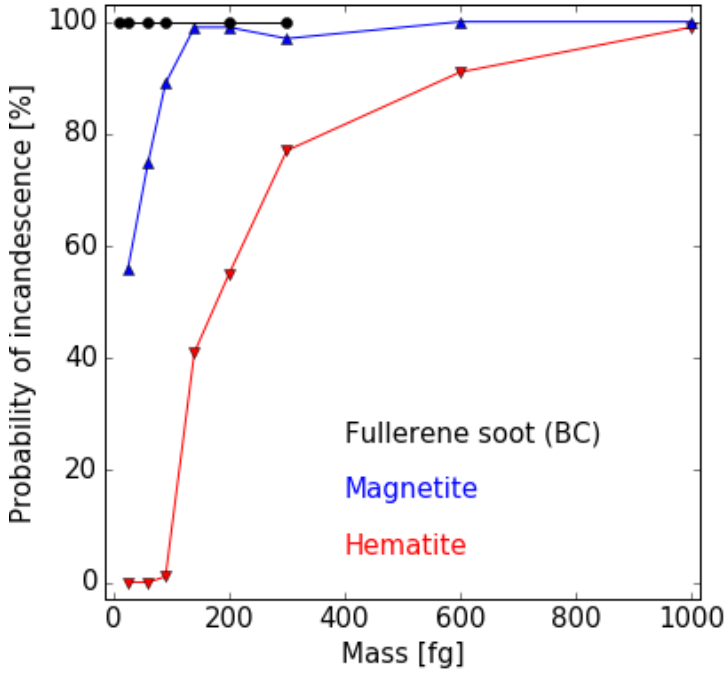


**Figure 2-6.** Incandescence probabilities of BC and $FeO_x$ particles.

### 2.5.2 Color ratio

The measured color ratios of individual laboratory magnetite and fullerene soot particles are shown in Figure 2-7. For the laboratory magnetite particles, the color ratios were measured at ~1.6, corresponding to $T_{boil}$ ~3300 K (Figure 2-3), which is close to the boiling point of iron (3134 K, *Lide*, 2000). The hematite data exhibit a distribution similar to that of magnetite. Thus, $FeO_x$ can be discriminated from BC (color ratio ~2.5), but hematite and magnetite are indistinguishable.

A theoretical curve for a spherical iron and magnetite particle at $T = 3300$ K is also shown in Figure 2-7, where the $S_i$ and color ratio values were computed using Equation (2.5). The absorption efficiency $Q_{abs}$ was calculated from the Mie theory using the wavelength-resolved refractive index of bulk iron and magnetite (*Johnson & Christy*, 1974). The theoretical relationship between the peak incandescence signal and the color ratio for spherical particles

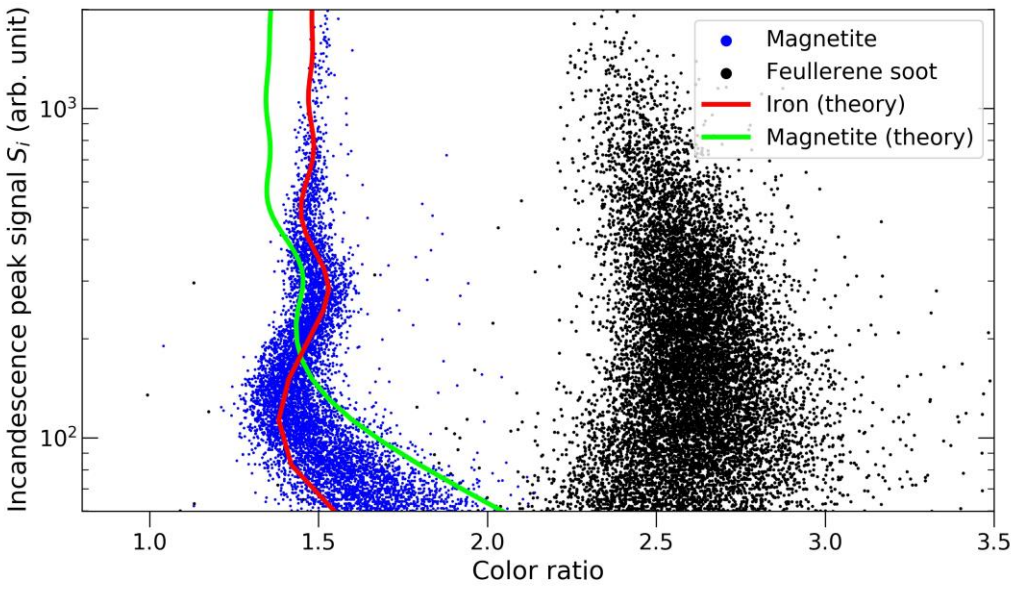


**Figure 2-7.** Scatter plot of the peak incandescence signal in the blue band and the color ratio of magnetite (blue) and fullerene soot particles (black). The colored curve shows computational results for iron and magnetite spherical particles with a boiling temperature of 3300 K.

shows a unique ripple structure that is highly similar to the experimental results for magnetite. This structure is highlighted in the range of $S_i$ = ~200–1000, corresponding to a particle size range of 50–500 nm, comparable to the incandescence wavelength. Within this size range for a spherical particle, the absorption efficiency is strongly dependent on the particle size and wavelength (Figure 2-5), resulting in the ripple structure shown in Figure 2-7. This result indicates that $FeO_x$ particles transform to spherical iron particles due to melting associated with thermal decomposition [*Qu et al.*, 2014] in the laser beam.

### 2.5.3 Incandescence onset position

The measured incandescence onset position $t_{oi}$ for $FeO_x$ particles and Taklamakan desert dust is shown in Figure 2-8, where $t_{oi}$ is expressed as the distance of a particle from the center axis of the laser beam, scaled by the standard deviation of the power profile of the Gaussian laser beam. A negative (positive) $t_{oi}$ value indicates that the particle begins to incandesce before

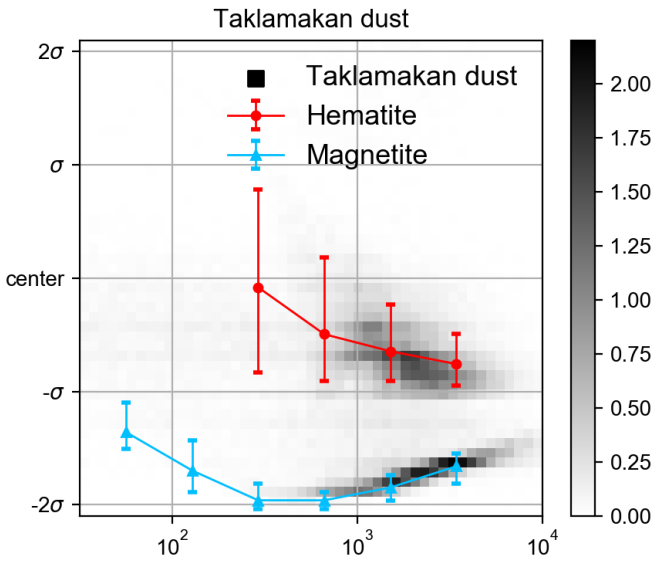


**Figure 2-8.** Incandescence onset position of iron oxide particles. The colored markers represent the median values for laboratory-based magnetite (blue) and hematite (red) particles. The error bars denote the 10$^{th}$ to 90$^{th}$ percentiles, and the gray shading represents the number fraction for the Taklamakan desert dust sample.

(after) reaching the center axis. The laboratory magnetite sample incandesced earlier than the hematite for all size domains detectable by the SP2, reflecting its larger imaginary part of the refractive index compared to hematite (Figure 2-4). For Taklamakan desert dust, both magnetite and hematite modes were observed. Because these two modes are separated, pure magnetite and hematite particles can be distinguished based on $t_{oi}$.

### 2.5.4 Quantification of $FeO_x$ and BC particles

The relationship between the peak height of the blue-band incandescence signal $S_{i(b)}(t_{peak})$ and the particle mass classified by the APM is shown in Figure 2-9. The intensity for fullerene soot is proportional to the particle mass $x$ in the small-mass domain of $x < 25$ fg. This result was theoretically expected because the particle is comparable to or smaller than the wavelength of incandescent light. The absorption efficiency of a particle of this size can be approximated by the Rayleigh–Gans approximation:

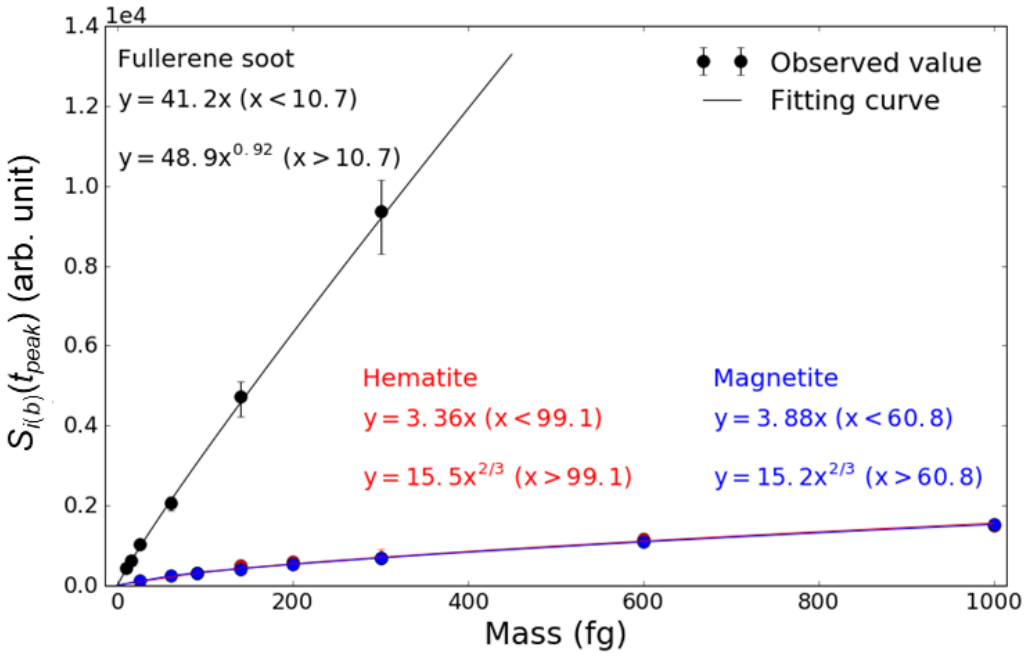


**Figure 2-9.** Relationship between the incandescence peak signal in the blue band and the mass of BC and $FeO_x$ particles. The markers represent median values, and the error bars show $10^{th}$–$90^{th}$ percentile values, which are overlapped by the markers for some data points.

$$Q_{abs} = \frac{4\pi d}{\lambda} \mathrm{Im}\left(\frac{m^2 - 1}{m^2 + 1}\right), \tag{2.8}$$

and from Equation (2.2),

$$S_i(t_{peak}) \propto d^3, \tag{2.9}$$

indicating that $S_{\mathrm{i(b)}}(t_{peak})$ is proportional to the particle mass.

The experimental data are fitted by functions (Figure 2-9) to estimate the ambient aerosol mass from the measured value of $S_{i(b)}(t_{peak})$. For the small-mass domain ($x$ < 25 fg for fullerene soot and $x$ < 100 fg for hematite and magnetite), linear functions were used for fitting (Equation 2.7), consistent with the Rayleigh–Gans theory. For the large-mass domain, power functions were used. The $FeO_x$ data were successfully fitted using power functions proportional to the particle mass with an exponent of 2/3. For $FeO_x$ mass > 1000 fg, which is beyond the upper limit of the APM sorting, these power function dependences were extrapolated as follows. First, it is theoretically predicted that the emission cross section ($C_{\mathrm{emit}}$) of a particle is proportional to the surface area when the particle size is much larger than the wavelength (i.e., geometric optical limit). Second, it is expected that iron oxides will melt and transform into spherical droplets (surface area $\propto$ $x^{2/3}$) prior to the onset of incandescence in the laser beam (Section 2.5.2). However, for large BC particles, a power function of $x^{0.92}$ was applied for fitting because BC sublimates in the laser beam and remains in an aggregate form. Because the volume-to-surface ratio for incandescing BC particles is larger than that for $FeO_x$, the exponent of $x$ is larger than 2/3 (= 0.67).

Based on the fitting functions, the mass-equivalent diameters ($D_{\mathrm{m}}$) of $FeO_x$ and BC can be estimated from the measured $S_{i\,(\mathrm{b})}(t_{\mathrm{peak}})$ values. The fitting curves for magnetite and hematite are close, indicating that the uncertainty in quantifying the $D_{\mathrm{m}}$ value of $FeO_x$ particles due to the difference in the oxidation state is negligible.

### 2.5.5 Scattering cross section

Figure 2-10 shows the relationship between the scattering cross section at the onset timing of incandescence, denoted by $C_s(t_{oi})$, and mass equivalent diameter ($D_m$) estimated from $S_{i(b)}(t_{peak})$ value. The $C_s(t_{oi})$ values above $\sim 1.4 \times 10^{-14} m^2$ are saturated because of the detection limit of the scattering signal. In the small-size domain ($D_m$ < 270 nm), the $C_s(t_{oi})$ values differ greatly between the laboratory and Taklamakan desert dust samples. For laboratory magnetite, $\log(C_s(t_{oi}))$ is proportional to $D_m$; however, for the Taklamakan desert sample, the $C_s(t_{oi})$ values for more than 90% of the particles are saturated. This result suggests that the majority of Taklamakan desert particles incandescing in the SP2 are $FeO_x$ particles internally mixed with non-absorbing and refractory mineral compounds such as aluminosilicate and quartz [melting point ~1900 K (*Deer et al.*, 1992)]. Therefore, the saturation of $C_s(t_{oi})$ indicates the presence of dust-like $FeO_x$ particles.

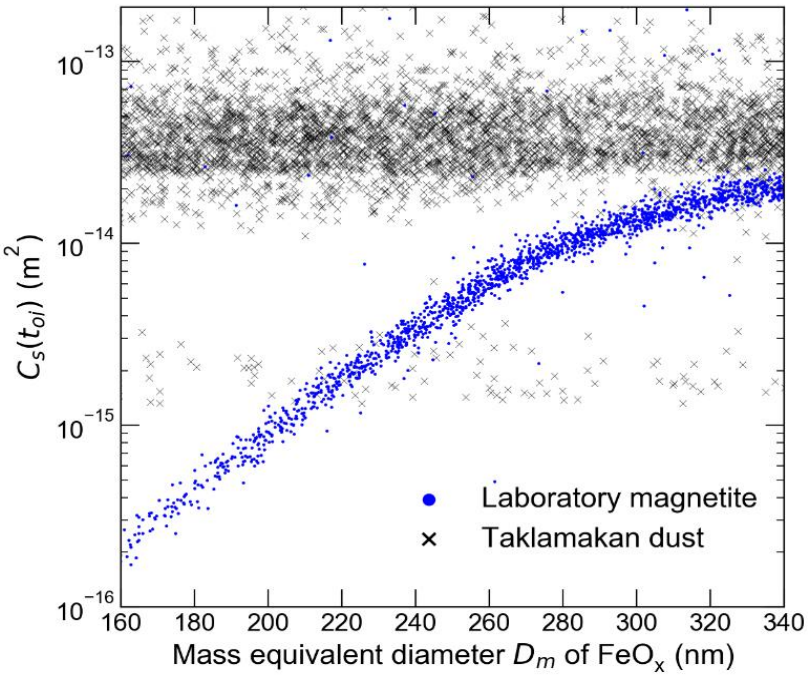


**Figure 2-10.** Scatter plots of the scattering cross section at the onset of incandescence $C_s(t_{oi})$ and the mass-equivalent diameter $D_m$ for magnetite and Taklamakan desert dust particles.

## 2.6 Summary

I have applied the SP2 (LII technique) to demonstrate that $FeO_x$ particles incandesce under laser exposure. Based on the obtained experimental results, I have established a method for measuring $FeO_x$ aerosols using the LII technique (Figure 2-11). Focusing on the difference in boiling point, $FeO_x$ can be discriminated from BC. The $D_m$ values of $FeO_x$ and BC particles can be estimated from the $S_{i(b)}(t_{peak})$ value, and $t_{oi}$ is a good proxy for capturing the difference in light absorption between hematite and magnetite. For small $FeO_x$ particles ($D_m$ < 270 nm), $C_s(t_{oi})$ can be used to determine whether a particle corresponds to dust-like $FeO_x$.

With LII, single-particle measurements of $FeO_x$ can be rapidly performed. Thus, single-particle data can be integrated with the concentration and size distribution of ambient $FeO_x$ aerosols. In the following chapter, I will demonstrate that observational $FeO_x$ aerosol data with a high time resolution (1–60 minutes) can be obtained using the established method.

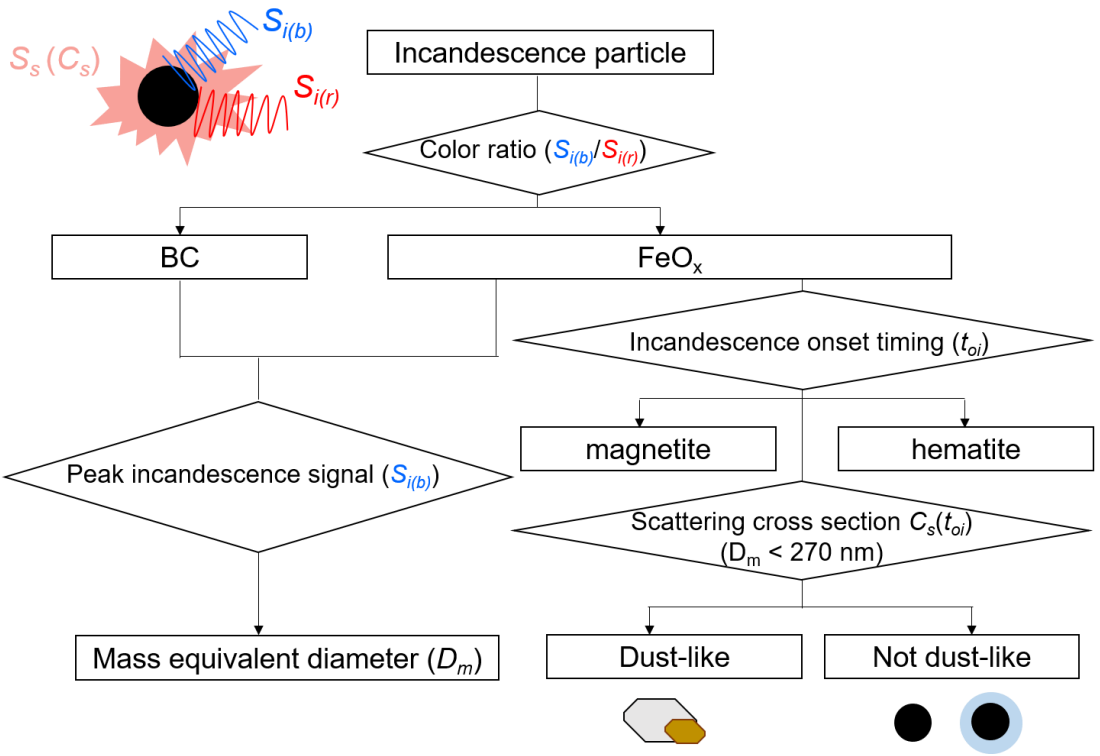


**Figure 2-11.** Flow chart of $FeO_x$ and BC measurements based on the developed LII technique.

## Appendix 2-1: Transmission efficiency of $FeO_x$ aerosols

This section evaluates $FeO_x$ particle loss caused by particle settling on the wall of the sampling tube. Although this loss is not generally considered in BC measurements, it may be crucial for $FeO_x$ measurements because of the high density of BC (~1.8 g/cm$^3$) and FeOx (~5 g/cm$^3$). The primary mechanisms governing particle loss include gravitational settling, diffusion, and inertial deposition in flow constrictions.

Particles settle due to gravitational forces and deposit on the wall in a sampling system, such as a transporting tube. The transport efficiency for gravitational settling in laminar airflow (corresponding to the inlet system airflow used in this study) in a circular horizontal tube was theoretically established by *Fuchs* (1964) and *Thomas* (1958) as

$$\eta_{\text{grav}} = 1 - \frac{2}{\pi}\left[2\varepsilon\sqrt{1-\varepsilon^{2/3}} - \varepsilon^{1/3}\sqrt{1-\varepsilon^{2/3}} + \arcsin\left(\varepsilon^{1/3}\right)\right] \quad \text{(2-1A)}$$

$$\varepsilon = \frac{3}{4}Z = \frac{3}{4}\frac{L}{d}\frac{V_{ts}}{U} \quad \text{(2-2A)}$$

where $Z$ is the gravitational deposition parameter, $L$ is the tube length, $d$ is the inner tube diameter, $V_{ts}$ is the terminal particle settling velocity, and $U$ is the gas velocity.

Due to Brownian motion, the particles will diffuse toward and deposit on the tube wall. For a laminar flow, *Holman* (1972) derived the transport efficiency due to diffusion in the tube as

$$\eta_{\text{diffuse}} = \exp[-\xi Sh], \quad \text{(2-3A)}$$

$$Sh = 3.66 + \frac{0.2672}{\xi + 0.10079\xi^{1/3}}, \quad \text{(2-4A)}$$

$$\xi = \frac{\pi DL}{Q}, \quad \text{(2-5A)}$$

where $D$ is the particle diffusion coefficient and $Q$ is the volumetric flow rate through the

tube.

Inertial deposition under flow constrictions in a sampling line must be considered to evaluate particle loss because the sampling system of the SP2 has an abrupt constriction, where the inner tube diameter changes from 2.0 to 0.5 mm. *Muyshondt et al*. (1996) gave the transport efficiency for this case as

$$\eta_{\text{const,inertial}} = 1 - \frac{1}{1 + \left\{ \frac{2\,Stk\left[1 - \left(\frac{d_o}{d_i}\right)^2\right]}{3.14\exp(-0.0185\theta)} \right\}^{-1.24}}, \tag{2-6A}$$

where $S_{tk}$ is the Stokes number, $d_i$ and $d_o$ are the inner and outer tube diameters, respectively, and $\theta$ is the contraction angle (90°).

In summary, the transport efficiency for $FeO_x$ measurement can be calculated as

$$\eta_{\text{calculated}} = \eta_{\text{grav}}\eta_{\text{diffuse}}\eta_{\text{const,inertial}}. \tag{2-7A}$$

I measured the transport efficiency of pure magnetite particles transported through a 1/4" tube with a length of $L = 3.13$ m, $\eta_{\text{experiment}}(\text{L} = 3.13\text{ m})$ for comparison with $\eta_{\text{calculated}}(\text{L} = 3.13\text{m})$. In the experiment, the normalized size distributions of magnetite particles passing through 1/4" tubes of different lengths ($L$ and $L + 3.31$ m) were measured, with $\eta_{\text{experiment}}$ indirectly defined as the ratio of size distributions:

$$\eta_{\text{experiment}}(L = 3.13\text{m}) = \frac{\text{d}N(L)/\text{dlog}D_m}{\text{d}N(L + 3.13\text{m})/\text{dlog}D_m}. \tag{2-8A}$$

Ideally, d*N*/dlogD in Equation 2-8A should be measured for a single particle group, but such experimental conditions are difficult to achieve. In this work, normalized d*N*/dlogD values were used for comparison, resulting in an overestimated $\eta_{\text{experiment}}$ value. Figure 2A-1 compares the experimental and calculated transport efficiencies. The reduction of $\eta$ in the large-size domain is consistent with both the experimental and calculated results. A gap in the small-size domain, particularly at $D_{\text{m}}{\sim}200$ nm, may be due to the overestimation of the

normalized $\mathrm{d}N(L)/\mathrm{dlog}D_m$ value in Equation (2-8A).

Figure 2A-1 shows that a substantial fraction of large $FeO_x$ particles is lost before being introduced to the SP2, leading to an underestimate of the $FeO_x$ concentration. Thus, I modified the mass concentration of observed $FeO_x$ aerosols using Equation 2-7A in data analyses in the following chapters (Chapter 3–5).

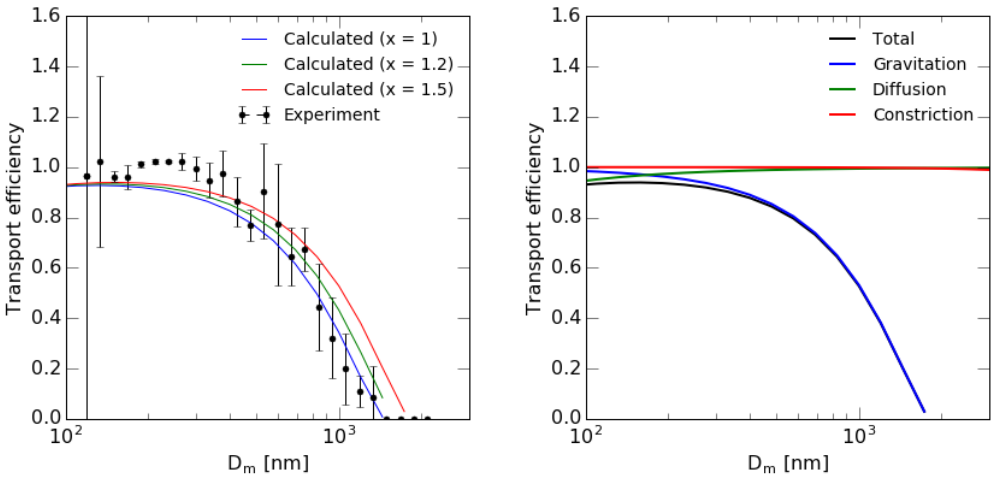


**Figure 2A-1.** (Left) Size-resolved transport efficiency of magnetite particles passing through a 1/4" tube with L = 3.13 m. The lines present theoretical values calculated for particles with various values for the dynamic shape factor x (x = 1 corresponds to a sphere). The markers with vertical bars indicate the mean value ± standard deviation for four experiments. (Right) Calculated transport efficiency of each loss mechanism for magnetite particles with x = 1.5.

## Appendix 2-2: Mixing state of $FeO_x$ aerosols

I evaluated the relationship between the shell-to-core ratio and $C_s(t_{be})/C_s(t_{oi})$ of aggregated $FeO_x$ aerosols. As discussed above, $FeO_x$ particles transform into a spherical morphology during their passage through the laser beam (Figure 2A-2a). Figure 2A-2b shows the computed relationship between the mass-equivalent shell-to-core ratio of an $FeO_x$ particle and the scattering cross section ratio, $\log(C_s(t_{be})/C_s(t_{oi}))$. $C_s(t_{be})$ is computed using the block-DDA method described in *Moteki et al*. (2017), assuming a monomer diameter of 34 nm and a fractal dimension of 2.8, and $C_s(t_{oi})$ was computed using the Mie theory. Different values of the refractive index $m$ were used for $FeO_x$ at $t_{be}$ and $t_{oi}$ because $FeO_x$ can transform from $FeO_x$ to iron in the laser beam. The refractive indices of magnetite (2.27 + 0.54i: *Huffman & Stapp*, 1973) and iron (2.95 + 4.00i: *Johnson & Christy*, 1974) were used for $m(t_{be})$ and $m(t_{oi})$, respectively, and the refractive index of the coating material was assumed to be 1.50 + 0.00i. The calculation results show that $C_s(t_{be})/C_s(t_{oi})$ can be used to estimate the thickness of the coating material on an aggregated $FeO_x$ particle, despite the difference in morphology at $t = t_{be}$ and $t_{oi}$.

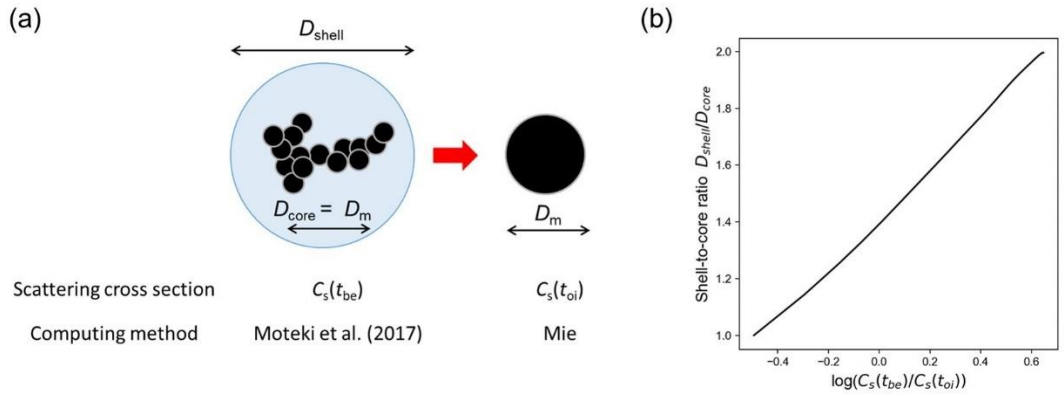


**Figure 2A-2.** (a) Schematic image of coated $FeO_x$ particles at $t_{be}$ and a melted (spherical) $FeO_x$ particle at $t_{oi}$. (b) Computed relationship between the mass-equivalent shell-to-core ratio of an $FeO_x$ particle and the scattering cross section ratio, $\log(C_s(t_{be})/C_s(t_{oi}))$.

## References


Bedidi, A., & Cervelle, B. (1993). Light scattering by spherical particles with hematite and goethite like optical properties: effect of water impregnation. *Journal of Geophysical Research: Solid Earth*, *98*(B7), 11941-11952.

Deer, W. A., Howie, R. A., & Zussman, J. (1992). *An introduction to the rock-forming minerals* (Vol. 696). London: Longman.

Fuchs, N. A. (1964). The Mechanics of Aerosols. *Oxford: Pergamon*

Holman, J. P. (1972). *Heat Transfer*. New York: McGrawHill

Huffman, D. R., & Stapp, J. L. (1973). Optical measurements on solids of possible interstellar importance. In *Interstellar dust and related topics* (pp. 297-301). Springer, Dordrecht.

Johnson, P.B., Christy, R.W.: *Phys. Rev*. B9 (1974) 5056

Liati, A., Pandurangi, S., Boulouchos, K., Schreiber, D., & Dasilva, Y. (2015). Metal nanoparticles in diesel exhaust derived by in-cylinder melting of detached engine fragments, *Atmospheric Environment*, *101*, 34-40, doi:10.1016/j.atmosenv.2014.11.014

Lide, D. R. (2000). *CRC Handbook of Chemistry and Physics*, 81st ed., CRC Press, Boca Raton, FL, doi:10.1021/ja0048230

Moteki, N., & Kondo, Y. (2010). Dependence of laser-induced incandescence on physical properties of black carbon aerosols: Measurements and theoretical interpretation. *Aerosol Science and Technology*, *44*(8), 663-675.

Moteki, N., Kondo, Y., & Adachi, K. (2014). Identification by single-particle soot photometer of black carbon particles attached to other particles: Laboratory experiments and ground observations in Tokyo, *Journal of Geophysical Research: Atmospheres*, *119*(2), 1031-1043, doi:10.1002/2013JD020655

Moteki, N., Adachi, K., Ohata, S., Yoshida, A., Harigaya, T., Koike, M., & Kondo, Y. (2017). Anthropogenic iron oxide aerosols enhance atmospheric heating., *Nature*

*Communications, 8,* 15329, doi:10.1038/ncomms15329

Muyshondt, A., A. R. McFarland, and N. K. Anand (1996). Deposition of aerosols particles in contraction fittings. *Aerosol Sci. Technol*. 24:205-216.

Qu, Y., Yang, Y., Zou, Z., Zeilstra, C., Meijer, K., & Boom, R. (2014). Thermal decomposition behavior of fine iron ore particles. *ISIJ International*, *54*(10), 2196-2205.

Schwarz, J. P., Spackman, J. R., Gao, R. S., Watts, L. A., Stier, P., Schulz, M., ... & Fahey, D. W. (2010a). Global-scale black carbon profiles observed in the remote atmosphere and compared to models. *Geophysical Research Letters*, *37*(18).

Schwarz, J. P., Spackman, J. R., Gao, R. S., Perring, A. E., Cross, E., Onasch, T. B., ... & Dubey, M. K. (2010b). The detection efficiency of the single particle soot photometer. *Aerosol science and technology*, *44*(8), 612-628.

Schwarz, J. P., Perring, A. E., Markovic, M. Z., Gao, R. S., Ohata, S., Langridge, J., ... & Fahey, D. W. (2015). Technique and theoretical approach for quantifying the hygroscopicity of black-carbon-containing aerosol using a single particle soot photometer. *Journal of Aerosol Science*, *81*, 110-126.

Shettle, E. P., & Fenn, R. W. (1979). *Models for the aerosols of the lower atmosphere and the effects of humidity variations on their optical properties* (No. AFGL-TR-79-0214). Air Force Geophysics Lab Hanscom Afb Ma.

Stephens, M., Turner, N., & Sandberg, J. (2003). Particle identification by laser-induced incandescence in a solid-state laser cavity. *Applied optics*, *42*(19), 3726-3736.

Tajima, N. et al. (2011). Mass range and optimized operation of the aerosol particle mass analyzer. *Aerosol Science and Technology*, *45*(2), 196-214.

Thomas, J. W. 1958. *J. Air Pollut. Control Assoc*. 8:32.

Uno, I., Eguchi, K., Yumimoto, K., Takemura, T., Shimizu, A., Uematsu, M., ... & Sugimoto, N. (2009). Asian dust transported one full circuit around the globe. *Nature Geoscience*, *2*(8), 557.

Wang, Q., Jacob, D. J., Spackman, J. R., Perring, A. E., Schwarz, J. P., Moteki, N., ... & Barrett, S. R. (2014). Global budget and radiative forcing of black carbon aerosol: Constraints from pole-to-pole (HIPPO) observations across the Pacific. *Journal of Geophysical Research: Atmospheres*, *119*(1), 195-206.

Zhang, X. L., Wu, G. J., Zhang, C. L., Xu, T. L., & Zhou, Q. Q. (2015). What's the real role of iron-oxides in the optical properties of dust aerosols? *Atmospheric Chemistry and Physics Discussion*, *15*(4), 5619-5662, doi:10.5194/acpd-15-5619-2015.

# 3 Abundance and emission strength of iron oxide aerosols in the East Asian continental outflow

## 3.1 Introduction

East Asia, particularly China, has numerous pollutant emission sources and has thus drawn much attention in climate and epidemiology studies [*Chan & Yao*, 2008]. These emission sources are driven by variable mechanisms, including fuel combustion, waste combustion, vehicle activity, and residential activity [*Bond et al.*, 2013, *Hoesly et al*., 2018]. These sources also emit anthropogenic iron aerosols [*Liati et al*., 2015, *Luo et al*., 2008, *Wang et al.*, 2015]. Thus, East Asia is an important emission region to consider in studying the effect of anthropogenic iron aerosols on the climate.

To date, various field measurements of anthropogenic iron aerosols have been conducted in East Asia and in the East Asian continental outflow via aerosol filtration. These studies have found anthropogenic iron aerosols through techniques such as electron microscopy [*Liu et al,*. 2017] and X-ray absorption fine structure spectroscopy (STXM/NEXAFS) [*Moffet et al.*, 2012] and have revealed the detailed morphology and elemental composition of anthropogenic iron aerosols. However, these studies are based on filtration, as described in Section 1.3; therefore, there is no statistical data on the atmospheric abundance (concentration and size distribution) of anthropogenic iron aerosols.

In this chapter, I demonstrate that the developed LII method can be applied to successfully observe anthropogenic $FeO_x$ aerosols emitted from East Asia, including China. Approximately 170 data points of 1-h mass, number concentrations, and size distributions of anthropogenic $FeO_x$ aerosols were obtained. Based on this large amount of data, I reveal that

anthropogenic $FeO_x$ aerosols are correlated with BC and CO. Based on the mass ratio of $FeO_x$ to BC and CO, the emission strengths of anthropogenic $FeO_x$ were also estimated.

## 3.2 Observation site

Continuous ground-based observations were performed at the Cape Hedo Atmosphere and Aerosol Monitoring Station (CHAAMS), Okinawa Island, Japan (26.87°N, 128.25°E; 60 m above sea level) from 8 to 25 March 2016. Okinawa Island is surrounded by the East China Sea and the Pacific Ocean, and CHAAMS is located at the northern edge of the island. CHAAMS is located approximately 100 km from the nearest densely populated region, with no substantial local emission. Thus, representative polluted air from East Asia can be observed at CHAAMS. Local meteorological data (temperature, humidity, precipitation, and wind speed) were continuously monitored at CHAAMS (http://www.nies.go.jp/asia/hedomisaki/home-e.html), and vertical profiles of mineral dust, spherical aerosols, and cloud droplets were continuously measured by polarization lidar [*Shimizu et al*., 2004]. The instruments used in this observation were installed in a room at CHAAMS as follows. The sampling inlet was set on a wall approximately 3 m above the ground, and particles were passed from the sampling inlet to the instruments through transport tubes with no impactor. The tube configurations utilized for sampling $FeO_x$ and BC aerosols are presented in Table 4A-2; these configurations are also referenced in the estimation of particle loss during transmission.

## 3.3 Instruments

BC and $FeO_x$ aerosols were measured using the SP2 with the developed LII technique (Chapter 2). CO was measured using a Picarro G2401 $CO/CH_4/CO_2/H_2O$ analyzer (Picarro Inc., USA) based on the cavity ring-down spectrum technique [*Crosson*, 2008; *Zellweger et al.*, 2012]. The accuracy of the CO concentration measurement is 0.1 ppbv.

During the observation, aerosols were also collected for electron microscopy conducted by Dr. Adachi (Meteorological Research Institute). Aerosol samples were collected on Cu grids with a formvar substrate over 5-min periods at intervals of 1–4 h during the observation period, with a total of 226 samples collected using two-stage impactor samplers (AS-24W, Arios Inc., Tokyo, Japan). The samplers have lower and upper 50% cutoff aerodynamic diameters of approximately 100 and 700 nm, respectively. Samples collected on the fine stages were used for TEM analyses. TEM images were obtained using a 120-kV TEM (JEM-1400, JEOL), and the particle compositions were measured by EDS (Oxford Instruments) in the scanning TEM mode (STEM-EDS) [*Adachi et al*., 2016, 2018].

## 3.4 Particle loss in the sampling system

Gravitational deposition, diffusion, and inertial deposition in flow constrictions caused non-negligible $FeO_x$ particle loss during the transmission of air from the sampling inlet to the laser beam in the SP2, as discussed in Appendix 2-1. I calculated the transmission efficiency, defined as the fraction of particles transported to the laser beam from the sampling inlet, using Equation (2-7A). The geometry and flow rate of the sampling system are specified in Table 4A-2. I also experimentally assessed the transmission efficiency using a portable optical particle sizer (OPS, Model 3330, TSI Inc.). Two categories of size-resolved number concentrations of ambient aerosols were measured using the OPS: 1) concentration measured outside the room without any transport tubes and 2) concentration with the transport tubes in the same setup used for the SP2 measurement (Figure 3-1). The ratio of these concentrations can be interpreted as the transmission efficiency. Figure 3-1 shows the measured and calculated transmission efficiencies. The measured results agree with the calculated results, obtained by assuming a particle density of approximately 2 $g/cm^3$, which is a typical value for ambient aerosols. This agreement supports our application of Equation (2-7A) to calculate the loss of $FeO_x$ and BC aerosols during transmission. In the calculation, I used the bulk densities of $FeO_x$

(magnetite, 5.17 g/cm$^3$) and BC (1.8 g/cm$^3$) to estimate the transmission efficiency (Figure 3-1b). Figure 3-1c shows the particle loss of magnetite due to three individual mechanisms. Gravitational deposition considerably decreases the transmission efficiency, especially for large particles ($D_m$ > 1 μm). I will use the transmission efficiency to correct the mass concentration of the $FeO_x$ aerosols in Section 3.6.

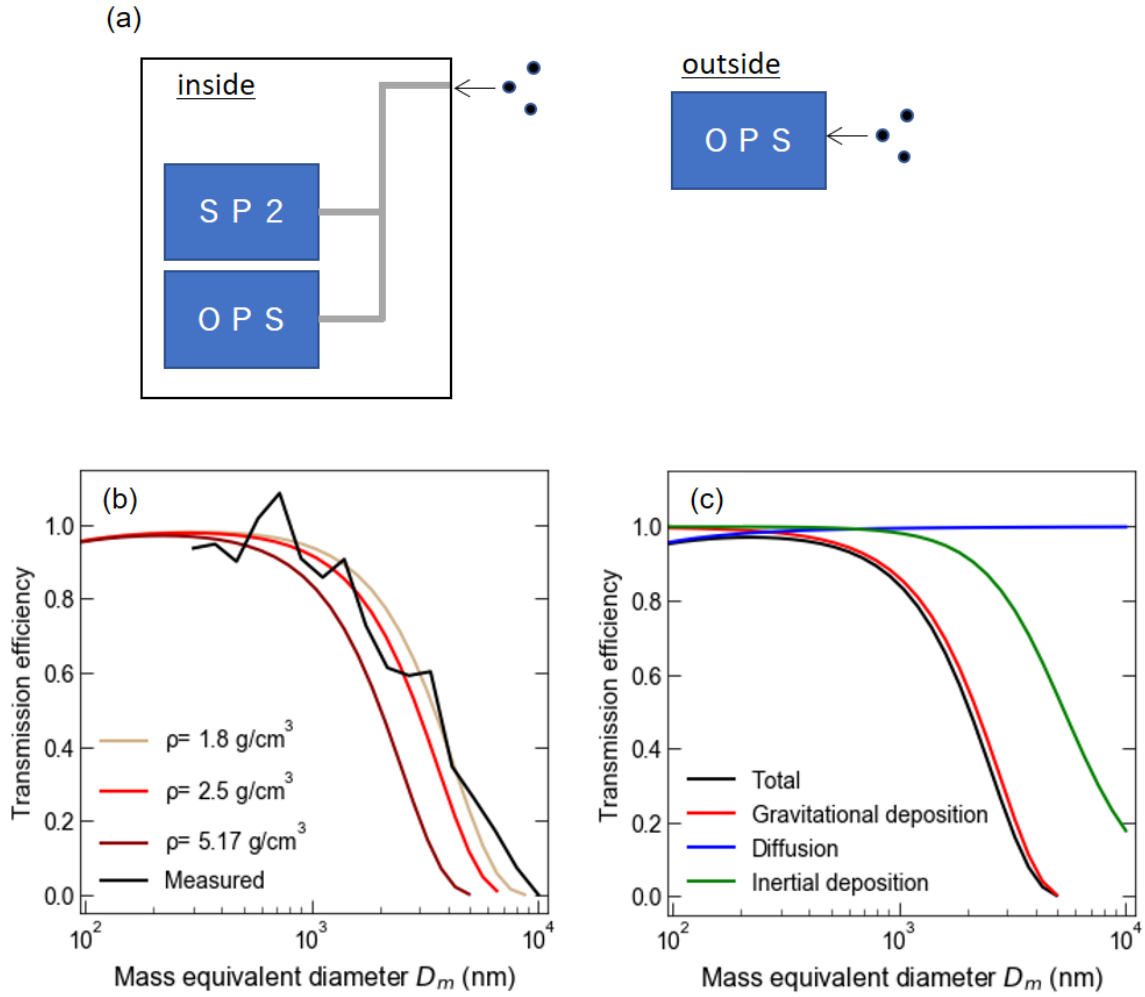


**Figure 3-1.** (a) Schematic image of the experiment for evaluating the transmission efficiency. (b) Transmission efficiency determined experimentally (black line) and theoretically (colored lines). The experimental data represent the average from two measurements. The theoretical values were calculated using three different particle densities, assuming a shape factor of 1.5. (c) Theoretical transmission efficiencies for individual loss mechanisms of particles with a density of 5.17 g/cm$^3$ and a shape factor of 1.5.

## 3.5 Single-particle quantities

### 3.5.1 Color ratio

I first classified incandescent particles as $FeO_x$ or BC using the color ratio, which is a proxy for the boiling point (Figure 3-2). The incandescent aerosols measured at CHAAMS have color ratios that are distinctively distributed over the laboratory $FeO_x$ (color ratio ~1.5) and BC (color ratio ~2.5) regions. I classified $FeO_x$ and BC particles using the threshold represented as a solid line in Figure 3-2. Some $FeO_x$ particles are distributed in the small-size domain ($S_i$ < ~400), where laboratory hematite particles do not incandesce (Chapter 2), implying that the observed $FeO_x$ particles, or at least those in these small-size domains,

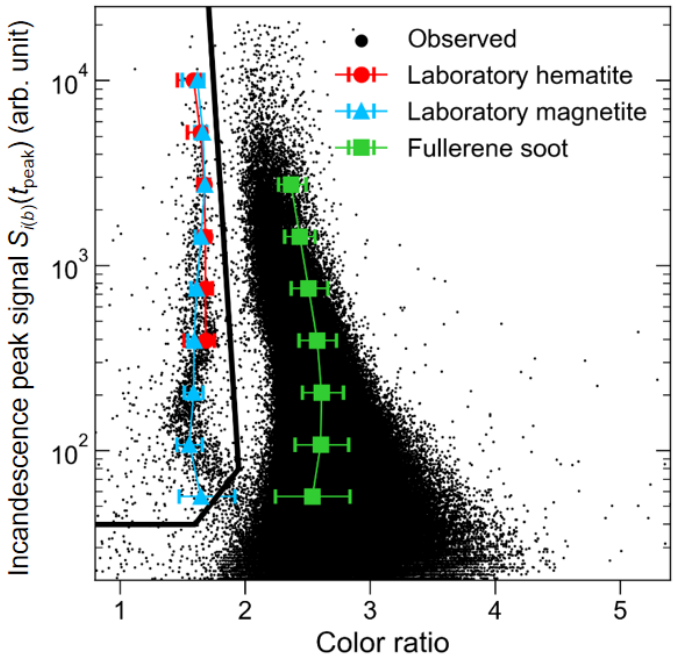


**Figure 3-2.** Scatter plots of the peak incandescence signal in the blue band and the color ratio of aerosols observed on 10 March (black points). The data distributions observed during the other periods are similar to that of 10 March. The colored markers represent the median values for laboratory magnetite (blue), hematite (red), and fullerene soot (green) samples (measured in laboratory experiments). The error bars denote the $10^{th}$–$90^{th}$ percentiles. The solid black line represents the threshold used in this study to discriminate $FeO_x$ from BC.

have different optical properties compared to pure hematite. Moreover, the distribution for the $FeO_x$ aerosols in Figure 3-2 shows a ripple structure appeared for laboratory measurements and theoretical curve in Figure 2-7. This result indicates that ambient $FeO_x$ aerosols melted into spherical particles in the laser beam, supporting the use of an extrapolated fitting curve for determining the $D_m$ values for large particles with mass > 1000 fg (Section 2.5.4).

I further examined the observed $FeO_x$ particles by focusing on the incandescence onset position in the laser beam ($t_{oi}$), as the proxy for light absorption. Figure 3-3 shows results for the $FeO_x$ particles measured throughout the entire observation period, where $t_{oi}$ is expressed as the distance of a particle from the center axis of the laser beam, scaled by the standard deviation of the power profile of a Gaussian laser beam. A negative (positive) $t_{oi}$ value indicates that a particle begins to incandesce before (after) reaching the center axis. Some $FeO_x$ aerosols are distributed in the laboratory-determined magnetite region; however, there are also unknown particles distributed outside the classified regions, particularly small $FeO_x$ particles (low $S_{i(b)}(t_{peak})$). These particles have different optical properties compared to pure hematite and magnetite. Maghemite ($\gamma$-$Fe_2O_3$) aerosols, whose incandescence probability and $t_{oi}$ are unknown, are emitted by steel manufacturing [*Machemer, 2004*] and coal burning [*Linak et al., 2007*]. Moreover, an inhomogeneous distribution of Fe oxidation states within individual anthropogenic Fe-containing aerosols due to atmospheric aging was reported by *Takahama et al.* (2008). Therefore, an internal mixture of magnetite and hematite with various relative fractions may be partially responsible for the broadly distributed $t_{oi}$ values, ranging between those of magnetite and hematite (Figure 3-3). However, this hypothesis cannot yet be verified nor can an internal mixture be used for calibration due to difficulties in preparing laboratory $FeO_x$ samples of an internal magnetite–hematite mixture with a controlled mass fraction. In this study, I used only pure magnetite particles for SP2 calibration of the iron oxide mass measurement. The choice of pure magnetite for the calibration should not significantly affect

the results because the signal-to-$FeO_x$ mass relationships (calibration curves) were almost identical between magnetite and hematite particles (Figure 2-9), which have similar bulk densities (5.17 and 5.25 g/cm$^3$, respectively) [*Lide*, 2000].

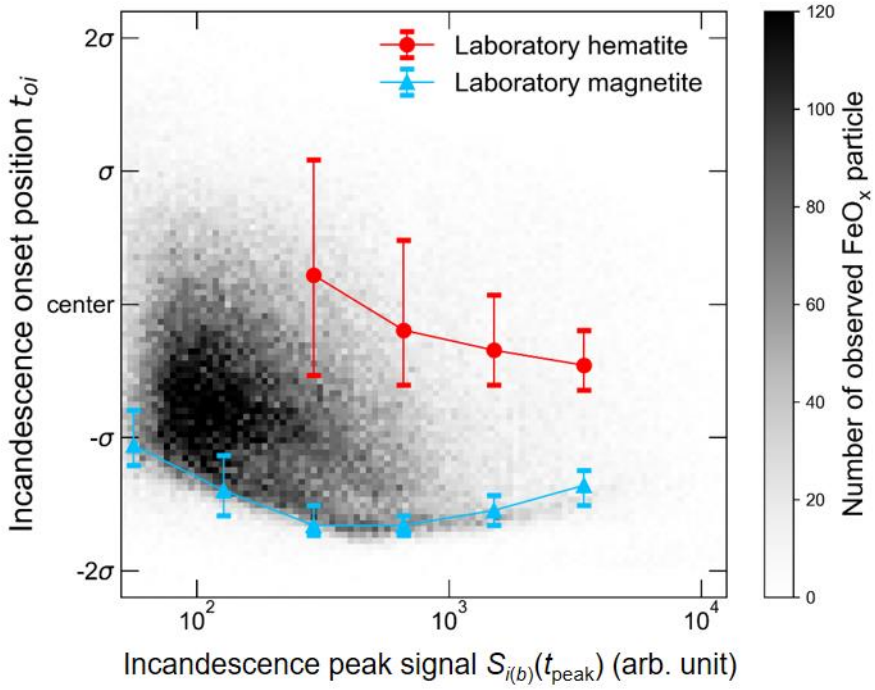


**Figure 3-3.** Scatter plots of the incandescence onset position $t_{oi}$ and the peak incandescence signal in the blue band, $S_i$, for $FeO_x$ particles measured throughout the entire observation period (grayscale). The colored markers represent median values for laboratory-based magnetite (blue) and hematite (red) particles, and the error bars denote the 10$^{th}$–90$^{th}$ percentiles.

Finally, I examined the scattering cross section at the onset timing of incandescence $C_s(t_{oi})$, which is a useful parameter for identifying mineral dust or anthropogenic $FeO_x$. Figure 3-4 shows a scatter plot of $C_s(t_{oi})$ for the observed $FeO_x$ aerosols and experimental results for laboratory magnetite and Taklamakan desert mineral dust particles. Results are shown only for small $FeO_x$ particles ($D_m$ < 340 nm); for larger particles, the measured $C_s(t_{oi})$ value of pure magnetite is saturated (> ~2 × $10^{-14}$ $m^2$) because the data acquisition system of the scattering channels was saturated. A saturated $C_s(t_{oi})$ is found for mineral dust particles, even for small $FeO_x$ particles ($D_m$ < 340 nm). As mentioned in Section 2.5.5, this result can be attributed to internal mixing between aluminosilicate particles and $FeO_x$. However, more than 90% of the

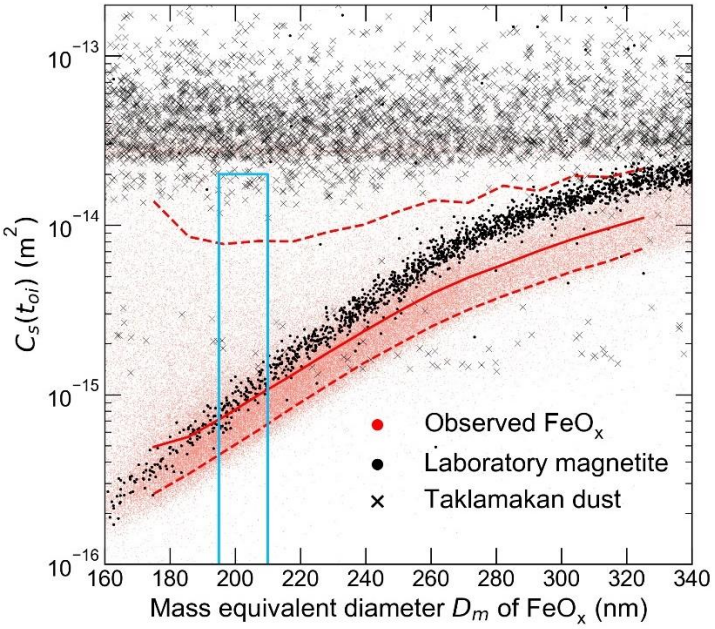


**Figure 3-4.** Scatter plots of the scattering cross section at the onset of incandescence $C_s(t_{oi})$ and mass-equivalent diameter $D_m$ for ambient $FeO_x$ aerosols measured throughout the entire period of observation, as well as results for laboratory magnetite particles and Taklamakan desert dust particles. The median value for the observed $FeO_x$ particles is represented by a solid red line between two dashed red lines, which represent the $10^{th}$ and $90^{th}$ percentile values Blue lines represent the criteria for evaluating the mixing state of observed $FeO_x$ particles, as discussed in Section 4.7.

observed $FeO_x$ particles with $D_m < 340$ nm have unsaturated $C_s(t_{oi})$ values, indicating that most of the particles are not mineral dust.

The distributions obtained by the SP2 measurement (Figures 3-2, 3-3, and 3-4) were relatively constant throughout the entire observation period. Air masses arriving at CHARMS during our observations can be characterized based on their source (Section 3.6), and although these air masses have different abundances of $FeO_x$ aerosols (Section 3.6), their optical properties are statistically similar.

### 3.5.2 Comparison with TEM analysis

The $FeO_x$ measurements were compared with TEM measurements, based on approximately 1900 particles from four samples and Fe-containing aerosols. Nanosized Fe particles were found to be mixed, either internally or externally, with organics and sulfate (Figure 3-5). Based on their morphology and elemental distribution, the Fe-containing particles were classified as $FeO_x$ aggregated particles or Si-rich fly ash particles; no natural $FeO_x$ particles (mineral dust) were found in the analyzed samples. The numbers of aggregated $FeO_x$ and Fe-containing fly ash particles counted using TEM are summarized in Table 3-1, where the number of $FeO_x$ particles detected by the SP2 is also shown. The number of $FeO_x$ particles measured by the SP2 exhibits a positive correlation with that of aggregated $FeO_x$ particles measured by TEM rather than that of Fe-containing fly ash particles.

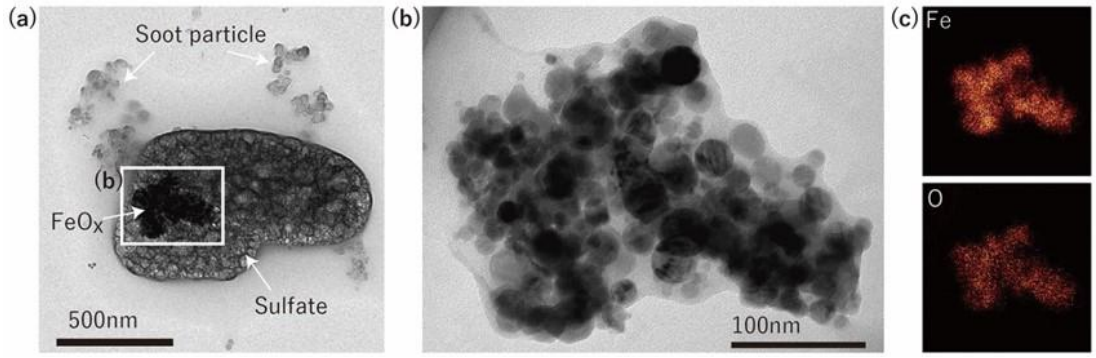


**Figure 3-5.** (a) TEM image of $FeO_x$ aggregate particles internally mixed with sulfate, sampled from 20:00 to 20:05 on 20 March 2016 (local time). Soot particles around the particle are also shown. (b) Enlarged image of the rectangular area outlined in image (a). Sulfate was decomposed by an electron beam. (c) Distributions of Fe and O within image (b), indicating that the aggregated particle is iron oxide.

**Table 3-1.** Number of Fe-containing particles in the TEM grid sample and $FeO_x$ particles detected by the SP2.

| | | TEM | | | SP2 |
|---|---|---|---|---|---|
| Sample number | Sampling time[a] | All measured particles | Aggregated $FeO_x$ | Fe-containing fly ash | $FeO_x$ |
| 1 | 10 Mar. 08:00–08:05 | 344 | 1 | 1 | 14 |
| 2 | 14 Mar. 16:00–16:05 | 550 | 6 | 1 | 59 |
| 3 | 20 Mar. 20:00–20:05 | 488 | 8 | 9 | 191 |
| 4 | 21 Mar. 08:00–08:05 | 510 | 3 | 1 | 116 |
| Total | | 1892 | 18 | 12 | 380 |

[a]Local time (JST).

### 3.5.3 Characterization of $FeO_x$ aerosols measured by the SP2

Based on the statistical distribution of the single-particle quantities measured by the SP2 (color ratio, $t_{oi}$, and $C_s(t_{oi})$) and the relative abundance of each type of Fe-bearing particle estimated by TEM analysis, I conclude that most $FeO_x$ aerosols detected by the SP2 at CHAAMS were aggregates of anthropogenic iron oxide. To support the minor contribution of mineral dust observed in our $FeO_x$ measurement data, I evaluated the correlation between the number concentration ratio of $FeO_x$ to BC measured by the SP2 and the ratio of large aerosols

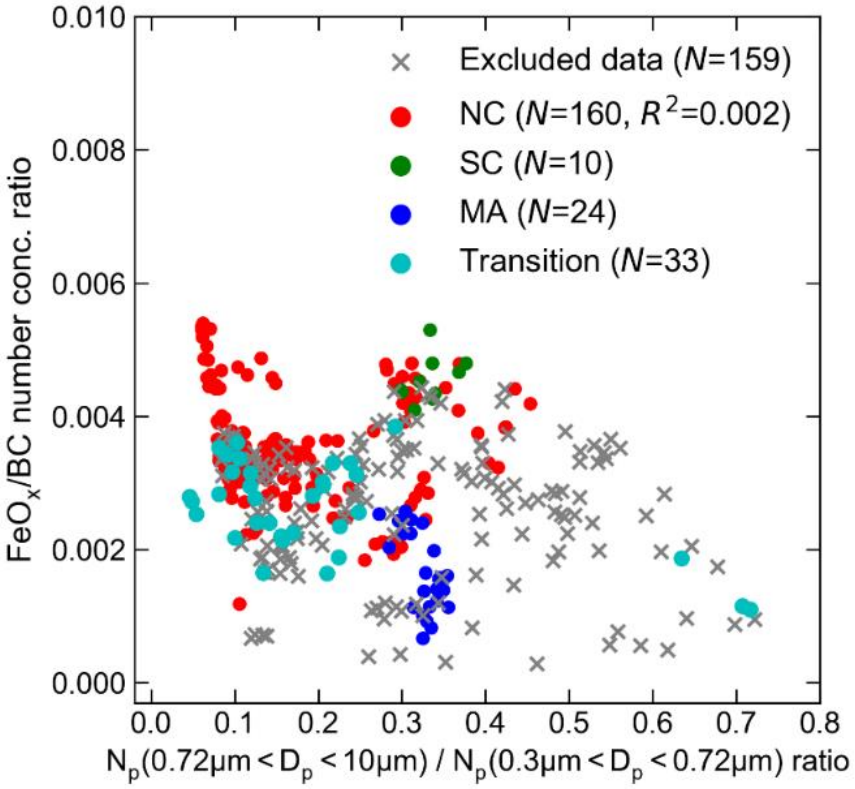


**Figure 3-6.** Scatter plot of the number concentration ratio of $FeO_x$ to BC aerosols measured by the SP2 and the ratio of small aerosols (0.3 μm < $D_p$ < 0.72 μm) to large aerosols (0.72 μm < $D_p$ < 10 μm) measured by the OPS, where $D_p$ denotes the light-scattering-equivalent diameter. The different colors represent the air mass type, according to the classification given in Section 3.6.

(> 0.72 μm) to small aerosols (< 0.72 μm) measured by the OPS (Figure 3-6). No correlation was found ($R^2 \approx 0$), implying that super-micron-sized mineral dust particles contribute very little to the abundance of $FeO_x$ aerosols measured by the SP2.

*Moffet et al*. (2012) performed chemical analyses of Fe-containing particles sampled at CHAAMS in the spring. By applying STXM-NEXAFS to screen the elemental distribution of individual Fe-containing particles, the *Moffet et al*. (2012) observed a minor contribution from mineral dust. This result is consistent with the conclusion that the observed $FeO_x$ particles in this study originated from anthropogenic sources.

## 3.6 Abundance and microphysical properties of anthropogenic iron oxide aerosols

### 3.6.1 Air mass characterization

Figure 3-7 shows a time series plot of the mass concentration of $FeO_x$ and BC aerosols observed at CHAAMS. The temporal variations of these two aerosol species were similar. Both

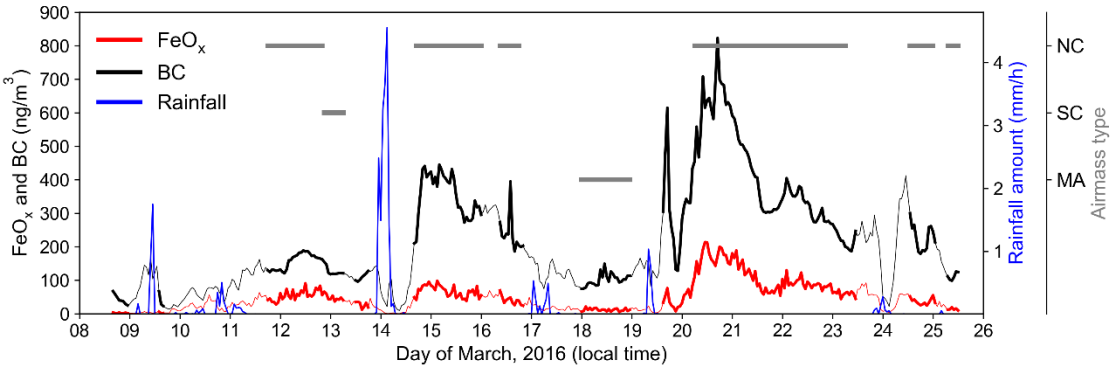


**Figure 3-7.** Time series of the hourly mass concentration of $FeO_x$ and BC aerosols measured by the SP2 and rainfall amount monitored at CHAAMS. The selected and excluded data are expressed as thick and thin lines, respectively. See the text for the data selection procedure. The air mass types classified using backward trajectories are represented by horizontal gray lines: North China (NC), South China (SC), and Marine (MA).

concentrations abruptly increased after rainfall events (14, 19, and 24 March) in association with passages of cold fronts above Okinawa Island (meteorological charts provided by the Japan Meteorology Agency). When frontal systems moved from above the Asian continent toward the East China Sea, air masses influenced by anthropogenic emissions above the continent (synoptic-scale cold air masses on the west side of the cold frontal systems) were generally transported eastward. When these air masses reached at CHAAMS following the passages of the cold fronts (as observed as precipitations), abrupt increases in pollutants were observed. Similar events have been often observed at CHAAMS especially during the winter and spring [*Hatakeyama et al*., 2004; *Liu et al*., 2008].

In order to characterize air masses sampled at CHAAMS in this study, I excluded data, which had been likely affected by precipitations around the observatory, and then I classified data using backward trajectories. The wet removal of aerosols via cloud formation and subsequent precipitation can significantly change the concentrations of $FeO_x$ and BC aerosols. Thus, I excluded data obtained within two hours before or after the precipitations (thin lines in Figure 3-7) to avoid the complications in the data interpretations. Air masses could have been influenced by precipitations in upwind regions, however, only precipitations around the observatory were considered in this study. This is because the air around the cold fronts was considered to have higher chances of influences from precipitations and because there will be large uncertainties in estimations of influences when backward trajectories are used. To confirm the validity of the procedure (exclusion of data) in this study, a scatter plot between the hourly data of BC mass concentration and CO mixing ratio is shown in Figure 3-8. Because CO is not removed by precipitation, deviations from a linear relationship suggest wet removal of BC when common emission ratios and common background concentrations are assumed for BC and CO in all sampled air [*Oshima et al.*, 2012]. In this figure, different symbols are used for excluded and selected data. The selected data points (likely without influences of precipitations) show a relatively tight linear relationship, while excluded data points (likely

with influences of precipitations) show generally lower BC values than those expected from this linear relationship. These results suggested that data with small or negligible influences from wet removal (denoted as "dry air mass" data, hereafter) were successfully extracted by the selection criterion adopted in this study. The slope of correlation for the selected data is 3.94 (ng $m^{-3}$ $ppbv^{-1}$), close to the value of 4.84 (ng $m^{-3}$ $ppbv^{-1}$) obtained by aircraft measurements in the East Asian continental outflow during the spring of 2009 [*Oshima et al*., 2012].

For the next step, I classified dry air masses according to their spatial origin as estimated

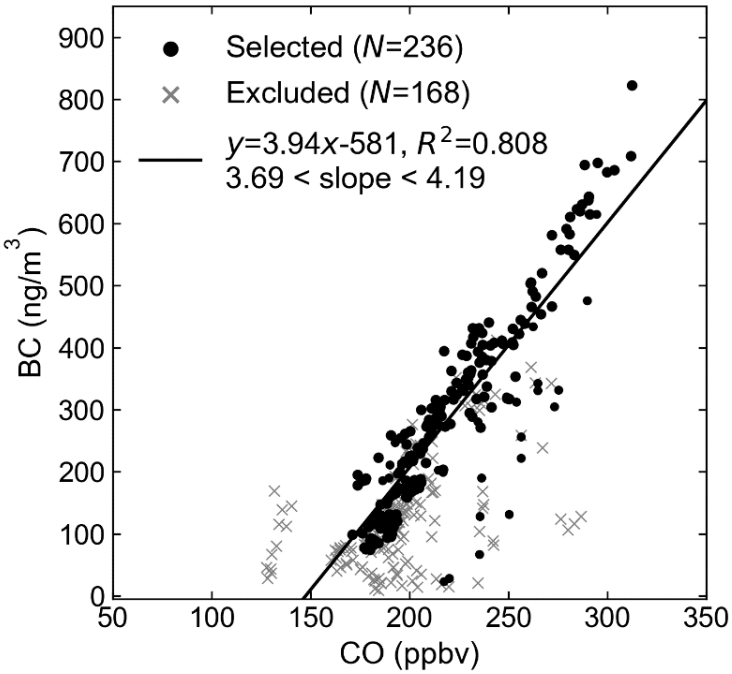


**Figure 3-8.** Scatter plots of the hourly BC mass concentration and CO mixing ratio for selected data and excluded data (the thick and thin lines, respectively, in the BC plot in Figure 3-7); the excluded data were likely influenced by wet removal processes. The selected data points were fitted by a linear function using the least squares method, expressed as the solid line. The 95% confidence interval for the fitting slope is also denoted assuming no statistical error in CO measurement.

by backward trajectory analysis. I made 5-day backward trajectory calculations, using a trajectory model developed at the National Institute of Polar Research [*Tomikawa & Sato*, 2005]. The calculations were started from the location of CHAAMS at a pressure height of 950 hPa (approximately 500 m altitude). I selected this altitude to avoid the trajectory descending to ground level a few hours after the departure. According to lidar measurements made at CHAAMS during the experiment, aerosols were vertically well mixed at altitudes below about 1 km, suggesting the starting point altitude of 500 m is appropriate.

According to the calculated trajectories, I categorized air masses into North China (NC), South China (SC), Marine (MA), and others, the last of which I exclude from the discussion. This categorization is shown in Figure 3-7 (gray horizontal lines), with the classified trajectories shown in Figure 3-9. Air masses that passed through North China and Korea were defined as type NC air masses. Table 3-2 summarizes the total mass concentration of $FeO_x$ (170 nm < $D_m$ < 2100 nm) and BC (70 nm < $D_m$ < 850 nm) aerosols in each air mass type. NC air masses are characterized by high concentrations of $FeO_x$ and BC aerosols. *Zhang et al*. [2009] reported that NC is the dominant emitter of pollutants (e.g., BC and CO) in East Asia. Anthropogenic sources in NC also likely to emit a large amount of $FeO_x$ aerosols, resulting in observed high $FeO_x$ concentrations. After the abrupt enhancements in $FeO_x$ and BC concentrations following the cold front passages, the gradual decreases in concentrations were observed (see Figure 3-7 for the following date ranges: 15–17 and 20–23 March). These tendencies within NC air are interpreted by changes in trajectories from the westerlies to stagnated air due to the development of high pressure.

Air masses that transported from South China were defined as type SC. All the concentrations of CO, BC, and $FeO_x$ were lower in SC air than those in NC air (Table 3-2). As described in section 3.7., however, scatter plot between $FeO_x$ and BC or between $FeO_x$ and CO show that SC data points and NC data points generally lie on similar linear relationship. These results may suggest that differences in concentrations between NC and SC air could be due to

differences in dilution levels.

Air masses that traveled over the Pacific Ocean for more than 1 day and had a warm and humid environment (Table 3-2) were defined as type MA. Both the $FeO_x$ and BC concentrations were lower in this air mass type than those in NC and SC.

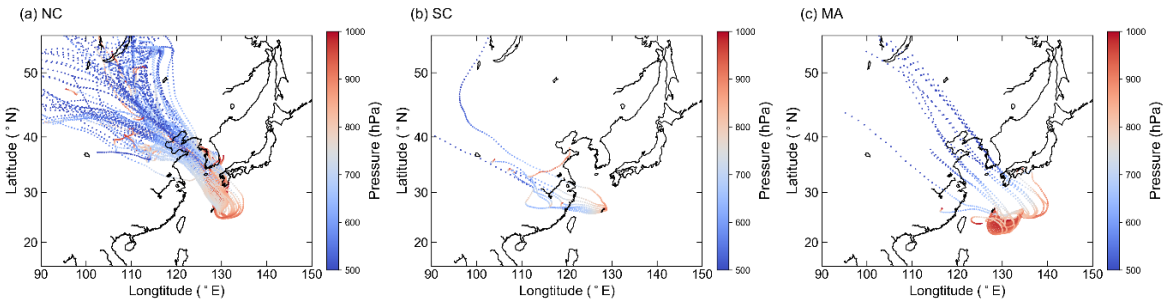


**Figure 3-9.** Backward trajectories from CHAAMS for (a) North China (NC), (b) South China (SC), and (c) Marine (MA) air masses.

**Table 3-2.** Statistics for $FeO_x$ (170 nm < $D_m$ < 2100 nm), BC (70 nm < $D_m$ < 850 nm, and CO in North China (NC), South China (SC), and Marine (MA) air masses[a].

| Species | NC | SC | MA |
|---|---|---|---|
| Temperature (°C)[b] | 17.5 ± 1.60 | 16.50 ± 1.19 | 20.9 ± 1.47 |
| RH (%)[b] | 66.7 ± 6.69 | 67.3 ± 2.81 | 85.9 ± 5.80 |
| $FeO_x$ (ng/m$^3$)[c] | 80.4 ± 42.8 (106 ± 60.3) | 45.5 ± 9.17 (61.3 ± 14.6) | 12.7 ± 4.29 (16.1 ± 6.31) |
| BC (ng/m$^3$) | 331 ± 147 | 123 ± 12.7 | 104 ± 18 |
| CO (ppbv) | 227 ± 31.4 | 187 ± 4.25 | 187 ± 5.86 |

[a]Statistics given as mean ± one standard deviation.

[b]Monitored value at CHAAMS.

[c]Corrected concentrations using the transmission efficiency given in parentheses.

### 3.6.2 Size distribution of $FeO_x$ aerosols

Figure 3-10 shows the size-resolved number and mass concentrations of $FeO_x$ aerosols in each type of air mass along with corrected concentrations using the transmission efficiency described in Section 3.4. The mean corrected size-resolved number and mass concentrations (170 nm < $D_m$ < 2100 nm) are fitted by the power function and bimodal log-normal function, respectively. The formulae of fitting function and fitting coefficients are described in Appendix 3-1. There is no distinct difference in the shapes of size distributions among NC, SC, and MA data in terms of number or mass.

The size-resolved number concentrations are distributed predominantly in the range $D_m$ < ~300 nm, where the transmission efficiency is nearly unity, indicating that particle loss in the transport tube does not affect the number concentration of $FeO_x$ aerosols. However, the number concentration in such small domains was probably underestimated due to the fact that the detection efficiency of $FeO_x$ particles decreases as their size decreases (Figure 2-6). Thus, the modes of number size distributions of ambient $FeO_x$ particles would be smaller than the lower detection limit of the SP2 ($D_m$ = 170 nm). On the other hand, the size-resolved mass concentrations are predominantly distributed in the range $D_m$ > ~800 nm, where the transmission efficiency is less than unity, indicating that a non-negligible number of particles were lost in the transport tube, mostly due to gravitational deposition. In particular, mass concentrations in the upper detection limit ($D_m$ = 2100 nm) were far from zero. Therefore, technical developments to improve the detection efficiency and detectable size range are needed in order to understand the entire size distribution and total mass concentrations of anthropogenic $FeO_x$ aerosols.

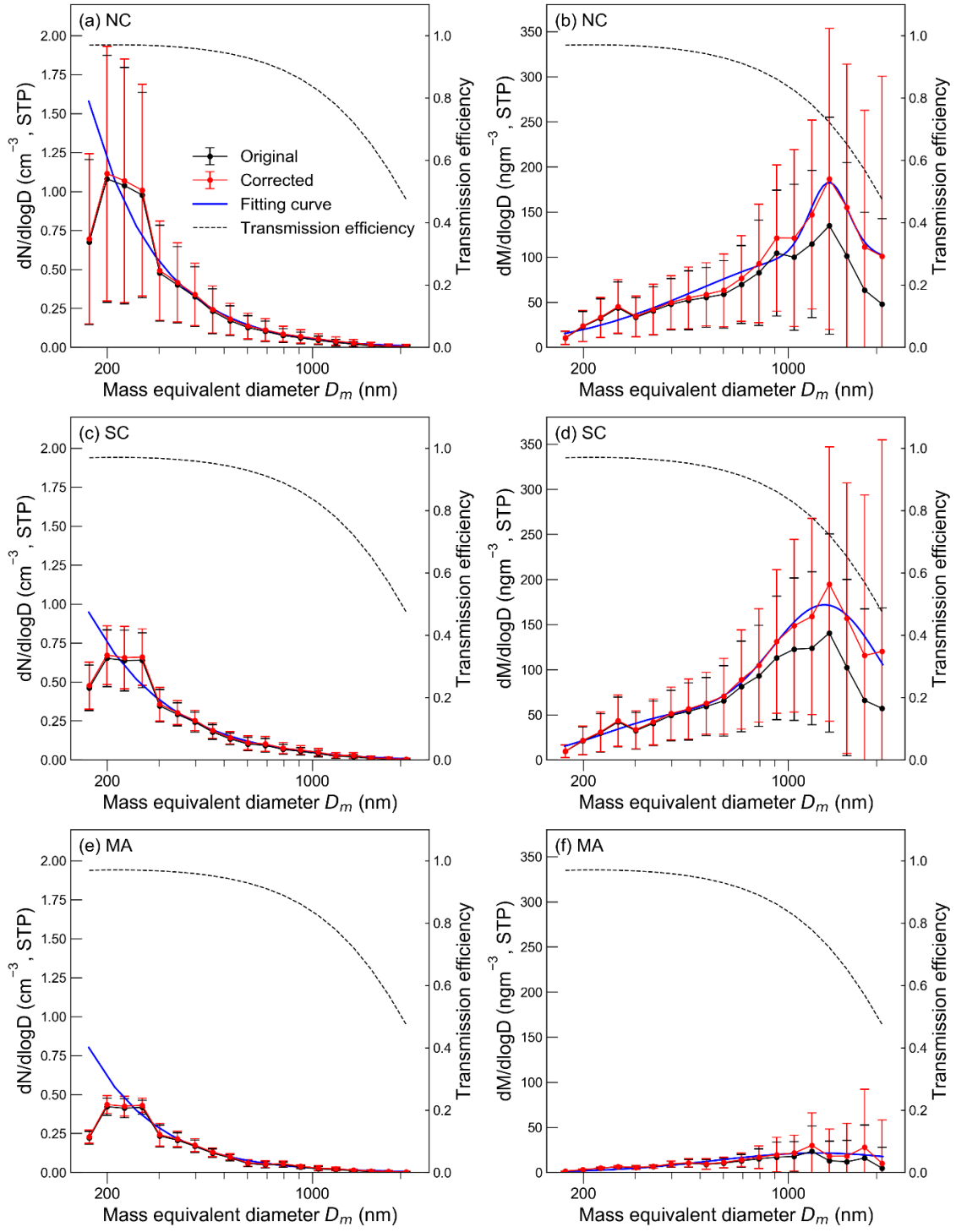


**Figure 3-10.** The mean size-resolved number and mass concentrations of $FeO_x$ aerosols in (a, b) North China (NC), (c, d) South China (SC), and (e, f) Marine (MA) air masses. The fitting curves and the corrected mass concentrations considering sampling efficiency are also depicted. Bars indicate ±1 standard deviation.

Table 3-2 compares the uncorrected and corrected total mass concentrations of $FeO_x$ (170 nm < $D_m$ < 2100 nm) aerosols within observed size ranges. The comparisons of these two values indicate that approximately 20% of $FeO_x$ aerosol mass was lost through the sampling system, largely because of the gravitational loss of large particles. The loss of BC aerosols was negligible because the transmission efficiency of BC in its size range (70 nm < $D_m$ < 850 nm) is almost unity (Figure 3-1b).

### 3.6.3 Correlation of $FeO_x$ concentrations with BC or CO concentrations

Figures 3-11a, b show the correlations of mass concentrations between $FeO_x$ (corrected values) and BC aerosols, as well as between $FeO_x$ aerosols and CO. A unit of mass concentration is used for CO as for $FeO_x$ and BC. In general, a good correlation was found for NC data points in both scatter plots with BC and CO ($R^2$ > 0.7). These results indicate that these $FeO_x$ aerosols are of anthropogenic origin. This result is consistent with the conclusion from microphysical properties measurements described in Section 3.5.2, namely, majority of $FeO_x$ was from anthropogenic emission sources. Furthermore, the observed good correlation indicates that $FeO_x$ sources have similar spatial distributions to those of BC and CO.

SC data points generally lie on the relationships observed for NC data points. These results indicate that emission ratios can be similar between NC and SC areas for $FeO_x$, BC, and CO emissions. MA data points, especially in Figure 3-11b, deviate slightly from NC and SC data points, probably reflecting the efficient removal of $FeO_x$ aerosols relative to CO during long periods of transport.

Applying the developed method to LII produces a time series of 170 hourly points, and permits the construction of scatterplots for analyzing the correlations of mass concentrations (Figure 3-11a,b). The correlation between $FeO_x$ and BC (Figures 3-11a,b) shows that mass concentrations of $FeO_x$ are approximately 30% of those of BC in air masses from China. I use

these correlations to estimate the emission flux of anthropogenic $FeO_x$ aerosols from China in Section 3.7.

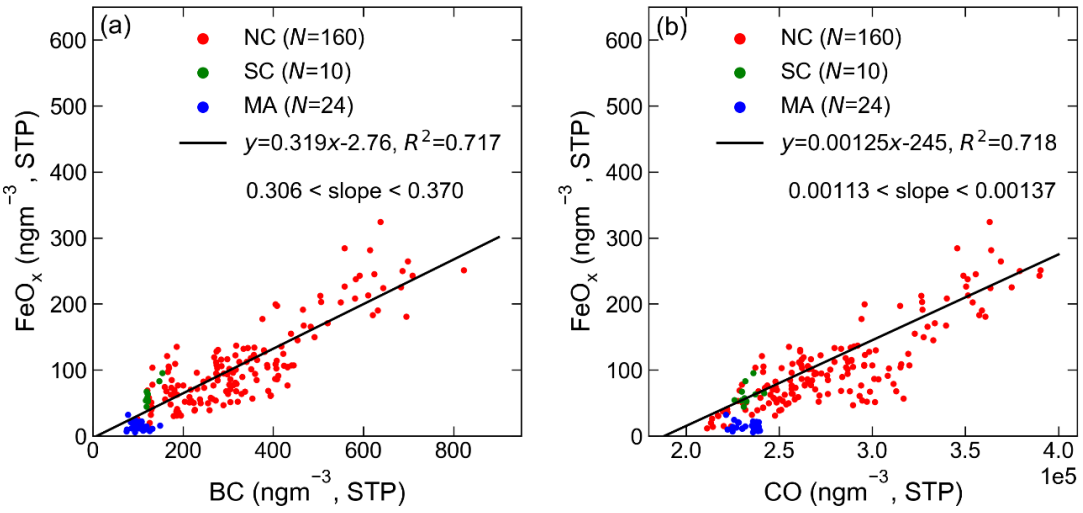


**Figure 3-11.** Correlations of the hourly mass concentrations (a) between corrected values of $FeO_x$ and BC and (b) between corrected values of $FeO_x$ and CO, for North China (NC), South China (SC), and Marine (MA) air masses. Black lines represent the linear function fitting the set of NC plus SC data points using the least squares method. 95% confidence intervals for the fitting slopes are also denoted assuming no statistical error in BC and CO measurements. Mass concentrations of CO are converted from mixing ratio values.

## 3.7 Emission strengths of anthropogenic $FeO_x$ aerosols

I estimated the annual emission flux of anthropogenic $FeO_x$ aerosols from China ($F_{FeOx}$) using a top-down method. I derived the flux in two ways, $F_{FeOx(BC)}$ and $F_{FeOx(CO)}$, with respectively observationally constrained emission ratios $F_{FeOx}/F_{BC}$ and $F_{FeOx}/F_{CO}$. $F_{BC}$ and $F_{CO}$ are emission fluxes of BC and CO from China, and values reported in previous studies were used [*Hoesly et al.* (2018)]. These emission ratios can be approximated as ratios of mass concentrations (after subtracting background values) spatially averaged over China as follows: $M_{FeOx,China}/M_{BC,China}$ and $M_{FeOx,China}/M_{CO,China}$. In this approximation, I assumed that $M_{FeOx,China}$, $M_{BC,China}$, and $M_{CO,China}$ are sourced only from emissions in China, since China is the dominant source of pollutant emissions to the boundary layer in this region [*Zhang et al.*, 2009]. To estimate the mass concentration ratios, I used the correlation slopes of mass concentrations between $FeO_x$ and BC, as well as between $FeO_x$ and CO, for NC plus SC data observed at CHAAMS, since these air masses contain a mixture of the pollutants emitted from sources throughout China. The mass concentration ratios of pollutants emitted from China and observed at CHAAMS were $M_{FeOx,CHAAMS}/M_{BC,CHAAMS} = 0.319$ and $M_{FeOx,CHAAMS}/M_{CO,CHAAMS} = 0.00125$ (Figure 3-11). However, the mass concentrations of these pollutants might have changed appreciably during transport due to dry deposition and chemical reactions. Thus, I also assessed $M_{FeOx,China}$, $M_{BC,China}$, and $M_{CO,China}$, as well as their ratios, considering the lifetimes of $FeO_x$, BC, and CO. For $FeO_x$ and BC aerosols, I calculated size-dependent dry deposition velocity using the method described in *Seinfeld & Pandis* (2006) (Section 3.10). I ignored the potential effects of wet removal because data for air masses that were likely influenced by wet removal were excluded (Section 3.6.1). The calculated size-dependent dry deposition velocities for $FeO_x$ and BC are described in Figure 3A-1. Submicron BC aerosols are removed preferentially compared with $FeO_x$ aerosols, predominantly due to Brownian diffusion. Impaction and interception, which could be efficient removal processes for super-micron particles such as $FeO_x$ aerosols over rough surfaces (e.g., soil), are not effective over smooth

surfaces considered here, namely the ocean. In this calculation of the dry deposition flux of aerosols, I considered the system as a Lagrangian air parcel within which particles were well mixed in a 1 km thick boundary layer (based on vertical aerosol profiles monitored by a polarized lidar installed in CHAAMS). Figure 3A-2a shows the transport history of the correlation slope of mass concentrations between $FeO_x$ and BC aerosols (i.e., $M_{FeOx}/M_{BC}$). The values increase with transport time, reflecting the efficient removal of BC aerosols compared with that of $FeO_x$ aerosols. Because the trajectory analysis shows that NC and SC air masses needed ~3 days to arrive at CHAAMS from the coastline of the Asian continent, I used a value for $M_{FeOx,China}/M_{BC,China}$ ($= F_{FeOx}/F_{BC}$) of 0.269, that is, the projected value at a time 3 days prior. For CO, I calculated the history of mass concentration assuming a lifetime of 2 months [*Hauglustaine et al*., 1998]. Figure 3A-2b shows calculated transport histories of correlation slope between $FeO_x$ aerosols and CO (i.e., $M_{FeOx}/M_{CO}$). The values decreased with transport time, reflecting that $FeO_x$ aerosols were preferentially removed compared with CO. I used $M_{FeOx,China}/M_{CO,China}$ ($= F_{FeOx}/F_{CO}$) = 0.00152, the projected value at a time 3 days prior. For $F_{BC}$ and $F_{CO}$ in the derivation of $F_{FeOx(BC)}$ and $F_{FeOx(CO)}$, I used values of 2.53 Tg/yr and 193 Tg/yr, respectively, from anthropogenic emission inventories of China for the base year of 2014 as described in *Hoesly et al.* (2018).

From these assumptions and data, I estimated $F_{FeOx(BC)}$ ($\equiv F_{FeOx}/F_{BC} \times F_{BC}$) and $F_{FeOx(CO)}$ ($\equiv F_{FeOx}/F_{CO} \times F_{CO}$) as 0.49 FeTg/yr and 0.21 FeTg/yr, respectively. The mass of $FeO_x$ was converted to the mass of Fe by multiplying by the elemental Fe mass ratio of magnetite ($Fe_3O_4$), that is, 0.7236. Although $F_{FeOx(BC)}$ and $F_{FeOx(CO)}$ were derived using different data, they agree to within a factor of ~2.

Emission inventories of Fe-containing aerosols from fossil fuel and biofuel combustion, biomass burning, and mineral dust have been made in previous studies using a bottom-up method that combines fuel consumption, emission factors, and Fe content in emitted aerosols [*Ito*, 2013; *Ito et al.*, 2018; *Luo et al.*, 2008; *Wang et al.*, 2015]. The global emission flux of

anthropogenic Fe (from fossil fuel) in $PM_{10}$ was reported to be 0.66 FeTg/yr in 1996 by *Luo et al*. (2008), 0.51 FeTg/yr in 2001 by *Ito* (2013), and 0.87 FeTg/yr in 2001 by *Wang et al*. (2015). Recently, *Ito et al.* (2018) updated global Fe emission flux in $PM_{10}$ from fossil fuel and biofuel to 1.91 FeTg/yr by using recent emission data from anthropogenic sources.

Before discussing my estimate of $F_{FeOx}$ with currently reported emission fluxes mentioned above, it should be noted that my estimates of $F_{FeOx}$ consider those $FeO_x$ particles having 170–2100 nm of mass-equivalent diameter ($D_m$), which corresponds to 380–4000 nm in aerodynamic diameter, assuming a density of 5.17 g/cm$^3$ and a shape factor of 1.5. The observed size-resolved mass concentration (Figure 3-10) implies that a non-negligible quantity of $FeO_x$ particles with $D_m > 2100$ nm could be emitted. If the size distribution of $FeO_x$ particles with $D_m > 2100$ nm follows the fitting curve shown in Figure 3-10, the $M_{FeOx}$ and $F_{FeOx}$ values in $PM_{10}$ increased by a factor of 1.4.

It should also be noted that the emission inventories mentioned above represent total Fe emission flux, which includes both $FeO_x$ and non-$FeO_x$ aerosols; for example, fly ash particles from coal combustion contain $FeO_x$ and Fe substituted in aluminosilicate glass (structural iron) [e.g., *Chen et al.*, 2012]. In this study, I assume the mass ratio of $FeO_x$ in total iron aerosols to be 0.4 (0.2–0.8) because of the following. First, as described in Chapter 4, the SP2 was used to measure $FeO_x$ aerosol in Chiba, where ICP-MS was simultaneously used to measure iron aerosols. The mass concentration ratio of $FeO_x$ (measured by SP2) to total iron (measured by ICP-MS) was 25%–47% for particles with $D_m$ = 170–320 nm in airmasses strongly influenced by steel plant emission, and 42–91% for the same particles in airmasses not influenced. Second, *Yu et al*. (2012) used Mössbauer Spectroscopic analysis to show that magnetite accounted for 40%–50% of total iron in terms of the mole fraction of iron in iron-containing minerals in coal ash. Third, *Zeng et al.* (2009) showed that the fraction of magnetite to total iron was 14%–32% in their coal combustion samples.

From these considerations, my estimates of the emission flux of anthropogenic Fe ($F_{Fe(BC)}$ and $F_{Fe(CO)}$) in $PM_{10}$ emitted from China are respectively 1.7 and 0.74 FeTg/yr, which are simply the values of $F_{FeOx(BC)}$ and $F_{FeOx(CO)}$ (i.e., 0.49 and 0.21 FeTg/yr, respectively) directly obtained from my observation multiplied by a factor of 3.5 (1.4 × 1/0.4). Although my estimated $F_{Fe}$ (1.7 and 0.74 FeTg/yr) contains only emissions from China, it is comparable to the global values derived from the bottom-up methods mentioned above [*Ito* 2013; *Ito et al*., 2018; *Luo et al*., 2008; *Wang et al*., 2015] (0.51–1.91 FeTg/yr, Table 3-3). *Wang et al*. (2015) reported that combustion emissions of Fe-containing aerosols from China have constituted ~50% of global Fe emissions in recent years. By hypothesizing that the global emission flux of anthropogenic Fe aerosols is 200% of the emission flux from China, my estimates of $F_{Fe}$ are extrapolated to global values of $F_{Fe(BC),global}$ = 3.4 FeTg/yr and $F_{Fe(CO),global}$ = 1.4 FeTg/yr.

The uncertainies of $F_{Fe}$ are estimated by integrating (root sum square) the following five factors. The fisrt is uncertainty in derivation of $FeO_x$ particle mass from peak incandescence signal ($S_i$). The difference in particle mass by using magnetite and hematite calibration curve (mass VS $S_i$) for large size ($D_m$ > ~300 nm) is approximately 3%. Thus, I assumed the uncertainty as ±1.5% (half value). The second is uncertainty in the derivation of $M_{FeOx}/M_{BC}$

**Table 3-3.** Global emission strength of anthropogenic Fe.

| | | Emission strength (FeTg/yr) | Base year |
|---|---|---|---|
| Bottom-up | *Ito et al.* 2013 | 0.51 | 2001 |
| | *Luo et al.* 2008 | 0.66 | 1996 |
| | *Wang et al.* 2015 | 0.87 | 2001 |
| | *Ito et al.* 2018 | 1.91 | Recent |
| Top-down | This study | 3.4 ± 3.7 (using BC data)<br>1.4 ± 1.1 (using CO data) | 2014 |

($M_{FeOx}/M_{CO}$) from the correlation slope. In this study, half values of 95% confidence interval for correlation slopes were defined as the uncertainties (±11.6 % for $M_{FeOx}/M_{BC}$ and ±27.0% for $M_{FeOx}/M_{CO}$). The third is uncertainty in correcting the mass ratio $M_{FeOx}/M_{BC}$ ($M_{FeOx}/M_{CO}$) by considering dry deposition. I used ±38% for $M_{FeOx}/M_{BC}$ and ±11% for $M_{FeOx}/M_{CO}$, which are estimated in Appendix 3-2. The forth is uncertainty of emission strength $F_{BC(CO)}$. I used half value of the uncertainty of $F_{BC}$ (−43% to +93%; *Hosely et al.*, 2018, *Lu et al*., 2011). I did not consider the uncertainty of $F_{co}$ because it was not specified in *Hoesly et al.* (2018). The final is uncertainty of the mass ratio of $FeO_x$ in total iron aerosols 0.4 (0.2–0.8). I used ±75% as uncertainty, which is half value of percentage uncertainty.

By integrating the uncertainties, my estimates of $F_{Fe(BC),global}$ and $F_{Fe(CO),global}$ are 3.4 (±3.7) FeTg/yr and 1.4 (±1.1), respectively. Despite of the large uncertainty, $F_{Fe(BC),global}$ might be larger than global emission fluxes reported in the emission inventories by bottom-up methods (0.51–1.91 FeTg/yr). This estimate implies that the currently reported estimates on $F_{Fe,global}$ by the bottom-up methods without any tuning by quantitative abundance data of ambient iron aerosols are underestimated. *Wang et al*. (2015) pointed out that major uncertainties remain in Fe emission inventories due to the scarcity of observational studies constraining the Fe content in aerosols from individual emission sources. Furthermore, other potential $FeO_x$ sources have not been considered in the current Fe inventories, such as wearing of automotive brakes [*Kukutschová* et al., 2011]. Further observational studies may reduce the uncertainties of the emission flux of anthropogenic Fe and are needed for quantitative evaluations of their impacts on atmospheric radiation and ocean biogeochemistry.

## 3.8 Summary

Ground-based aerosol observations at CHAAMS, Okinawa Island, Japan, were performed in March 2016. Using the technique developed in this study, the size-resolved number and mass concentrations of $FeO_x$ aerosols were obtained.

Based on the quantities measured by the SP2 (color ratio, incandescence onset position, and scattering cross section), and the particle morphologies and compositions analyzed by TEM, most of the observed $FeO_x$ aerosols were identified as anthropogenic origin that was externally or internally mixed with other aerosol compounds (e.g., sulfates and organics). The developed LII enabled a time series of 170 hourly data points for mass and number concentrations of anthropogenic $FeO_x$ aerosols, as well as for their size distributions. The time resolution (1 hour) is much shorter than that obtainable using filtration methods (several days). The statistically significant mass concentration data obtained in this study enabled me to obtain clear positive correlations between the mass concentrations of $FeO_x$ and BC ($R^2 = 0.717$) and of $FeO_x$ and CO ($R^2 = 0.718$) in air masses originating from China. These correlations indicate that the emission sources of $FeO_x$ aerosols are spatially similar to those of BC and CO in China. From the correlation between $FeO_x$ and BC, I conclude that the mass concentration of $FeO_x$ aerosols from China is approximately 30% of that of BC.

Based on the slope of the correlation between the mass concentrations of $FeO_x$ and BC, I estimated the annual emission flux of anthropogenic $FeO_x$ aerosols from China to be 0.49 FeTg/yr. An alternative estimate of 0.21 FeTg/yr was obtained from the slope of the correlation between the mass concentrations of $FeO_x$ and CO. These results imply that currently reported emission inventories of anthropogenic Fe are underestimated. Furthermore, current model simulations using these inventories could underestimate the effect of anthropogenic $FeO_x$ aerosols on iron supply to the surface ocean. To obtain an accurate inventory, additional observational datasets of anthropogenic $FeO_x$ aerosols should be collected in other locations. In Chapter 4, I discuss the abundance of $FeO_x$ aerosols observed in other locations including East Asian continental outflow, urban city, and the Arctic region.

## Appendix 3-1: Fitting of size distribution

The power function fitted to size-resolved number concentration is

$$\frac{\mathrm{d}N}{\mathrm{d}\log D_m} = y_0 + aD_m^{-p}, \tag{3A-1}$$

where $y_0, a,$ and $p$ are fitting coefficients summarized in Table 3A-1 for each air mass type. The bimodal log-normal function fitted to size-resolved number concentration is

$$\frac{\mathrm{d}M}{\mathrm{d}logD_m} = \sum_{i=0}^{1} A_i \exp\left[-\frac{\log^2(D_m/D_i)}{2\log^2\sigma_{g,i}}\right], \tag{3A-2}$$

where $A_i$, $D_i$, and $\sigma_{g,i}$ are fitting parameters listed in Table 3A-1.

**Table 3A-1.** List of the parameters used to fit size-resolved number and mass concentrations of $FeO_x$ aerosols.

| Air mass type | $y_o$ | $a$ | $p$ | $A_0$ | $A_1$ | $D_0$ | $D_1$ | $\sigma_{g,0}$ |
|---|---|---|---|---|---|---|---|---|
| NC | −0.005291 | 26660 | −1.888 | 76.54 | 106.3 | 1376 | 1470 | 0.06399 |
| SC | −0.011586 | 3523 | −1.593 | 47.69 | 163.6 | 433.7 | 1372 | 0.2635 |
| MA | −0.002159 | 12000 | −1.865 | 77.22 | 21.4 | 0.0001 | 1259 | 0.8094 |

## Appendix 3-2: Dry deposition velocity $FeO_x$ and BC aerosols

Dry deposition flux of aerosol well mixed in an air mass during transport from the emission source to the observatory is expressed as

$$F(D_m) = v(D_m)M(D_m), \tag{3A-3}$$

where $v$ is the dry deposition velocity and $M$ is the mass concentration of aerosol with specified size ($D_m$). When the height of the air mass is $h$, the time variation of $M$ is

$$\frac{dM(D_m)}{dt} = -\frac{F(D_m)}{h} = -\frac{v(D_m)}{h}M(D_m) \tag{3A-4}$$

$$M(D_m) = M_0 \exp -\frac{v_d}{h}t, \tag{3A-5}$$

where $M_0$ is $M_0(D_m, t = 0)$.

I calculated the dry deposition velocity $v_d$ using a resistance model [*Seinfeld and Pandis*, 2006]. In the calculation, I assumed Pasquill stability class to be C (slightly unstable). I also assumed the following parameters by referring to previous studies. The uncertainties are defined as plausible values for boundary layers over the ocean (smooth surface).

Roughness length was assumed to be $10^{-3}$ ($10^{-5}$–$10^{-2}$) m (smooth sea; *Seinfeld and Pandis* 2006). The characteristic radius of collectors was assumed to be 5 (2–10) mm (*Zhang et al.* 2001). The friction velocity was assumed to be 0.3 (0.01–0.6) m/s, a typical value for the boundary layer over the ocean (*Jones and Schroeder* 1977; *Weber* 1999). Parameters in collection efficiencies from Brownian diffusion and impaction are as reported in *Zhang et al.* (2001) for the ocean category.

Using these assumptions, deposition velocity for $FeO_x$ and BC were calculated (Figure 3A-1). Based on the deposition velocity and Equation 3A-5, I estimated the correlation slopes for $FeO_x$ VS BC and $FeO_x$ VS CO when the backward time is 3 days as 0.269 (0.153–0.325) 0.00153 (0.00135–0.00169) (Figure 3A-2). The uncertainty of correlation slope represents calculated range using the parameters within their uncertainties.

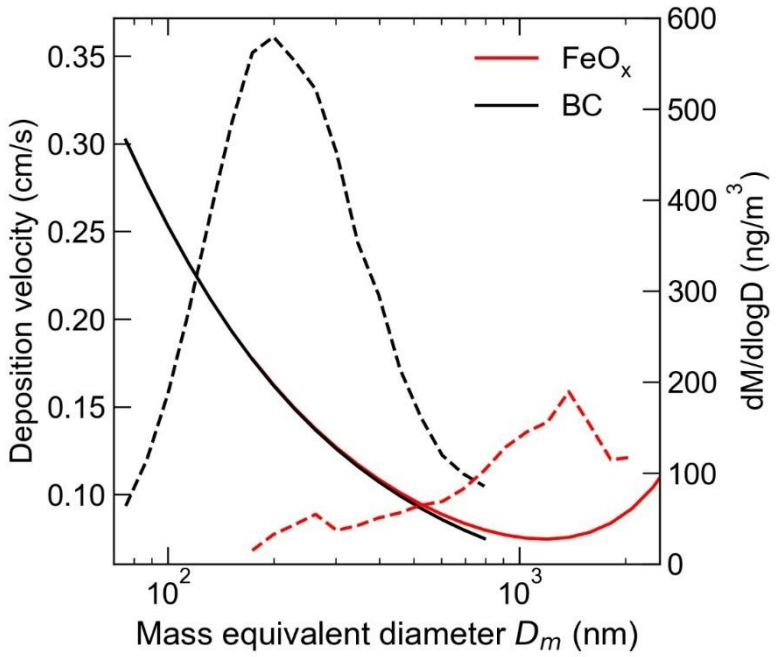


**Figure 3A-1.** Size-dependent deposition velocities of $FeO_x$ and BC aerosols over the ocean (solid lines). The mean size-resolved mass concentrations of BC and $FeO_x$ aerosols in NC and SC air masses are also shown (dashed lines of corresponding colors).

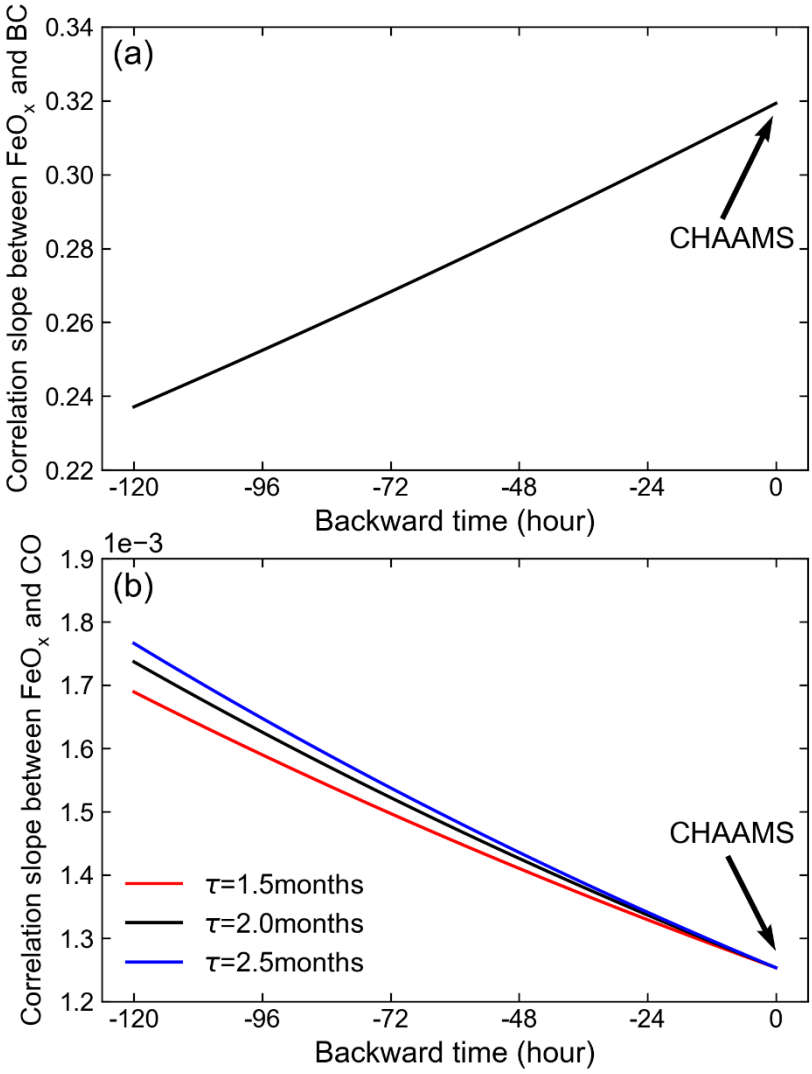


**Figure 3A-2.** Transport history of the correlation slope of mass concentrations between (a) $FeO_x$ and BC aerosols and (b) $FeO_x$ aerosols and CO in North China (NC) plus South China (SC) air masses. In (b), I depict three results by assuming different lifetimes of CO $\tau$.

## References

Adachi, K., Moteki, N., Kondo, Y., & Igarashi, Y. (2016). Mixing states of light-absorbing particles measured using a transmission electron microscope and a single-particle soot photometer in Tokyo, Japan, *Journal of Geophysical Research: Atmospheres*, *121*(15), 9153–9164, doi:10.1002/2016JD025153

Adachi, K., Sedlacek, A. J., Kleinman, L., Chand, D., Hubbe, J. M., & Buseck, P. R. (2018). Volume changes upon heating of aerosol particles from biomass burning using transmission electron microscopy, *Aerosol Science and Technology*, *52*(1), 46-56, DOI: 10.1080/02786826.2017.1373181

Chan, C. K., & Yao, X. (2008). Air pollution in mega cities in China. *Atmospheric environment*, *42*(1), 1-42.

Chen, H., Laskin, A., Baltrusaitis, J., Gorski, C. A., Scherer, M. M., & Grassian, V. H. (2012). Coal fly ash as a source of iron in atmospheric dust., *Environmental Science & Technology*, *46*(4), 2112-20, doi:10.1021/es204102f

Crosson, E. R. (2008). A cavity ring-down analyzer for measuring atmospheric levels of methane, carbon dioxide, and water vapor, *Applied Physics B*, *92*(3), 403-408, doi:10.1007/s00340-008-3135-y

Furutani, H., Jung, J., Miura, K., Takami, A., Kato, S., Kajii, Y., & Uematsu, M. (2011). Single-particle chemical characterization and source apportionment of iron-containing atmospheric aerosols in Asian outflow, *Journal of Geophysical Research: Atmospheres*, *116*(D18), doi:10.1029/2011JD015867

Hatakeyama, S., Takami, A., Sakamaki, F., Mukai, H., Sugimoto, N., Shimizu, A., & Bandow, H. (2004). Aerial measurement of air pollutants and aerosols during 20–22 March 2001 over the East China Sea, *Journal of Geophysical Research: Atmospheres, 109*(D13), doi:10.1029/2003JD004271

Hauglustaine, D. A., Brasseur, G. P., Walters, S., Rasch, P. J., Müller J.-F., Emmons, L. K., &

Carroll, M. A. (1998). MOZART, a global chemical transport model for ozone and related chemical tracers: 2. Model results and evaluation, *Journal of Geophysical Research: Atmospheres*, *103*(D21), 28291-28335, doi:10.1029/98JD02398

Hoesly, R. M., Smith, S. J., Feng, L., Klimont, Z., Janssens-Maenhout, G., Pitkanen, T., Seibert J. J., Vu, L., et al. (2018) Historical (1750–2014) anthropogenic emissions of reactive gases and aerosols from the Community Emissions Data System (CEDS), *Geoscientific Model Development*, *11*(1), 369-408, doi:10.5194/gmd-11-369-2018.

Ito, A. (2013). Global modeling study of potentially bioavailable iron input from shipboard aerosol sources to the ocean, *Global Biogeochemical Cycles*, *27*(1), 1-10, doi:10.1029/2012GB004378

Ito, A., G. Lin, & J. Penner (2018), Radiative forcing by light-absorbing aerosols of pyrogenetic iron oxides, *Scientific Reports*, *8*(1), 7347, doi:10.1038/s41598-018-25756-3.

Jones, W. L., & Schroeder, L. C. (1978). Radar backscatter from the ocean: Dependence on surface friction velocity. *Boundary-Layer Meteorology*, *13*(1-4), 133-149.

Li, W., Xu, L., Liu, X., Zhang, J., Lin, Y., Yao, X., Gao, H., Zhang, D., et al. (2017). Air pollution–aerosol interactions produce more bioavailable iron for ocean ecosystems, *Science Advances*, *3*(3), e1601749, doi:10.1126/sciadv.1601749

Liu, C.-M., Yeh, M.-T., Paul, S., Lee, Y.-C., Jacob, D. J., Fu, M., Woo, J.-H., Carmichael, G. R. & Streets, D. G. (2008). Effect of anthropogenic emissions in East Asia on regional ozone levels during spring cold continental outbreaks near Taiwan: A case study, *Environmental Modeling & Software*, *23*(5), 579-591, doi:10.1016/j.envsoft.2007.08.007

Lu, Z., Zhang, Q., & Streets, D. G. (2011): Sulfur dioxide and primary carbonaceous aerosol emissions in China and India, 1996–2010, *Atmos. Chem. Phys*., *11*, 9839-9864, https://doi.org/10.5194/acp-11-9839-2011

Luo, C., Mahowald, N., Bond, T., Chuang, P., Artaxo, P., Siefert, R., Chen, Y., & Schauer, J.

(2008). Combustion iron distribution and deposition, *Global Biogeochemical Cycles*, *22*(1), doi:10.1029/2007GB002964

Matsui, H., Mahowald, N., Moteki, N., Hamilton, D., Ohata, S., Yoshida, A., Koike, M., Scanza, R., & Flanner, M. (2018). Anthropogenic combustion iron as a complex climate forcer, *Nature Communications*, *9*(1), 1593, doi:10.1038/s41467-018-03997-0.

Moffet, R., Furutani, H., Rödel, T., Henn, T., Sprau, P., Laskin, A., Uematsu, M., & Gilles, M. (2012). Iron speciation and mixing in single aerosol particles from the Asian continental outflow, *Journal of Geophysical Research: Atmospheres*, *117*(D7), doi:10.1029/2011JD016746

Moteki, N., Adachi, K., Ohata, S., Yoshida, A., Harigaya, T., Koike, M., & Kondo, Y. (2017). Anthropogenic iron oxide aerosols enhance atmospheric heating., *Nature Communications*, *8*, 15329, doi:10.1038/ncomms15329

Oshima, N., Kondo, Y., Moteki, N., Takegawa, N., Koike, M., Kita, K., Matsui, H., Kajino, M., et al. (2012). Wet removal of black carbon in Asian outflow: Aerosol radiative forcing in East Asia (A-FORCE) aircraft campaign, *Journal of Geophysical Research: Atmospheres*, *117*(D3), doi:10.1029/2011JD016552

Qu, Y., Yang, Y., Zou, Z., Zeilstra, C., Meijer, K., & Boom, R. (2014). Thermal decomposition behavior of fine iron ore particles. *ISIJ International*, *54*(10), 2196-2205.

Sanderson, P., Su, S. S., Chang, I. T. H., Saborit, J. M., Kepaptsoglou, D. M., Weber, R. J. M., & Harrison, R. (2016). Characterisation of iron-rich atmospheric submicrometre particles in the roadside environment, *Atmospheric Environment*, *140*, 167-175, doi:10.1016/j.atmosenv.2016.05.040

Seinfeld, J.H., & Pandis, S.N. (2006). Atmospheric Chemistry and Physics: From *Air Pollution to Climate Change. 2nd Edition*, John Wiley & Sons, New York, 1152 pp.

Shimizu, A., Sugimoto, N., Matsui, I., Arao, K., Uno, I., Murayama, T., Kagawa, N., Aoki, K., Uchiyama, A., & Yamazaki, A. (2004). Continuous observations of Asian dust and other

aerosols by polarization lidars in China and Japan during ACE-Asia, *Journal of Geophysical Research: Atmospheres*, *109*(D19), doi:10.1029/2002JD003253

Takahama, S., Gilardoni, S., & Russell, L. (2008). Single-particle oxidation state and morphology of atmospheric iron aerosols, *Journal of Geophysical Research: Atmospheres*, *113*(D22), doi:10.1029/2008JD009810

Tomikawa, Y., & Sato, K. (2005). Design of the NIPR trajectory model, *Polar Meteorology and Glaciology*, 19, 120-137.

Wang, R., Balkanski, Y., Boucher, O., Bopp, L., Chappell, A., Ciais, P., Hauglustaine, D., Peñuelas, J., & Tao, S. (2015). Sources, transport and deposition of iron in the global atmosphere, *Atmospheric Chemistry and Physics*, 15, 6247-6270, doi:10.5194/acp-15-6247-2015

Weber, R. O. (1999). Remarks on the definition and estimation of friction velocity. *Boundary-Layer Meteorology*, *93*(2), 197-209.

Yoshida, A., Moteki, N., Ohata, S., Mori, T., Tada, R., Dagsson-Waldhauserová, P., & Kondo, Y. (2016). Detection of light-absorbing iron oxide particles using a modified single-particle soot photometer, *Aerosol Science and Technology*, *50*(3), 1-4, doi:10.1080/02786826.2016.1146402

Zellweger, C., Steinbacher, M., & Buchmann, B., (2012). Evaluation of new laser spectrometer techniques for in-situ carbon monoxide measurements, *Atmospheric Measurement Techniques*, *5*(10), 2555-2567, doi:10.5194/amt-5-2555-2012

Zhang, L., Gong, S., Padro, J., & Barrie, L. (2001). A size-segregated particle dry deposition scheme for an atmospheric aerosol module, *Atmospheric Environment*, *35*(3), 549-560, doi:10.1016/s1352-2310(00)00326-5

Zhang, Q., Streets, D. G., Carmichael, G. R., He, K. B., Huo, H., Kannari, A., Kilmont Z., Park, I. S., et al. (2009). Asian emissions in 2006 for the NASA INTEX-B mission, *Atmospheric Chemistry and Physics*, *9*(14), 5131-5153, doi:10.5194/acp-9-

5131-2009

Yu, D., Zhao, L., Zhang, Z., Wen, C., Xu, M., & Yao, H. (2012). Iron transformation and ash fusibility during coal combustion in air and O2/CO2 medium. *Energy & Fuels*, *26*(6), 3150-3155.

Zhang, X. L., Wu, G. J., Zhang, C. L., Xu, T. L., & Zhou, Q. Q. (2015). What's the real role of iron-oxides in the optical properties of dust aerosols? *Atmospheric Chemistry and Physics Discussion*, *15*(4), 5619-5662, doi:10.5194/acpd-15-5619-2015.

# 4 Abundance of iron oxide aerosols in the northern hemisphere

## 4.1 Introduction

Anthropogenic iron aerosols have drawn attention because they are bioavailable and thus have an important role in ocean biogeochemistry and the global carbon budget. In addition, anthropogenic iron aerosols may have important role in atmospheric because magnetite and hematite, the main component of anthropogenic iron aerosols [*Magiera et al.*, 2011, *Sanderson et al.,* 2016], strongly absorb visible light [*Zhang et al*., 2015].

Atmospheric abundances of anthropogenic iron aerosols are simulated using an aerosol transport model [*Luo et al*., 2008, *Wang et al*., 2015, *Ito et al*., 2018]. These studies calculated the abundances based on the emission inventories of anthropogenic iron aerosols estimated by the bottom-up method. However, current estimations have large uncertainties due to a lack of observational data. Although observations of bulk mass concentrations of anthropogenic iron aerosols are needed, observations of microphysical properties such as size distribution and mixing state are also needed because these properties affect aerosol lifetime (dry deposition and wet removal), light absorption (e.g. absorption cross section), and iron bioavailability for phytoplankton [*Jacobson*, 2000, *Chen et al*., 2012, *Bond et al*., 2013].

In this chapter, measured data for $FeO_x$ aerosols in eight observation campaigns in the northern hemisphere obtained by the developed LII are analyzed. The majority of the measured $FeO_x$ aerosols were found to be anthropogenic. Mass and number concentrations, size distribution, and mixing state of such $FeO_x$ aerosols are shown. In addition, I will show that the concentration of $FeO_x$ aerosols is well correlated with BC and CO in all observation, suggesting that emission sources of these pollutants are spatially similar.

## 4.2 Observation datasets

I analyzed observational datasets obtained from five ground measurements including Hedo observation (CHAAMS, Chapter 3) and three aircraft measurements (Figure 4-1 and Table 4-1). These observation sites cover three regions in the northern hemisphere: the East Asian continental outflow (A-FORCE 2009, 2013W, Hedo, and Fukue), urban cities (Tokyo and Chiba), and the Arctic region (Ny-Ålesund and PAMARCMiP 2018). In all observations, the identical SP2 was used. Thus, the same analysis procedure for $FeO_x$ and BC particles using the developed LII (Chapter 2, 3) can be applied to the all observational data. In addition, CO was measured using a Picarro G2401 $CO/CH_4/CO_2/H_2O$ analyzer (Picarro Inc., USA) in A-FORCE 2009 and 2013W, Hedo, Fukue, and Chiba.

Aerosol Radiative Forcing in East Asia (A-FORCE) 2009 and 2013W are aircraft campaigns conducted over Yellow Sea and East China Sea (*Oshima et al.*, 2012, *Kondo et al.*, 2016). Fukue observation was conducted in April 2019. The observation site is located on Fukue Island (32.8 °N, 128.7 °E), 1,460 km southeast of Beijing and 740 km east of Shanghai [*Takami et al.*, 2005]. Tokyo observation was conducted in a building on the Hongo campus of the University of Tokyo, located in the Tokyo Metropolitan Area [*Ohata et al.*, 2018]. Chiba

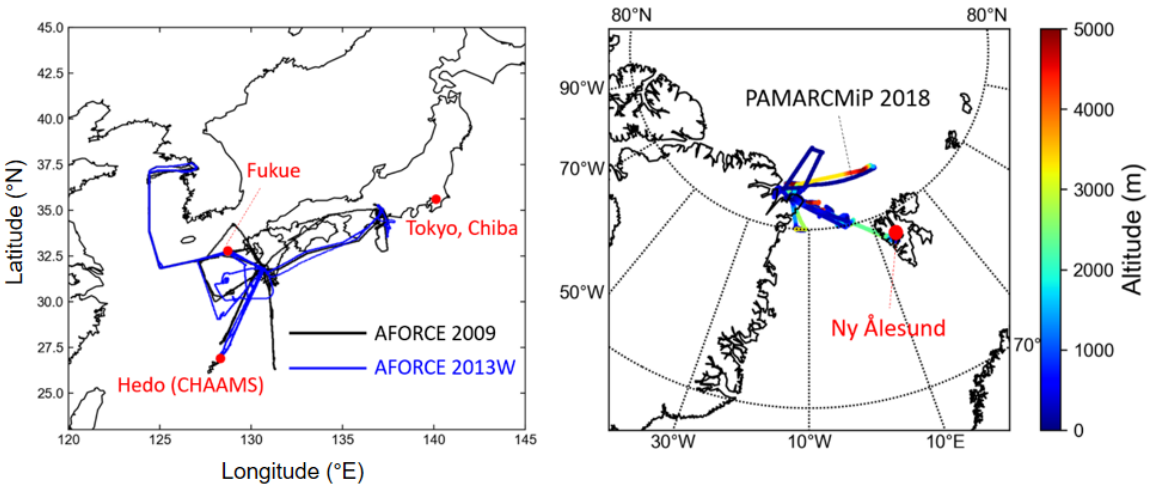


**Figure 4-1.** Location of observation sites and flight tracks (left: East Asia continental outflow; right: Arctic region).

observation was conducted in a building of the Chiba City Hall center [*Ohata et al*., 2018]. Ny-Ålesund observation was conducted in an atmospheric monitoring station built at Mt. Zeppelin (474 m above sea level). The site is representative of the European Arctic background and can be influenced by pollutants transported from Europe and Russia [*Beine et al*., 1996, *Ström et al*., 2003]. The Polar Airborne Measurements and Arctic Regional Climate Model Simulation Project (PAMARCMiP) 2018 was conducted in spring 2018. PAMARCMiP consisted of a series of flights conducted over the North Polar and Northern Pacific regions, covering a vertical range up to approximately 5 km (Figure 4-1, Table 4A-1).

**Table4-1.** Summary of observations

| | Location | Latitude | Longitude | Altitude (m) | Term |
|---|---|---|---|---|---|
| A-FORCE 2009[a*] (dry-PBL) | Yellow Sea and East China Sea | 27.9°N–36.6°N | 124.4°E–137.4°E | 360–1930 | Mar. – Apr. 2009 |
| A-FORCE 2013 W[a*] (dry-PBL) | | 28.0°N–36.4°N | 124.4°E–130.3°E | 220–1980 | Feb. – Mar. 2013 |
| Hedo[b*] | Okinawa Island | 26.9°N | 128.3°E | 60 | Mar. 2016 |
| Fukue[b*] | Fukue Island | 32.8°N | 128.7°E | - | Apr. 2019 |
| Tokyo[b] | Hongo, Tokyo | 35.7°N | 139.7°E | 20 | Feb. 2014<br>Aug. – Sep. 2014 |
| Chiba[b*] | Chiba | 35.6°N | 140.1°E | 30 | Sep. 2016 |
| Ny-Ålesund[b] | Mt. Zeppelin, Svalbard | 78.9°N | 11.9°E | 474 | Mar. 2017 |
| PAMARCMiP 2018[a] | Greenland and Arctic ocean | 78.3°N–84.6°N | 24.0°W–20.0°E | 190–5200 | Mar. – Apr. 2018 |

[a]Aircraft measurement

[b]Ground measurement

[*]CO data available

For A-FORCE 2009 and 2013 datasets, I selected air masses that passed through the planetary boundary layer over the eastern China and were directly transported to the sampling point on the flight track below 2 km altitude without experiencing wet removal of aerosols (dry PBL air; *Kondo et al.* 2016, *Moteki et al.* 2017). For Fukue and Hedo datasets, I excluded the data when precipitation at the observation sites was observed in the 2 hr before or after a given time, as discussed for Hedo observation in Chapter 3. For Chiba observation, I excluded the data when the southerly wind was dominant in order to exclude the emission of steel plants 3.9 km southwest from the observation site [*Ohata et al.* 2018]. For the Tokyo dataset, the measurements were conducted in winter (Feb. 2014) and summer (Aug. – Sep. 2014). However, the sampling inlet tubes used in summer measurement were so long that only $FeO_x$ aerosols with $D_m < 740$ nm were measured; the majority of large particles ($D_m > 740$ nm) were dropped onto the wall on the tubes mainly due to gravitational settling. For this reason, I omit the Tokyo data in summer in the discussion until Section 5.1, at which point the emission sources of anthropogenic $FeO_x$ aerosols are discussed.

## 4.3 Results and discussion

### 4.3.1 Single-particle quantities

First of all, I show the observation results related to the microphysical properties for individual particles. The observed $FeO_x$ and BC aerosols were classified based on the $S_{i(b)}(t_{peak})$ value and color ratio. Figure 4-1 shows a scatter plot of the $FeO_x$ aerosols discriminated from BC. Although the color ratio is sensitive to the measurement conditions of the SP2 (especially the laser power), the ripple feature of $S_{i(b)}(t_{peak})$-vs-color ratio relationship resembles to the theoretical curve was noticeable in five out of the eight field-campaign-datasets (Figure 2a, b, c, d, and g). This $S_{i(b)}(t_{peak})$-vs-color ratio feature could be useful information, supporting the use of an extrapolated fitting curve for determining the $D_m$ values for large $FeO_x$ particles with mass > 1000 fg (Section 2.5.4).

Figure 4-2 shows the incandescence onset position $t_{oi}$ for observed $FeO_x$ aerosols (a-h) and standard magnetite and hematite particles as well as Taklamakan desert mineral dust particles (i). The distributions are similar among all observation data, resembling most closely that of laboratory magnetite, less so that of laboratory magnetite and hematite (Figure 4-2i). Although the contents of the observed aerosols are not identified in this study, their distribution differs from those of laboratory hematite and mineral dust $FeO_x$ particles (Figure 4-2i). In this

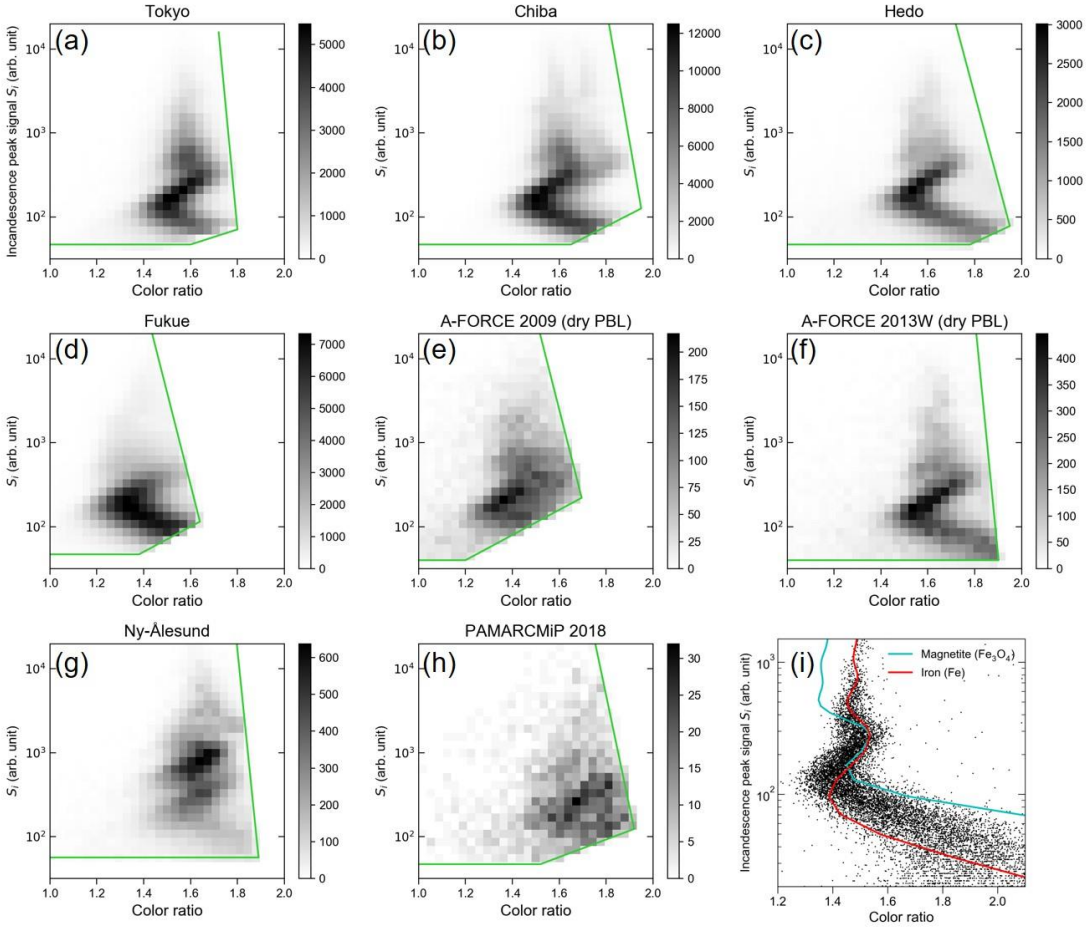


**Figure 4-1.** (a-h) Scatter plot of peak signal of incandescence in blue band ($S_{i(b)}(t_{peak})$) and color ratio for $FeO_x$ aerosols discriminated from BC. Gray shade represents the density of the distribution of $FeO_x$ aerosols. Thresholds used for classifying $FeO_x$ and BC are represented as green polygon boundaries. (i) Scatter plot for standard magnetite particles and theoretically calculated curves for spherical magnetite and iron particles. The details of the theoretical curves are described in Section 2.5.

study, I quantify the size of individual $FeO_x$ aerosol particles using a fitting curve for magnetite.

I further investigate the sources of measured $FeO_x$ aerosols focusing on the scattering cross section at the onset timing of incandescence $C_s(t_{oi})$ (Figure 4-3). Only small $FeO_x$

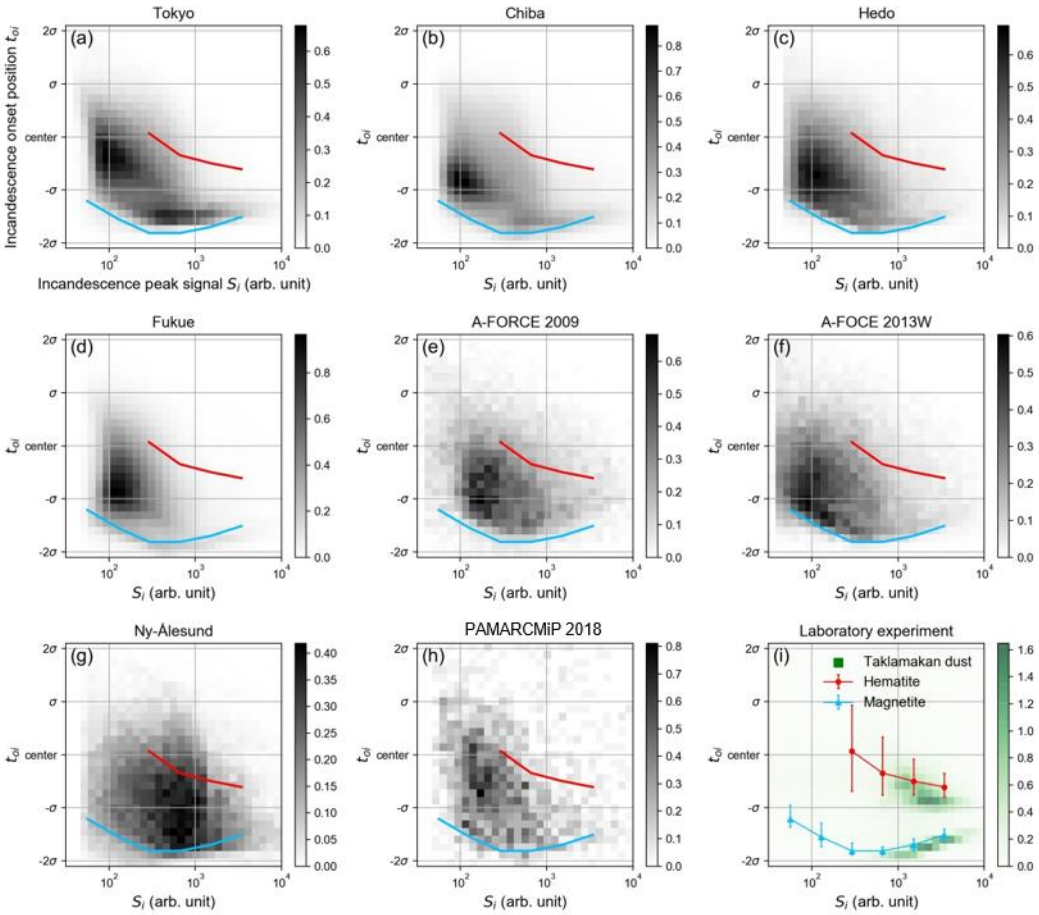


**Figure 4-2.** Scatter plots of the incandescence onset position $t_{oi}$ and the peak incandescence signal in the blue band ($S_i$) for observed $FeO_x$ particles in the eight campaign datasets (a–h) and for Taklamakan desert dust samples (i). $FeO_x$ data from the datasets are shown as black shading. Values of $t_{oi}$ are scaled by standard deviation of the Gaussian laser beam; negative positions represent particles that began to incandesce before reaching the center of the laser beam. The scatter plot in (i) shows data from Taklamakan desert dust samples as green shading. Color lines represents median values for standard magnetite (blue) and hematite (red) particles with error bars spanning the 10th to 90th percentiles; these color lines are overlaid in (a–h) for reference.

particles ($D_m$ < 340 nm) are shown. In all observations, the majority of $FeO_x$ aerosols have unsaturated $C_s(t_{oi})$ values (Figure 4-3a-h), in contrast to mineral dust particles (Figure 4-3i), which have saturated $C_s(t_{oi})$ values due to aluminosilicate components. Figure 4-4 shows the dust-like $FeO_x$ number fraction. In this study, dust-like $FeO_x$ is defined as $FeO_x$ particles with $D_m$ = 170–270 nm and $C_s(t_{oi}) < 1.4\times10^{-14}$ $m^2$ (red lines in Figure 4-3). The dust-like $FeO_x$ fraction constitutes less than ~ 15% of all observations.

All of these results indicate that, the majority of the measured $FeO_x$ aerosols are of anthropogenic origins; not only those in East Asian continental outflow and urban environments, but also those in the Arctic region.

In addition to the SP2 measurement, electron microscope analysis (conducted by Dr. Adachi) shows that measured Fe aerosols collected during $FeO_x$ observation are predominantly anthropogenic aggregated iron oxide particles or fly ash particles in A-FORCE 2013, Hedo, Tokyo, and Chiba observations (Figures 3-5, 4-5, 4-6). Table 4-2 summarizes the numbers of anthropogenic iron oxide, Fe-bearing iron fly ash, and Fe-bearing mineral dust particles counted by the electron microscope, showing that most iron aerosols were of anthropogenic sources. Anthropogenic $FeO_x$ aerosols were found in field measurements such as urban environments [*Sanderson et al.,* 2016] and over the East China Sea [*Li et al*., 2017]. However, to my knowledge, the present study is the first to find anthropogenic $FeO_x$ aerosols in the Arctic region.

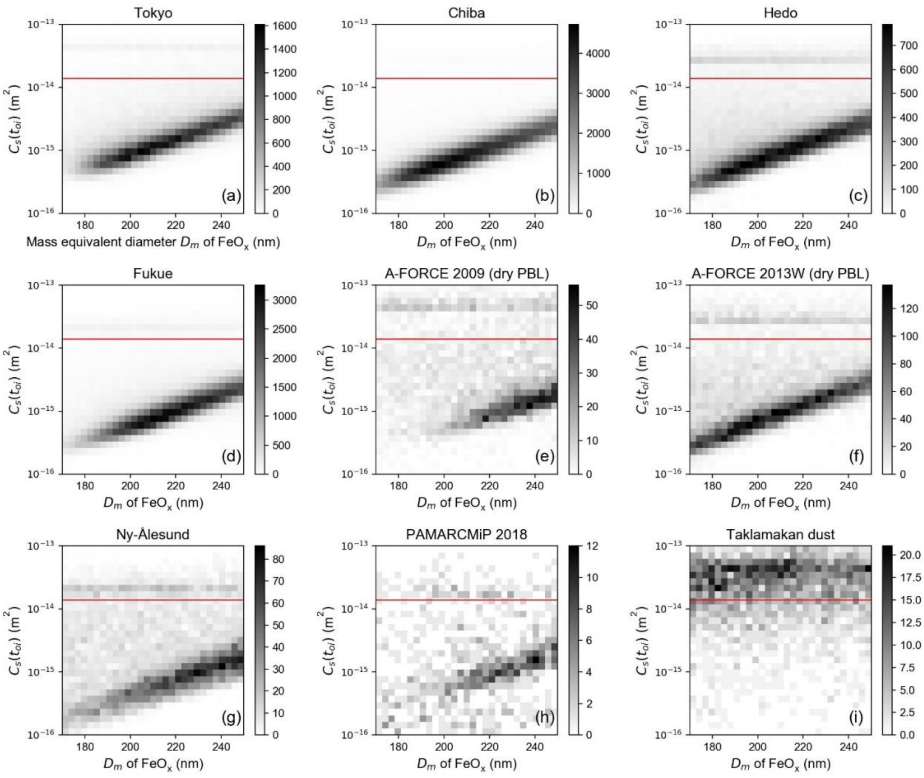


**Figure 4-3.** Scatter plots of the scattering cross section at the onset of incandescence $C_s(t_{oi})$ and mass-equivalent diameter $D_m$ for ambient $FeO_x$ aerosols. The red lines represent the saturation threshold of $C_s(t_{oi})$ ($1.4 \times 10^{-14}$ m$^2$) used in this study.

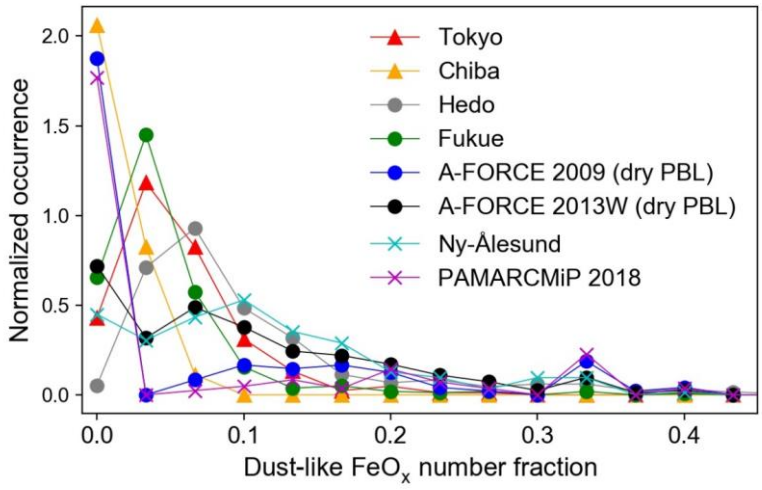


**Figure 4-4.** Histogram of the number fraction of dust-like $FeO_x$ particles to all $FeO_x$ particles with $D_m$ = 170–270 nm as measured by the SP2.

**Table 4-2.** Number of particles determined via STEM-EDS analysis for the samples collected in Tokyo, Chiba, and A-FORCE 2013.

| Date | Sampling time | All measured particles | Aggregated $FeO_x$ nanoparticles | Fe-bearing fly ash | Fe-bearing mineral dust | Number fraction of mineral dust in these three types of Fe-bearing particles |
|---|---|---|---|---|---|---|
| **Tokyo** | | | | | | |
| 7 Aug. 2014 | 12:00–12:03 | 394 | 39 | 24 | 0 | 0 |
| 7 Aug. 2014 | 16:48–16:51 | 241 | 44 | 6 | 1 | 0.020 |
| 8 Aug. 2014 | 15:36–15:39 | 402 | 32 | 6 | 13 | 0.25 |
| total | | 1037 | 115 | 36 | 14 | 0.085 |
| **Chiba** | | | | | | |
| Sep. 6 2016 | 23:35–23:40 | 455 | 82 | 8 | 0 | 0 |
| Sep. 15 2016 | 0:00–0:05 | 219 | 21 | 0 | 0 | 0 |
| Sep. 23 2016 | 22:30–22:35 | 334 | 143 | 18 | 0 | 0 |
| Sep.24 2016 | 4:30–4:35 | 457 | 12 | 3 | 0 | 0 |
| total | | 1465 | 258 | 29 | 0 | 0 |
| **A-FORCE 2013W** | | | | | | |
| Mar. 4 2013 | 14:35–14:47 | 278 | 20 | 6 | 1 | 0.038 |
| Mar. 7 2013 | 11:53–12:05 | 344 | 4 | 4 | 0 | 0 |
| Mar. 7 2013 | 12:53–13:05 | 403 | 11 | 2 | 0 | 0 |
| Mar. 8 2013 | 11:17–11:29 | 435 | 1 | 9 | 1 | 0.10 |
| | | 1460 | 36 | 21 | 2 | 0.035 |

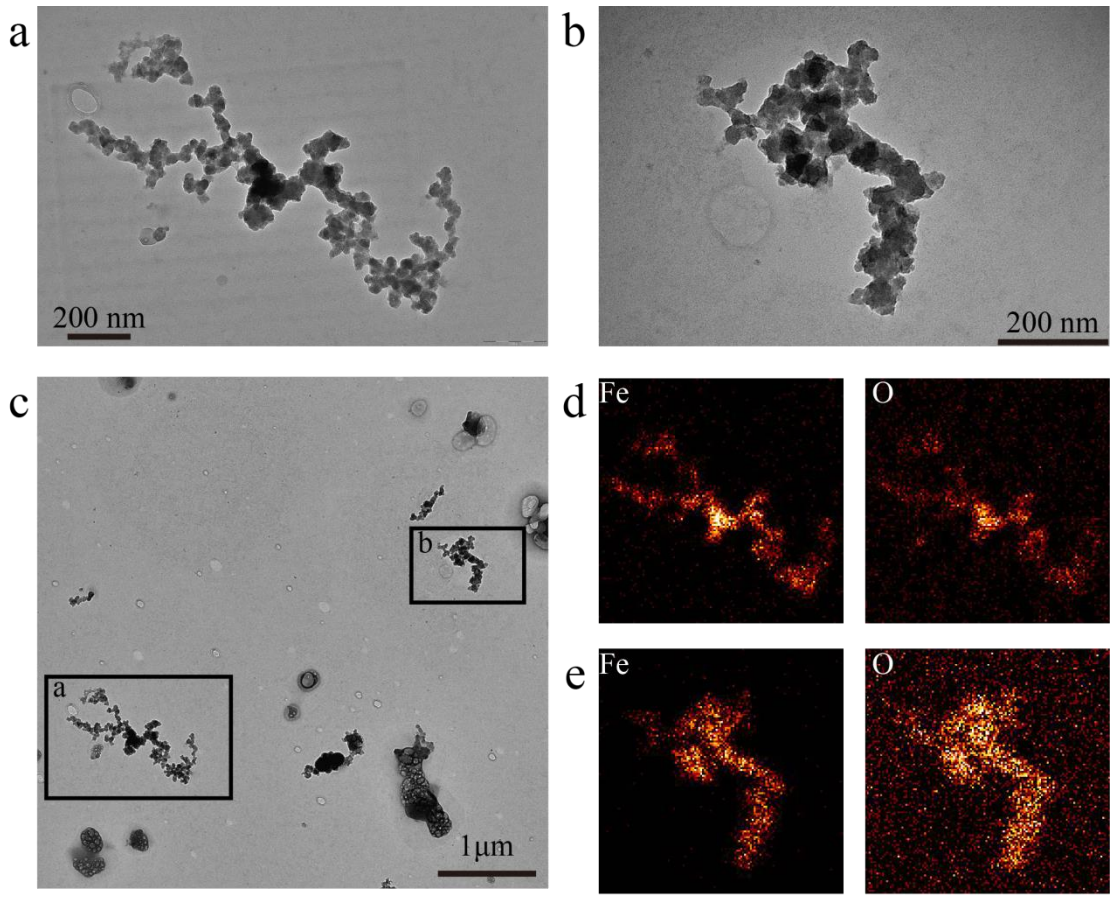


**Figure 4-5.** TEM images and element distributions of aggregated $FeO_x$ nanoparticles found in the A-FORCE 2013W campaign. The sample was collected by an aerosol-impactor sampler onboard the aircraft from 14:35 to 14:47 on March 4, 2013 (local time). As shown in panel (c), the particles magnified in panels (a) and (b) were collected on the same substrate with the inter-particle distance of ~4 μm. The elemental distributions of Fe and O for particles (a) and (b) are shown in panels (d) and (e), respectively.

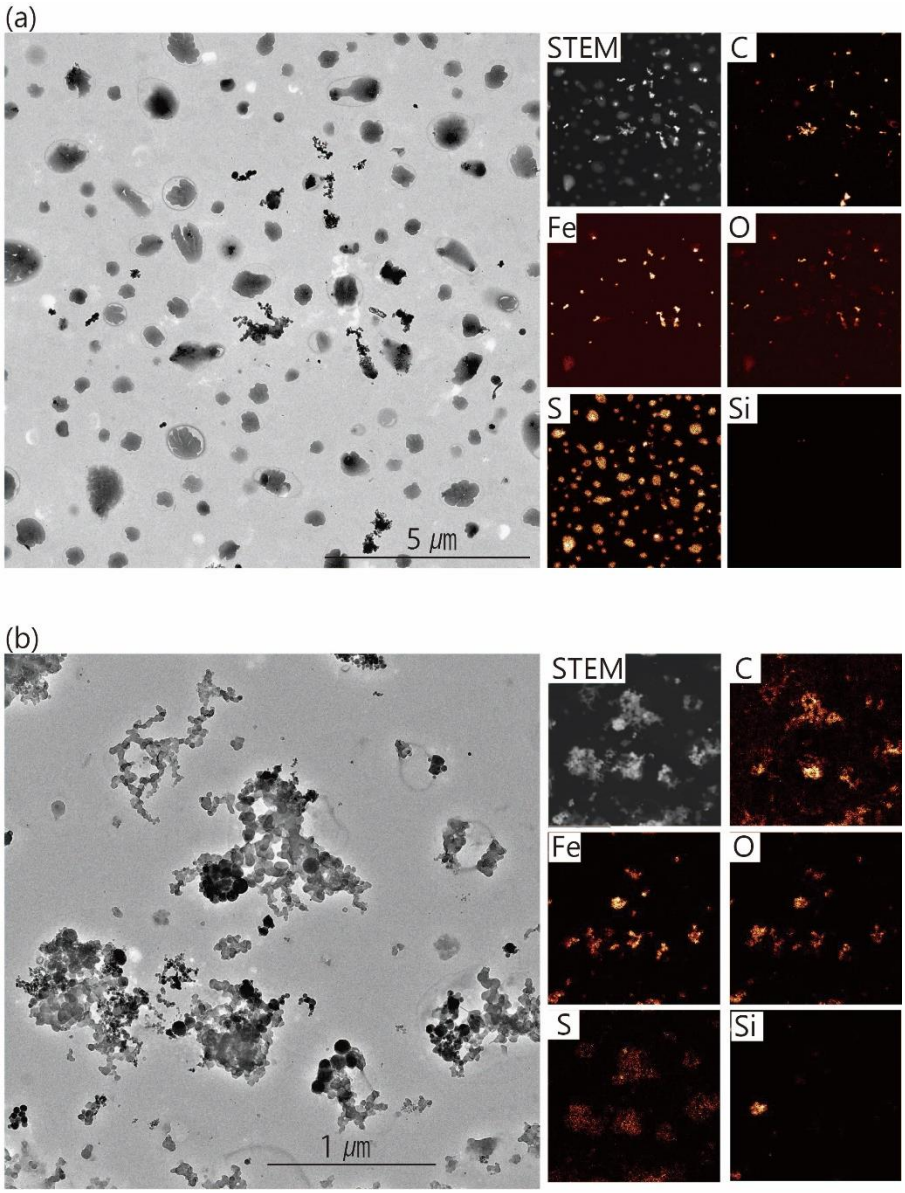


**Figure 4-6.** TEM images of aggregated $FeO_x$ and BC particles found in (a) Tokyo (summer) and (b) Chiba. The sample in Tokyo was collected from 12:00 to 12:03 on 7 August 2014. The sample in Chiba was collected from 22:30 to 22:35 on 23 September 2016. The STEM images and elemental distributions of the particles (C, Fe, O, S, and Si) are shown to the right of each TEM image.

### 4.3.2 Size distribution

Figure 4-7 shows the normalized size distribution of $FeO_x$ aerosols. The d$M$/dlog$D_m$ values for $FeO_x$ are modified by transmission efficiency considering particle loss in the sampling line from the ambient air to the SP2 (Equation 2-7A). Figure 4A-1 shows the calculated transmission efficiency using Equation 2-7A and geometrics of sampling inlet, summarized in Table 4A-2. I did not modify the d$M$/dlog$D_m$ of BC because the transmission efficiency of BC is approximately unity.

Both the normalized d$M$/dlog$D_m$ and d$N$/dlog$D_m$ values for $FeO_x$ aerosols are remarkably similar among the observations except for PAMARCMiP d$M$/dlog$D_m$ data. This finding is surprising when different degrees of removal processes that air could have experienced are considered. The observed similarity implies that emission sources of $FeO_x$ aerosols are mostly common, resulting in similar size distributions.

A reason for the difference in the shape of d$M$/dlog$D_m$ data obtained during PAMARCMiP measurement from others is not clear. The shape of PAMARCMiP size distribution may suggest a higher degree of removals because both dry and wet removal

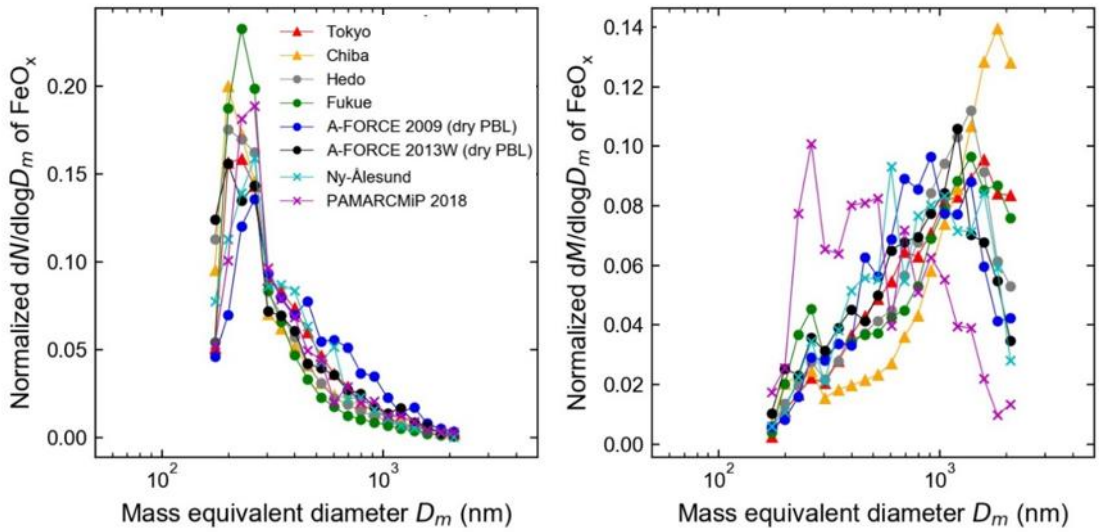


**Figure 4-7.** Mean normalized d$N$/dlog$D_m$ (left) and d$M$/dlog$D_m$ (right) of $FeO_x$ aerosols. The time resolutions for each observational data set are same as those described in Table 4-3.

processes are generally more efficient for larger particles in this size range. In the northern polar region, there is a transport barrier known as the "polar dome," resulting from isentropic sloping. Transport time of pollutants from potential sources (in lower latitudes) to the polar dome is long, $t$ > ~10 days [*Willis et al.,* 2019]. Thus, large $FeO_x$ aerosols measured in PAMARCMiP could have been removed by dry deposition or wet removal during transport.

### 4.3.3 Number and mass concentrations

Table 4-3 summarizes the concentrations of BC and $FeO_x$ aerosols and the CO mixing ratio. Figure 4-8 shows box-whisker plots of mass concentrations of BC and $FeO_x$ aerosols and their mass concentration ratio. The time resolutions are different between observations in order to reduce statistical errors. Notably, the mass concentrations of BC and $FeO_x$ aerosols were in the same order between datasets obtained in the urban environment (Tokyo) and East Asian continental outflow (A-FORCE 2009 and 2013, Hedo, and Fukue), suggesting significant emission sources on the Asian continent. In the Arctic region, the concentrations are ~1 order lower than these values. However, the mass concentration ratios of $FeO_x$ to BC are not very different among the datasets: they are ~20%–50% in all observations including the Arctic region. This result implies that anthropogenic $FeO_x$ aerosols in the northern hemisphere atmosphere exist at a mass ~20%–50% that of BC.

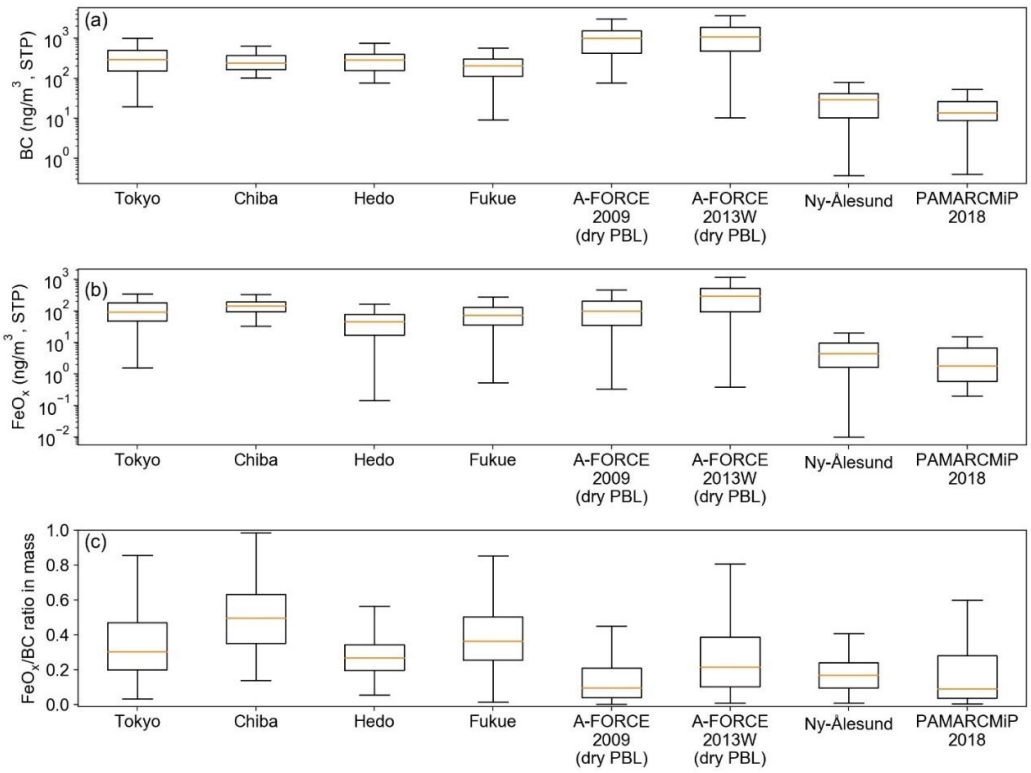


**Figure 4-8.** Box-whisker plots of mass concentrations of BC and $FeO_x$ aerosols and their mass concentration ratio. Each box-whisker displays minimum, first quartile, median (orange line), third quartile, and maximum value.

**Table 4-3.** Mean values of BC and $FeO_x$ abundances.

| | Time resolution | CO (ppbv) | BC (ng/m$^3$) | BC (#/cm$^3$) | $FeO_x$ (ng/m$^3$) | $FeO_x$ (#/cm$^3$) | $FeO_x$ (ng/m$^3$)/ BC (ng/m$^3$) |
|---|---|---|---|---|---|---|---|
| A-FORCE 2009 (dry PBL) | 1 min | 268 | 990 | 112.7 | 154 | 0.41 | 17.3% |
| A-FORCE 2013W (dry PBL) | 1 min | 299 | 1025 | 207.9 | 377 | 1.04 | 36.1% |
| Hedo | 1 hour | 212 | 284 | 73.2 | 78.5 | 0.25 | 26.1% |
| Fukue | 1 hour | 171 | 242 | 65.9 | 93.9 | 0.39 | 39.8% |
| Tokyo | 1 hour | - | 562 | 95.2 | 188 | 0.43 | 36.5% |
| Chiba | 1 hour | 232 | 291 | 94.3 | 177 | 0.41 | 54.1% |
| Ny-Ålesund | 3 hour | - | 28 | 7.1 | 6.43 | 0.015 | 18.1% |
| PAMARCMiP 2018 | 10 min | - | 21 | 3.6 | 5.15 | 0.010 | 28.4% |

### 4.3.4 Correlation

Figure 4-9 shows the scatter plot of BC and $FeO_x$ mass concentration and CO mixing ratio. The correlation slope and $R^2$ values are summarized in Table 4-4. Scatter plots of mass concentration of $FeO_x$ are shown only for ground observations. For aircraft measurements (A-FORCE 2009 and 2013 and PAMARCMiP), measurement times were not long enough to provide data for making the correlation. BC concentration is well correlated with CO mixing ratio (Figure 4-9a), reflecting that their emission sources, i.e., combustion sources, are spatially similar. In addition, $FeO_x$ concentration is also well correlated with BC and with CO (Figure 7b-d). In particular, number concentrations of $FeO_x$ and BC are well correlated for all

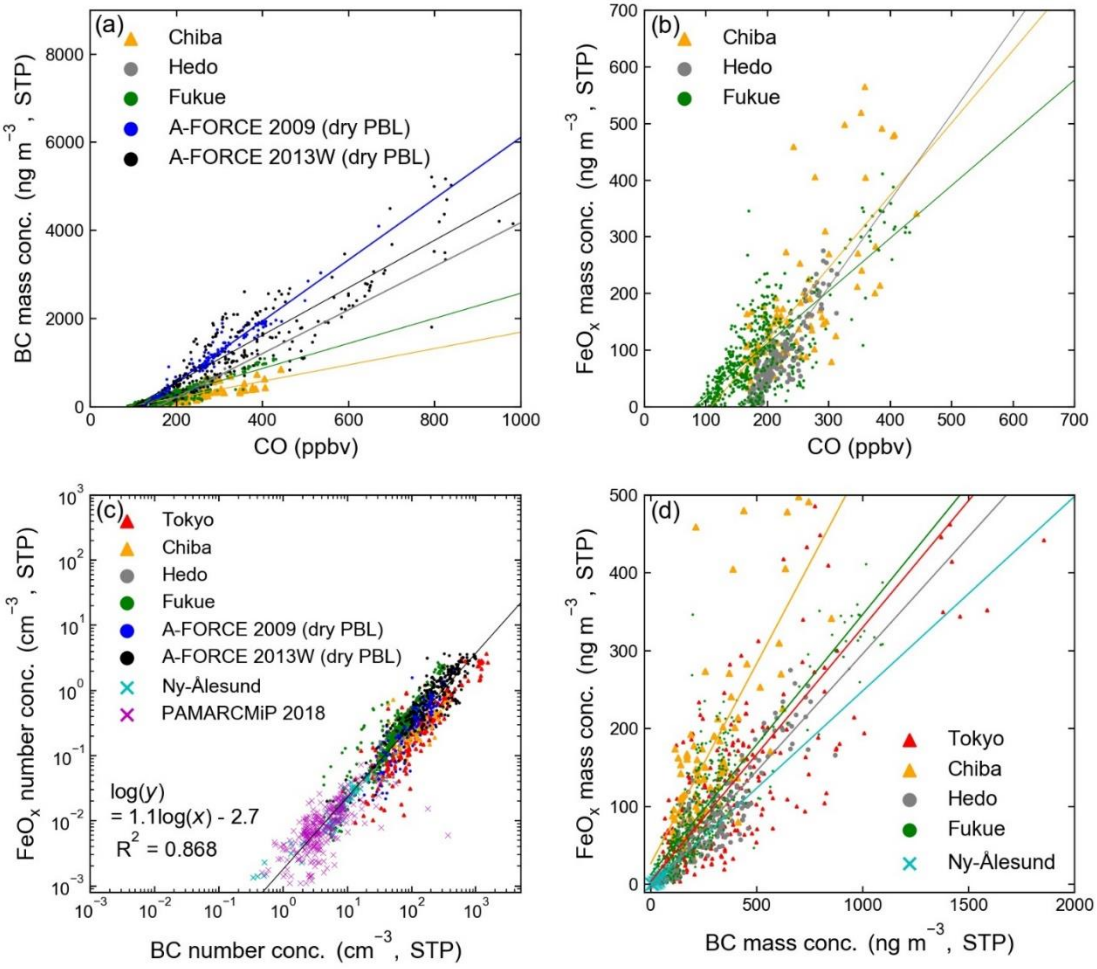


**Figure 4-9.** Scatter plots of BC and $FeO_x$ concentrations and CO mixing ratio. Time resolutions are the same as those described in Table 4-3. Fitting lines are also shown in the figure using 1-D linear regression. The fitting slopes and $R^2$ values are denoted in Table 4-4.

observations. The possible sources of pollutants measured in East Asian continental outflow are in East Asia, especially China; those measured in urban environments are in local Tokyo and Chiba sources. For observations in the Arctic, pollutants from lower latitudes such as Europe, Russia, North America, and Asia are potential sources for the measured pollutants [*Barrie et al.* 1981]. Thus, the good correlations of $FeO_x$ aerosols imply that emission sources of anthropogenic $FeO_x$ aerosols are similar to those of BC and CO in the northern hemisphere. Although it is difficult to evaluate the sources of the measured $FeO_x$ aerosols based on the correlation alone, the sources in the urban environments will be discussed based on a detailed analysis of the observed data for urban $FeO_x$ aerosols in Section 5.2.

**Table 4-4.** Summary of correlation slope and $R^2$ for $FeO_x$, BC, and CO

| | BC ($ng/m^3$) / CO (ppbv) | | BC ($ng/m^3$) / $FeO_x$ ($ng/m^3$) | | $FeO_x$ ($ng/m^3$) / CO (ppbv) | |
|---|---|---|---|---|---|---|
| | slope | $R^2$ | slope | $R^2$ | Slope | $R^2$ |
| A-FORCE 2009 (dry PBL) | 6.94 | 0.95 | - | - | - | - |
| A-FORCE 2013 W (dry PBL) | 5.39 | 0.83 | - | - | - | - |
| Hedo | 4.94 | 0.93 | 0.30 | 0.77 | 1.52 | 0.76 |
| Fukue | 2.84 | 0.82 | 0.33 | 0.75 | 0.93 | 0.59 |
| Tokyo | - | - | 0.33 | 0.76 | - | - |
| Chiba | 1.85 | 0.58 | 0.51 | 0.50 | 1.28 | 0.52 |
| Ny-Ålesund | - | - | 0.25 | 0.74 | - | - |

### 4.3.5 Mixing state

Figure 4-10 shows a scatter plot of hourly median values of $\log(C_s(t_{be})/C_s(t_{oi}))$, the proxy for the thickness of particle coatings, for BC vs. $FeO_x$ aerosols (Section 2.8). Only $FeO_x$ particles of diameter 195 nm < $D_m$ < 210 nm and of solid angle $C_s(t_{oi})$ < ~2 × $10^{-14}$ $m^2$ (bounded by the blue lines in Figure 3-4) were considered. Selected size ranges for BC particles are equivalent to those of $FeO_x$.

A clear positive correlation between $FeO_x$ and BC aerosols can be seen even with all observational data combined ($R^2$ = 0.70). This correlation indicates that atmospheric aging processes contribute to the coatings of both $FeO_x$ and BC aerosol particles. TEM analyses also indicate that aged $FeO_x$ aerosol particles are coated with sulfates or organics (Figures 3-5, 4-5, 4-6). In particular, coating by sulfate promotes acidic dissolution of iron (*Li et al.*, 2017). Thus, atmospheric aging could be a key factor in evaluating the supply of bioavailable iron to the

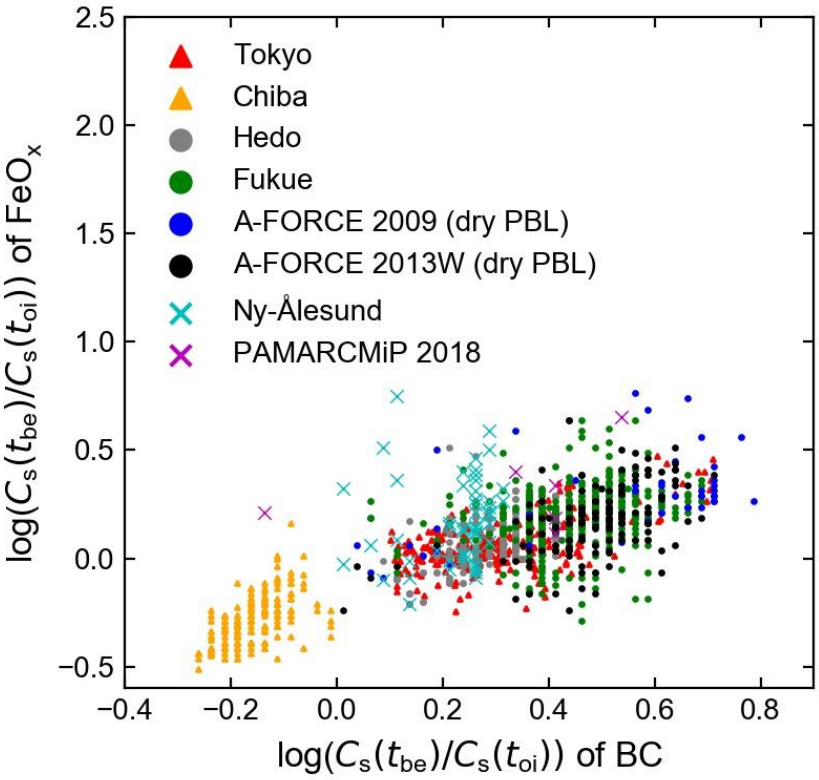


**Figure 4-10.** Scatter plot of the hourly median values of $\log(C_s(t_{be})/C_s(t_{oi}))$ for BC and $FeO_x$ aerosols.

surface ocean.

## 4.4 Summary

$FeO_x$ aerosols in East Asian continental outflow, urban environments, and the Arctic region were measured and analyzed using the developed LII technique. Size distribution, concentration, and mixing state of such $FeO_x$ aerosols were analyzed. Based on the single-particle quantities measured by the SP2 (color ratio, incandescence onset position, and scattering cross section), a majority of the measured $FeO_x$ aerosols are anthropogenic particles.

The shapes of size distributions, especially number size distributions, are similar among all observations, indicating that the measured $FeO_x$ aerosols are emitted from common sources. The mass concentrations of $FeO_x$ aerosols in East Asian continental outflow and urban environments are of the same order, while those in the Arctic region are 1–2 orders of magnitude lower. However, the $FeO_x$/BC mass concentration ratios are similar among all observations, implying that anthropogenic iron $FeO_x$ aerosols in the northern hemisphere atmosphere exist at a mass of ~20%–50% that of BC. $FeO_x$, BC, and CO were well correlated with each other in all the regions observed. These results indicate that $FeO_x$ BC and CO were emitted in nearly the same areas with similar emission ratios.

The measured scattering cross section ratio $\log(C_s(t_{be})/C_s(t_{oi}))$ indicates that $FeO_x$ aerosols experience atmospheric aging processes, with coating thickness gradually increasing as well as BC. These facts seem obvious, but the developed LII technique provides observational confirmation of this process. Further experiments are needed in order to derive the coating thickness of $FeO_x$ aerosols from the measured $\log(C_s(t_{be})/C_s(t_{oi}))$ values.

## Appendix 4-1: Dates and locations of aircraft flights during PAMARCMiP campaign

**Table 4A-1.** Dates and Locations of Aircraft Flights During PAMARCMiP Campaign

| Flight No. | Date 2018 | Takeoff (UT) | Landing (UT) | Duration of Flight (min) |
|---|---|---|---|---|
| 1 | 23 Mar. | 11:53 | 12:47 | 54 |
| 2 | 25 Mar. | 14:12 | 17:55 | 223 |
| 3 | 26 Mar. | 11:53 | 15:41 | 228 |
| 4 | 26 Mar. | 16:49 | 18:06 | 76 |
| 5 | 27 Mar. | 13:00 | 17:04 | 244 |
| 6 | 28 Mar. | 11:00 | 13:05 | 125 |
| 7 | 28 Mar. | 14:58 | 17:27 | 209 |
| 8 | 30 Mar. | 07:42 | 13:07 | 325 |
| 9 | 31 Mar. | 11:30 | 17:39 | 369 |
| 10 | 2 Apr. | 10:07 | 14:14 | 247 |
| 11 | 2 Apr. | 15:07 | 16:29 | 82 |
| 12 | 3. Apr. | 07:53 | 11:54 | 241 |
| 13 | 3. Apr. | 12:54 | 16:44 | 230 |
| 14 | 4. Apr. | 07:51 | 11:50 | 239 |

## Appendix 4-2: Geometry and flow rate of the individual components of the aerosol sampling system

**Table 4A-2.** Geometry and flow rate of the individual components of the aerosol sampling system

| Component | Inner diameter (mm) | Geometry | Volumetric flow rate (L $min^{-1}$) |
|---|---|---|---|
| Inside the SP2 (common in all observations) | | | |
| 1/8” tube | 2.0 | 0.3 m length | 0.06 (Fukue 2019)<br>0.1 (the others) |
| 1/8” bend | 2.0 | 90° bend | 0.06 (Fukue 2019)<br>0.1 (the others) |
| SP2 aerosol jet | 2.0 (inlet)<br>0.5 (outlet) | Abrupt constriction | 0.06 (Fukue 2019)<br>0.1 (the others) |
| Outside the SP2 (A-FORCE 2009, 2013W) | | | |
| Shrouded solid diffuser inlet | 5.1 (tip) | See Methods section | 80 |
| 1” tube | 22 | 1.5 m length | 80 |
| 1” bend | 22 | 45° bend | 80 |
| 3/4” tube | 16 | 1.5 m length | 80 |
| 3/4” bend | 16 | 45° bend | 80 |
| 1/4” tube | 4.0 | 2.0-m length | 2 |
| 1/4” bend | 4.0 | 90° bend | 2 |
| Outside the SP2 (Tokyo 2014) | | | |
| 1/4” tube | 4.0 | 2.0-m length | 0.5 |
| 1/4” bend | 4.0 | 90° bend | 0.5 |
| Outside the SP2 (Hedo 2016) | | | |

| | | | |
|---|---|---|---|
| 1/4” tube | 4.0 | 0.67 m length | 1.0 |
| 1/4” tube | 4.0 | 0.88 m length | 0.4 |
| 1/4” tube | 4.0 | 0.75 m length | 0.3 |
| Outside the SP2 (Chiba 2016) | | | |
| 1/4” tube | 4.0 | 1.0 m length | 2.0 |
| 1/4” bend | 4.0 | 90° bend | 2.0 |
| Outside the SP2 (Bremen 2018 and PAMARCMiP 2018) | | | |
| 1” tube | 16 | 0.6 m length | 20 |
| 3/4” tube | 12 | 0.3 m length | 1.6 |
| 3/4” bend | 12 | 45° bend | 1.6 |
| 1/4” tube | 4 | 1.1 m length | 1.6 |
| 1/4” tube | 4 | 0.6 m length | 1.6 |
| 1/4” tube | 4 | 0.8 m length | 1.6 |
| Outside the SP2 (Fukue 2019) | | | |
| 1/4” tube | 4 | 3.5 m length | 2.0 |
| 1/4” tube | 4 | 1.3 m length | 2.0 |

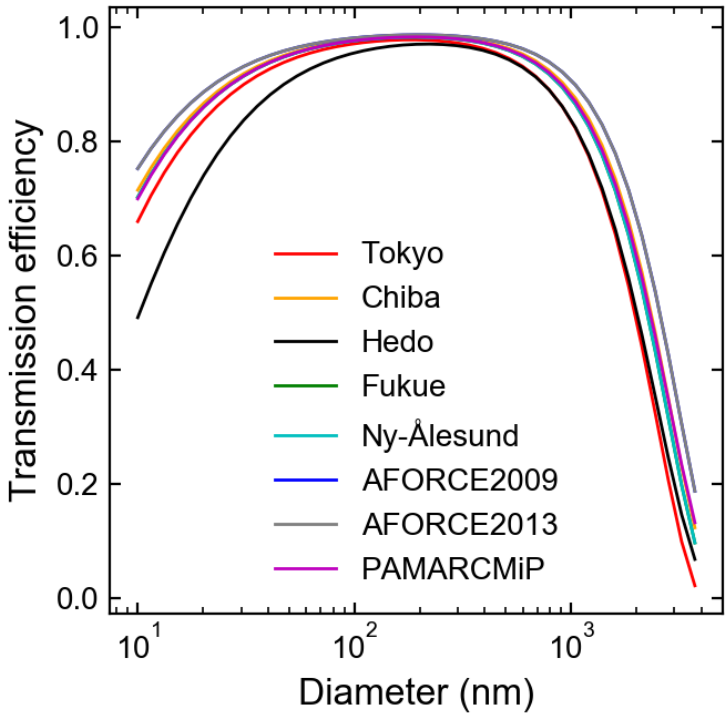


**Figure 4A-1.** Theoretical transmission efficiency of $FeO_x$ aerosols calculated by Equation 2-7A. Particles density and shape factors are 5.17 g $cm^{-3}$ and 1.5, respectively

## References


Baker, A. R. & Jickells, T. D. (2006) Mineral particle size as a control on aerosol iron solubility. *Geophys. Res. Lett. 33*, L17608.

Barrie, L. A., Hoff, R. M., & Daggupaty, S. M. (1981). The influence of mid-latitudinal pollution sources on haze in the Canadian Arctic. *Atmospheric Environment (1967)*, *15*(8), 1407-1419.

Beine, H. J., Engardt, M., Jaffe, D. A., Hov, Ø., Holme, K., & Stordal, F. (1996). Measurements of NOx and aerosol particles at the NY-Ålesund Zeppelin mountain station on Svalbard: Influence of regional and local pollution sources. *Atmospheric Environment*, *30*(7), 1067-1079.

Chen, H., Laskin, A., Baltrusaitis, J., Gorski, C. A., Scherer, M. M., & Grassian, V. H. (2012). Coal fly ash as a source of iron in atmospheric dust. *Environmental science & technology*, *46*(4), 2112-2120.

Chuang, P. Y., Duvall, R. M., Shafer, M. M. & Schauer J. J. (2005).The origin of water soluble particulate iron in the Asian atmospheric outflow. *Geophys. Res. Lett. 32*, L07813.

Guieu, C., Bonnet, S., Wagener, T. & Loÿe-Pilot, M.-D. (2005). Biomass burning as a source of dissolved iron to the open ocean? *Geophys. Res. Lett. 32*, L19608.

Ito, A. (2013). Global modeling study of potentially bioavailable iron input from shipboard aerosol sources to the ocean, *Global Biogeochemical Cycles*, *27*(1), 1-10, doi:10.1029/2012GB004378

Ito, A., G. Lin, & J. Penner (2018), Radiative forcing by light-absorbing aerosols of pyrogenetic iron oxides, *Scientific Reports*, *8*(1), 7347, doi:10.1038/s41598-018-25756-3.

Jacobson, M. Z. (2000). A physically-based treatment of elemental carbon optics: Implications for global direct forcing of aerosols. *Geophysical Research Letters*, *27*(2), 217-220.

Kondo, Y., Moteki, N., Oshima, N., Ohata, S., Koike, M., Shibano, Y., ... & Kita, K. (2016). Effects of wet deposition on the abundance and size distribution of black carbon in East

Asia. *Journal of Geophysical Research: Atmospheres*, *121*(9), 4691-4712.

Li, W., Xu, L., Liu, X., Zhang, J., Lin, Y., Yao, X., Gao, H., Zhang, D., et al. (2017). Air pollution–aerosol interactions produce more bioavailable iron for ocean ecosystems, *Science Advances*, *3*(3), e1601749, doi:10.1126/sciadv.1601749

Luo, C., Mahowald, N., Bond, T., Chuang, P., Artaxo, P., Siefert, R., Chen, Y., & Schauer, J. (2008). Combustion iron distribution and deposition, *Global Biogeochemical Cycles*, *22*(1), doi:10.1029/2007GB002964

Magiera, T., Jabłońska, M., Strzyszcz, Z., & Rachwal, M. (2011). Morphological and mineralogical forms of technogenic magnetic particles in industrial dusts. *Atmospheric Environment*, *45*(25), 4281-4290.

Moteki, N., Adachi, K., Ohata, S., Yoshida, A., Harigaya, T., Koike, M., & Kondo, Y. (2017). Anthropogenic iron oxide aerosols enhance atmospheric heating, *Nature Communications*, *8*, 15329, doi:10.1038/ncomms15329

Ohata, S., Yoshida, A., Moteki, N., Adachi, K., Takahashi, Y., Kurisu, M., & Koike, M. (2018). Abundance of light-absorbing anthropogenic iron oxide aerosols in the urban atmosphere and their emission sources. *Journal of Geophysical Research: Atmospheres*, *123*(15), 8115-8134.

Ohata, S., Kondo, Y., Moteki, N., Mori, T., Yoshida, A., Sinha, P. R., & Koike, M. (2019). Accuracy of black carbon measurements by a filter-based absorption photometer with a heated inlet. *Aerosol Science and Technology*, *53*(9), 1079-1091.

Oshima, N., Kondo, Y., Moteki, N., Takegawa, N., Koike, M., Kita, K., Matsui, H., Kajino, M., et al. (2012). Wet removal of black carbon in Asian outflow: Aerosol Radiative Forcing in East Asia (A-FORCE) aircraft campaign, *Journal of Geophysical Research: Atmospheres*, *117*(D3), doi:10.1029/2011JD016552

Samset, B. H. Myhre, G., Herber, A., Kondo, Y., Li, S. M., Moteki, N., ... & Bauer, S. E. (2014) Modelled black carbon radiative forcing and atmospheric lifetime in AeroCom Phase II

constrained by aircraft observations. *Atmos. Chem. Phys. 14,* 12465-12477.

Sanderson, P., Su, S. S., Chang, I. T. H., Saborit, J. M., Kepaptsoglou, D. M., Weber, R. J. M., & Harrison, R. (2016). Characterisation of iron-rich atmospheric submicrometre particles in the roadside environment, *Atmospheric Environment*, *140*, 167-175, doi:10.1016/j.atmosenv.2016.05.040

Sokolik, I. N., & Toon, O. B. (1999). Incorporation of mineralogical composition into models of the radiative properties of mineral aerosol from UV to IR wavelengths. *Journal of Geophysical Research*, *104*(D8), 9423-9444.

Ström, J., Umegård, J., Tørseth, K., Tunved, P., Hansson, H. C., Holmén, K., ... & König-Langlo, G. (2003). One year of particle size distribution and aerosol chemical composition measurements at the Zeppelin Station, Svalbard, March 2000–March 2001. *Physics and Chemistry of the Earth, Parts A/B/C*, *28*(28-32), 1181-1190.

Takami, A., Miyoshi, T., Shimono, A., & Hatakeyama, S. (2005). Chemical composition of fine aerosol measured by AMS at Fukue Island, Japan during APEX period. *Atmospheric Environment*, *39*(27), 4913-4924.

Wang, R., Balkanski, Y., Boucher, O., Bopp, L., Chappell, A., Ciais, P., Hauglustaine, D., Peñuelas, J., & Tao, S. (2015). Sources, transport and deposition of iron in the global atmosphere, *Atmospheric Chemistry and Physics*, *15*, 6247-6270, doi:10.5194/acp-15-6247-2015

Willeke, K., & Whitby, K. T. (1975). Atmospheric aerosols: size distribution interpretation. *Journal of the Air Pollution Control Association*, *25*(5), 529-534.

Willis, M. D., Bozem, H., Kunkel, D., Lee, A. K., Schulz, H., Burkart, J., ... & Abbatt, J. P. (2019). Aircraft-based measurements of High Arctic springtime aerosol show evidence for vertically varying sources, transport and composition. *Atmospheric Chemistry and Physics*, *19*(1), 57-76.

Zhang, X. L., Wu, G. J., Zhang, C. L., Xu, T. L., & Zhou, Q. Q. (2015). What's the real role of

iron-oxides in the optical properties of dust aerosols?, *Atmospheric Chemistry and Physics Discussion*,*15*(4), 5619–5662, doi:10.5194/acpd-15-5619-2015.

# 5 Discussion

In this chapter, I further discuss the abundances of anthropogenic $FeO_x$ aerosols based on the dataset used in Chapter 4. In Section 5.1, I show the detailed analysis of $FeO_x$ aerosols measured in Tokyo and Chiba and examine the emission sources of anthropogenic iron aerosols in urban environments. In section 5.2, I show the simulated result of anthropogenic iron aerosols using global model simulation calculated by Dr. Matsui (Nagoya University), where the measured data of $FeO_x$ in A-FORCE 2013W were used as a constraint for the simulation. Based on the simulated result, the radiative forcing of anthropogenic iron aerosols and iron deposition rate to the surface ocean will be discussed.

## 5.1 Emission sources of anthropogenic iron oxides in urban environments

$FeO_x$ measurements in Tokyo and Chiba are further examined in order to understand the possible sources of anthropogenic $FeO_x$ aerosols. The detail locations of these observation sites are shown in Figure 5-1. The observation site in Tokyo is located in the Tokyo Metropolitan Area and is approximately 10 km northwest of the Tokyo Bay coastline. The observation site

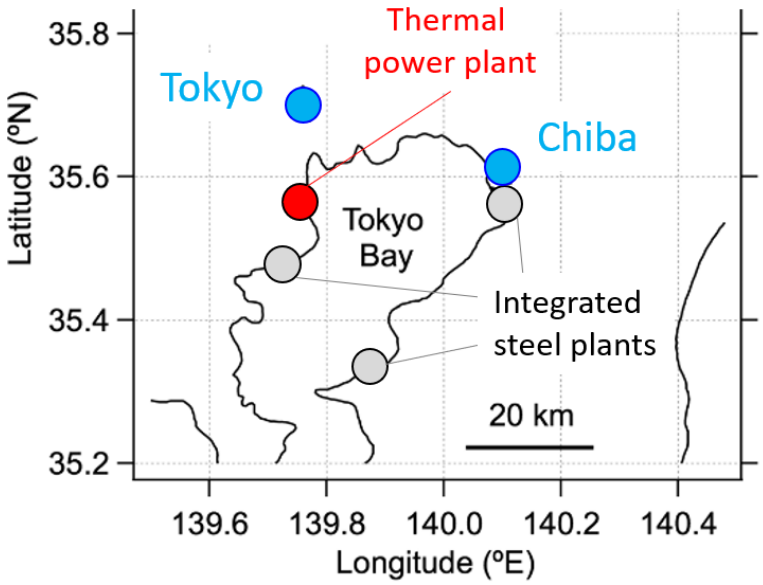


**Figure 5-1.** Location map of observation sites (Tokyo and Chiba), thermal power plant, and integrated steel plants.

for Chiba is a building of the Chiba City Hall center, approximately 30 m above ground level. In this region, there are integrated steel plants and a thermal power plant, both known emission sources of anthropogenic $FeO_x$ aerosols [*Flament et al.,* 2008*, Luo et al.,* 2008, *Wang et al.,* 2015]. The Chiba observation site is approximately 3.9 km northeast of an integrated steel plant that includes a blast furnace and coke oven plants. Such large steelworks operate at three locations along the Tokyo Bay coastline, as shown in Figure 5-1. In addition, thermal power plant burning coal is located ~10 km and ~30 km, respectively, from the Tokyo and Chiba observation sites.

As mentioned above, $FeO_x$ aerosols measured in summer can be quantified up to $D_m$ = 740 nm, but not beyond, due to particle loss in the long transport tubes. In this section I express the mass concentration of $FeO_x$ measured for Tokyo summer data as $M_{740}$ and for Tokyo summer and Chiba data as $M_{2100}$ for the sake of clarity. Figure 5-2 shows the dependencies of the $FeO_x$ and BC mass concentrations and the $FeO_x$/BC mass concentration ratio on the local wind direction. In Chiba, the average mass concentration of BC ($M_{BC}$) depended little on the wind direction, whereas the $M_{2100}$ values and $M_{2100}/M_{BC}$ ratio were distinctly high when the air mass originated from the south-southwest (Figures 5-2b, d, f). On average, the $M_{2100}$ and $M_{2100}/M_{BC}$ values during northerly wind periods were respectively ~0.2 μg $m^{-3}$ and ~0.4, becoming 1.0 μg $m^{-3}$ and 3.5, respectively, during south-southwest wind periods. The 1-min $M_{2100}$ data values reached 15 μg $m^{-3}$ when the observation site was downwind with respect to the steel plant. These results confirm that integrated steel plants are significant $FeO_x$ emission sources. Meanwhile, in Tokyo, the wind direction did not significantly affect the $M_{740}$, $M_{BC}$, or $M_{740}/M_{BC}$ values (Figures 5-2a, c, e). This finding implies that $FeO_x$ abundance at the Tokyo observation site, which is 20–40 km northwest of the steel plants and ~10 km north of the power plant, is attributable to emissions of $FeO_x$ from other local human activities.

I further investigate this issue by analyzing the diurnal variations in $M_{740}$, $M_{BC}$, and $M_{740}/M_{BC}$. The diurnal variations in the median values of $M_{740}$, $M_{BC}$, and $M_{740}/M_{BC}$ in Tokyo

are shown in Figure 5-3. These median values in the summer and in the winter generally showed similar diurnal variations. $M_{740}$ values were the lowest in the early morning, becoming higher in the daytime; $M_{BC}$ values were the lowest at midnight and in the early morning, becoming higher in the daytime. These results suggest that $FeO_x$ and BC abundances in Tokyo were largely affected by emissions from local human activities. Diurnal variations in Chiba were not clear (not shown), partly because $FeO_x$ emissions from the steelworks affected the data. Blast furnaces of steel plants generally run 24 hours a day, thereby potentially overprinting and obliterating any otherwise detectable diurnal variation.

In Tokyo, approximately 40% of the BC emissions in 2011 were attributable to emissions from vehicles with diesel engines [*Kondo et al*., 2012]. As discussed, motor vehicle exhaust and brake wear are two important candidate $FeO_x$ emission sources [*Liati et al.*, 2015, *Kukutschová et al.*, 2011]. Therefore, diurnal variations in the $M_{740}/M_{BC}$ ratio might reflect diurnal variations in the traffic number proportion of vehicles with diesel engines. The diurnal variations in the typical traffic numbers of various types of vehicles in Tokyo are shown in Figure 5-3d. Here, the data from the traffic statistics for the boundaries of Tokyo and its neighboring prefectures on 12 November 2014, reported by the Tokyo Metropolitan Police Department (http://www.keishicho.metro.tokyo.jp/about_mpd/jokyo_tokei/tokei_jokyo/ryo.html) was used. The traffic data used here represent typical diurnal variations in the number of vehicles; their year-to-year variations are not significant. I assumed that the vehicles with diesel engines are both light-duty trucks and heavy-duty vehicles. The diurnal variation in the traffic number ratio is plotted in Figure 5-3c; it was well correlated with the diurnal variation in the median $M_{740}/M_{BC}$ ratio ($R^2$ = 0.71 for summer and $R^2$ = 0.48 for winter). These results suggest that motor vehicles may be the major emission sources of $FeO_x$ in Tokyo. To confirm, exhaust gas from a tailpipe of gasoline-driven vehicle was introduced to the SP2. Figure 5-4 shows a scatter plot of color ratio for particles in the exhaust gas, showing a $FeO_x$-like distribution (color ratio

~ 1.5) in addition to a BC-like distribution (color ratio ~ 2). This result also suggests that $FeO_x$ and BC aerosols are both emitted from vehicles, and that vehicles are a possible key source of anthropogenic $FeO_x$ aerosols. Further experimental studies for quantifying the emission fluxes from motor vehicles, including engine combustion and brake wear, are important because currently reported emission strengths of anthropogenic $FeO_x$ aerosols from vehicle are significantly lower than that for coal combustion, or even not considered [*Wang et al*., 2015, *Luo et al.,* 2008].

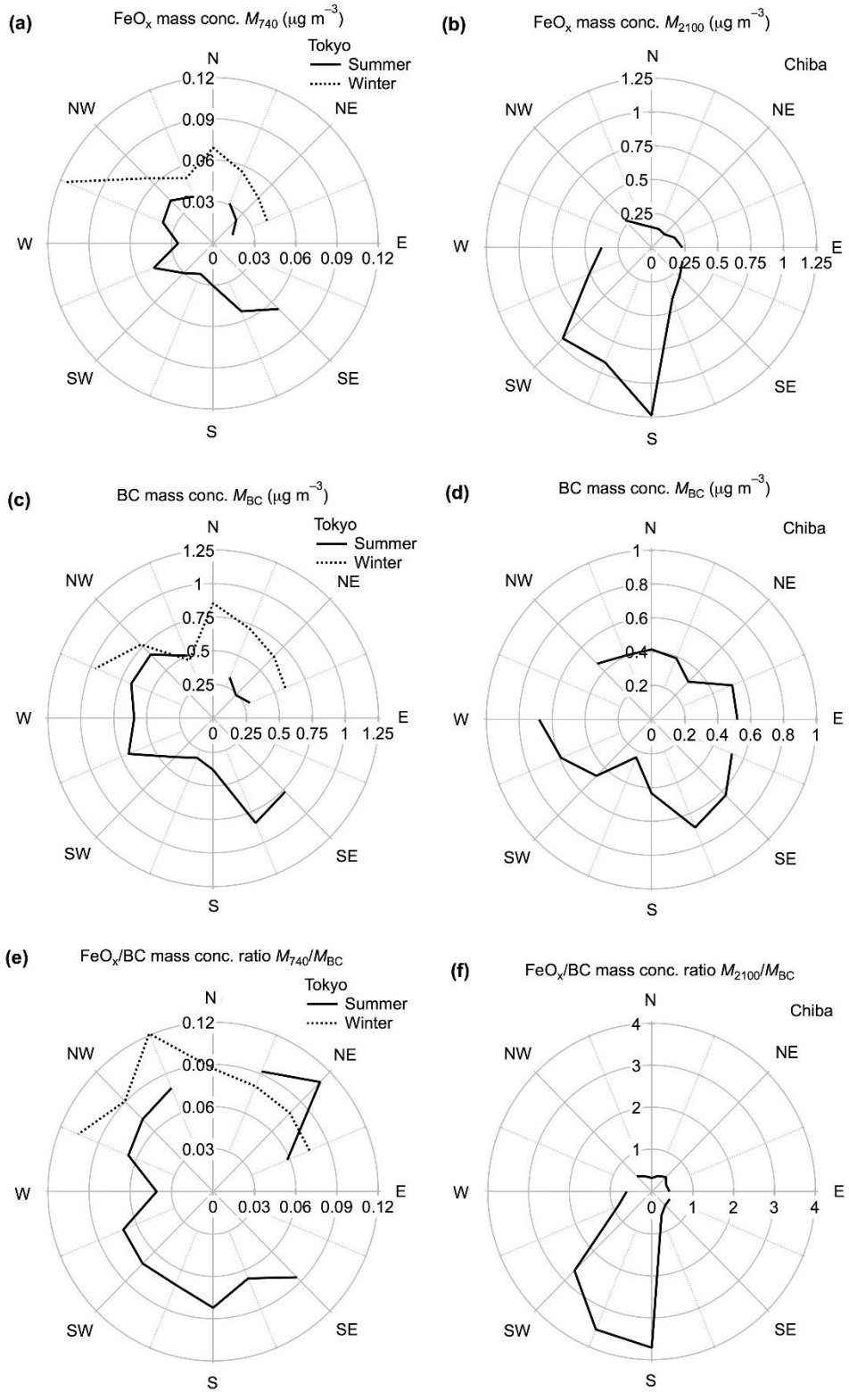


**Figure 5-2.** Wind direction dependences of mass concentrations of $FeO_x$ and BC and $FeO_x$/BC mass concentration ratios in Tokyo and Chiba. Average values of the hourly data are shown.

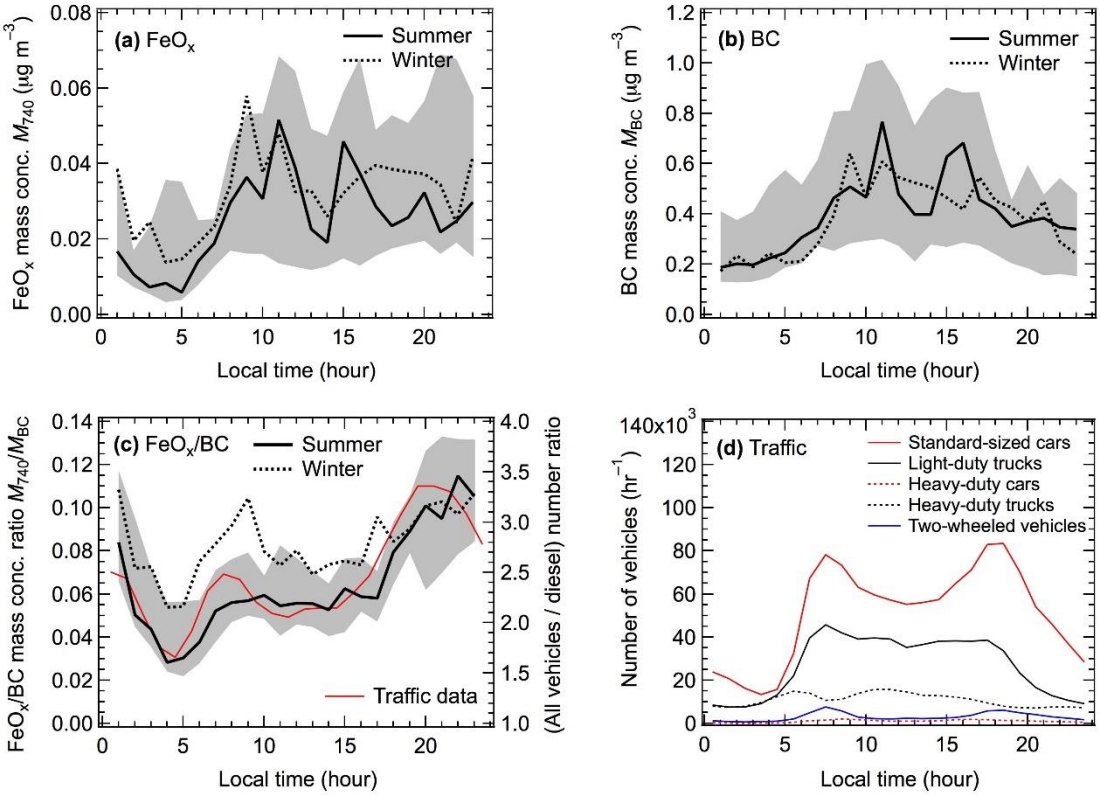


**Figure 5-3.** Diurnal variations (hourly data) of the median mass concentrations of (a) $FeO_x$, (b) BC, and (c) median $FeO_x$/BC mass concentration ratio. (d) The typical traffic number of various types of vehicles in Tokyo. The diurnal variation in the traffic number ratio (all types of vehicles/vehicles with diesel engines) is also shown in panel (c). Shading shows the range of 25–75 percentile values for the Tokyo summer data.

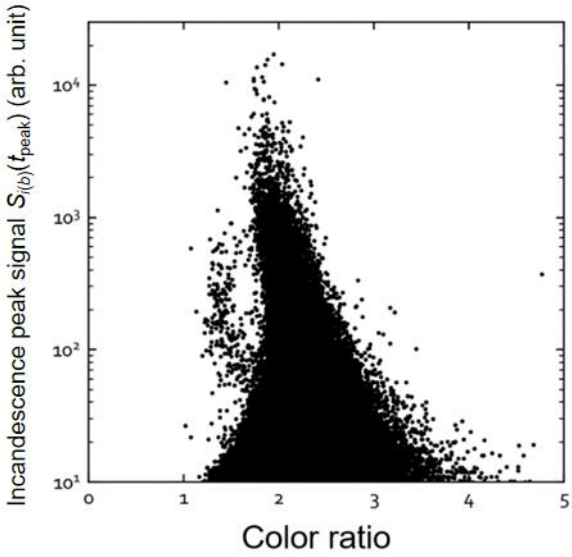


**Figure5-4.** Scatter plot of peak signal of incandescence in the blue band ($S_i$) and color ratio of particles emitted from a gasoline vehicle.

## 5.2 Model simulation for anthropogenic iron aerosols

The measurements of anthropogenic $FeO_x$ aerosols using the developed LII technique provide quantitative data on $FeO_x$ aerosols. Using these data as a constraint, the global abundance of anthropogenic iron aerosols was simulated using a global aerosol transport model by Dr. Matsui [*Matsui et al*., 2018]. In this section, I show some simulated results.

### 5.2.1 Methods

Global aerosol model simulations were conducted for both the present-day (PD) and preindustrial (PI) conditions using two treatments of anthropogenic combustion iron emissions (BASE and NEW). In the BASE simulation, the emission flux of anthropogenic combustion iron in *Luo et al.* (2008), which was estimated by the bottom-up method, was used. In the NEW simulation, iron emission strength from anthropogenic iron sources was tuned by a factor of 5.5 compared with *Luo et al.* (2008) (BASE simulation). This factor was chosen to make the model simulations consistent with the observed $FeO_x$/BC mass ratio (40%) over East Asia (A-FORCE 2013). The factor was applied globally by assuming the same spatial patterns for $FeO_x$ emissions (NEW) and combustion iron emissions from anthropogenic sources in *Luo et al.,* (2008) (BASE).

The size distribution of anthropogenic iron emissions for the NEW simulation is assumed to be a power function fitted to the observed d$N$/dlog$D_m$ for $FeO_x$ aerosols in A-FORCE 2013W (Section 4.3.2),

$$\frac{dN}{dlogD_m} = -0.0395 + 17340D_m^{1.627}, \quad (5\text{-}1)$$

which distribute over a smaller size domain than that for BASE simulation. In the size distribution of anthropogenic iron emission used in the BASE simulation, coarse particles (> 2.5 μm), especially those emitted from coal combustion, significantly contribute to the mass of anthropogenic Fe emission [*Luo et al.,* 2008]. Other simulation settings (e.g., combustion iron

emission from biomass burning sources [*Luo et al.,* 2008], online dust emission scheme [*Matsui* & *Mahowald* 2017, *Ito* 2013, *Wang et al.,* 2015]) are kept constant between the two simulations. This global aerosol model was evaluated previously [*Matsui* & *Mahowald* 2017] other than for $FeO_x$.

When estimating total and soluble iron concentrations and their deposition flux in the NEW simulation, the $FeO_x$ fraction of total iron from anthropogenic sources was assumed to be 40% based on the discussion in Section 3.7. Soluble iron was estimated from the product of total iron and its solubility for each source (anthropogenic (AN), biomass burning (BB), and Dust). The solubility of iron deposited to the global ocean for each source is 7.7%, 11%, and 4.0%, respectively, for AN, BB, and Dust sources [*Bonnet* & *Guieu* 2004, *Hand et al*., 2004, *Chuang et al*., 2005, *Baker* & *Jickells* 2006, *Guieu et al*., 2005, *Sedwick et al*., 2007].

Direct radiative forcings for BC, BrC, and $FeO_x$ were estimated. DRF was calculated for all sky conditions [*Ghan et al.,* 2013] as the difference in direct radiative effect (DRE) between the PD and PI simulations. For BC and $FeO_x$, DRE was defined as the difference in shortwave radiative flux at the top of the atmosphere between when all species were considered vs. when BC or $FeO_x$ was excluded. BrC DRE was defined as the difference in shortwave radiative flux at the top of the atmosphere when all species were considered (i.e., with BrC absorption) vs. when BrC was assumed to be a non-absorbing species (i.e., without BrC absorption).

### 5.2.2 Results

A summary of the simulation is illustrated in Figure 5-5. The emission strength of anthropogenic iron in the NEW simulation is 5.0 times greater than that in the BASE simulation. The emission strength of combustion iron (anthropogenic + BB) in the NEW simulation is 2.5 times greater than that in the BASE simulation.

The average emission lifetime in the NEW simulation is 1.5 times longer than that of the BASE simulation because $FeO_x$ in the NEW simulation has a smaller average particle size (based on A-FORCE 2013 observations). As a result, the atmospheric burden of anthropogenic iron in the NEW simulation is 7.7 times that in the BASE simulation. For comparison, the

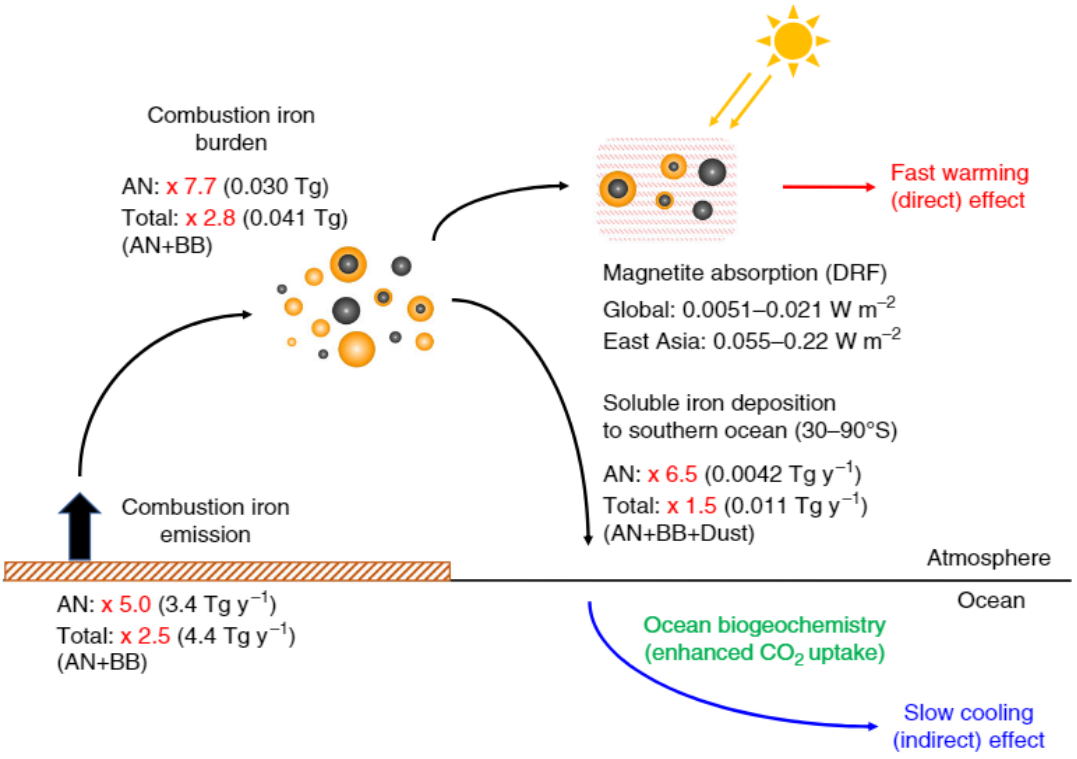


**Figure 5-5.** Schematic figure for the findings of this simulation. The values shown in black are globally or regionally averaged statistics of combustion iron emission and burden, magnetite direct radiative forcing (DRF), and soluble iron deposition flux to the southern ocean in the NEW simulation for anthropogenic sources (AN) and for all sources (Total). The values shown in red are enhancement ratios in the NEW simulation from the BASE simulation

simulated burden is compared with observational data obtained from the SP2 measurement. Table 5-1 shows simulation results for the $FeO_x$/BC mass ratio at SP2 measurement observation sites. The simulation result was spatially and temporally averaged to match each observation location and term. Although only the measured $FeO_x$/BC ratio obtained in A-FORCE 2013 was used to tune the emission strength, all simulated ratios agree with observed ratios within a factor of ~3, and the sign of the model bias was randomly changed without any regional tendency. This result implies that the model's assumption of anthropogenic $FeO_x$ emission in NEW simulation might be able to represent the important feature of region-dependent $FeO_x$ emission strength in reasonable accuracy.

The global mean DRF of anthropogenic $FeO_x$ is 0.0051 W $m^{-2}$ in the NEW simulation. The magnitude of $FeO_x$ DRF depends on the accuracy of the BC DRF because the $FeO_x$/BC ratio was used for estimating magnetite emissions. The BC DRF in this simulation (0.13 W $m^{-2}$) is within the range of estimates from other global aerosol models [*Myhre et al*., 2013,

**Table 5-1.** Simulated and observed $FeO_x$/BC mass concentration ratios.

| | Simulation | Observation | Simulation/Observation |
|---|---|---|---|
| A-FORCE 2009 (dry PBL) | 0.33 | 0.17 | 1.9 |
| A-FORCE 2013W (dry PBL) | 0.38 | 0.36 | 1.1 |
| Hedo | 0.37 | 0.26 | 1.4 |
| Fukue | 0.23 | 0.40 | 0.58 |
| Tokyo | 0.18 | 0.37 | 0.50 |
| Chiba | 0.19 | 0.54 | 0.35 |
| Ny-Ålesund | 0.21 | 0.18 | 1.2 |
| PAMARCMiP 2018 | 0.19 | 0.28 | 0.65 |

*Samset et al*., 2014]. However, this BC DRF is 4–7 times smaller than observationally constrained BC DRF estimates, likely due to an underestimate in emissions of BC [*Bond et al.,* 2013, *Myhre et al*., 2013]. When assuming a similar underestimation of DRF for magnetite, the global mean DRF of anthropogenic $FeO_x$ is 0.021 W $m^{-2}$ (4 times of the NEW simulation). In the estimation, the global mean DRF of anthropogenic $FeO_x$ (0.0051–0.021 W $m^{-2}$) is smaller than that of BrC (0.016–0.038 W $m^{-2}$), which was estimated from the refractive index for moderately and strongly absorbing BrC [*Feng et al.,* 2013]. However, these DRF values for $FeO_x$ and BrC may be comparable within their uncertainty ranges; the maximum DRF for anthropogenic magnetite is 0.021 W $m^{-2}$, while the DRF based on moderately absorbing BrC is 0.016 W $m^{-2}$.

For AN, BB, and Dust sources, the deposition fluxes of soluble iron to the global ocean are 0.012, 0.039, and 0.77 Tg $y^{-1}$, respectively, in the BASE simulation. The soluble iron deposition fluxes for AN and BB sources (BASE simulation) are generally consistent with previous estimates [*Ito* 2015, *Scanza* 2016]. The deposition flux of total (AN+BB+Dust) soluble iron in the NEW simulation exceeds that of the BASE simulation by 12% across the global ocean, and by 52% across the mid- and high-latitudes (30–90 °S) in the southern ocean (Figure 4-15). In particular, the deposition flux of AN soluble iron exceeds that of the BASE simulation by 550% in the southern ocean. The contribution of AN iron to the total soluble iron deposition flux increases from 9.2% (BASE) to 39% (NEW) over the southern ocean. This updated contribution is greater than those of BB and Dust iron sources, respectively 34% and 27%. In the BASE simulation, the contribution of AN iron to total soluble iron deposition flux is less than 10% across the global ocean, while BB and Dust are the major sources of soluble iron deposition at the ocean surface. The reason for highlighting the contribution of deposition by anthropogenic iron in the southern ocean is because the longer anthropogenic iron lifetime than in previous simulations enables longer transport from emission sources to the remote southern ocean.

This simulation result indicates that AN iron is an important source for soluble iron deposition, especially in the southern ocean. However, observations of $FeO_x$ aerosols over the southern ocean remain lacking. Because the southern ocean is the largest HNLC region in the global ocean, further measurements are important for understanding the role of iron aerosols in ocean biogeochemistry and the global carbon cycle.

## References


Bond, T., Streets, D., Yarber, K., Nelson, S., Woo, J., & Klimont, Z. (2004), A technology-based global inventory of black and organic carbon emissions from combustion, *J Geophys Res Atmospheres 1984 2012*, *109*(D14), doi:10.1029/2003jd003697.

Bonnet, S., & Guieu, C. (2004). Dissolution of atmospheric iron in seawater. *Geophysical Research Letters*, *31*(3).

Chuang, P. Y., Duvall, R. M., Shafer, M. M., & Schauer, J. J. (2005). The origin of water soluble particulate iron in the Asian atmospheric outflow. *Geophysical Research Letters*, *32*(7).

Feng, Y., Ramanathan, V., & Kotamarthi, V. R. (2013). Brown carbon: a significant atmospheric absorber of solar radiation?. *Atmospheric Chemistry and Physics*, *13*(17), 8607-8621.

Flament, P., Mattielli, N., Aimoz, L., Choël, M., Deboudt, K., de Jong, J., ... & Weis, D. (2008). Iron isotopic fractionation in industrial emissions and urban aerosols. *Chemosphere*, *73*(11), 1793-1798.

Ghan, S. J. (2013). Estimating aerosol effects on cloud radiative forcing. *Atmospheric Chemistry and Physics*, *13*(19), 9971-9974.

Guieu, C., Bonnet, S., Wagener, T., & Loÿe-Pilot, M. D. (2005). Biomass burning as a source of dissolved iron to the open ocean?. *Geophysical Research Letters*, *32*(19).

Hand, J. L., Mahowald, N. M., Chen, Y., Siefert, R. L., Luo, C., Subramaniam, A., & Fung, I. (2004). Estimates of atmospheric-processed soluble iron from observations and a global mineral aerosol model: Biogeochemical implications. *Journal of Geophysical Research: Atmospheres*, *109*(D17).

Ito, A. (2015). Atmospheric processing of combustion aerosols as a source of bioavailable iron. *Environmental Science & Technology Letters*, *2*(3), 70-75.

Kondo, Y., Ram, K., Takegawa, N., Sahu, L., Morino, Y., Liu, X., & Ohara, T. (2012). Reduction of black carbon aerosols in Tokyo: Comparison of real-time observations with emission estimates. *Atmospheric Environment*, *54*, 242-249.

https://doi.org/10.1016/j.atmosenv.2012.02.003

Kutchko, B., & Kim, A. (2006). Fly ash characterization by SEM–EDS, *Fuel*, *85*(17-18), 2537-2544, doi:10.1016/j.fuel.2006.05.016

Liati, A., Pandurangi, S. S., Boulouchos, K., Schreiber, D., & Dasilva, Y. A. R. (2015). Metal nanoparticles in diesel exhaust derived by in-cylinder melting of detached engine fragments. *Atmospheric environment*, *101*, 34-40.

Luo, C., Mahowald, N., Bond, T., Chuang, P., Artaxo, P., Siefert, R., Chen, Y., & Schauer, J. (2008). Combustion iron distribution and deposition, *Global Biogeochemical Cycles*, *22*(1), doi:10.1029/2007GB002964

Matsui, H., & Mahowald, N. (2017). Development of a global aerosol model using a two-dimensional sectional method: 2. Evaluation and sensitivity simulations. *Journal of Advances in Modeling Earth Systems*, *9*(4), 1887-1920.

Matsui, H., Mahowald, N., Moteki, N., Hamilton, D., Ohata, S., Yoshida, A., Koike, M., Scanza, R. and Flanner, M. (2018). Anthropogenic combustion iron as a complex climate forcer. *Nature Communications*. 9, 1, 1593. doi:10.1038/s41467-018-03997-0

Myhre, G., Samset, B. H., Schulz, M., Balkanski, Y., Bauer, S., Berntsen, T. K., ... & Easter, R. C. (2013). Radiative forcing of the direct aerosol effect from AeroCom Phase II simulations. *Atmospheric Chemistry and Physics*, *13*(4), 1853.

Scanza, R. A. (2016). The impact of resolving mineralogy of dust on climate and biogeochemistry. PhD thesis, Cornell University.

Sedwick, P. N., Sholkovitz, E. R., & Church, T. M. (2007). Impact of anthropogenic combustion emissions on the fractional solubility of aerosol iron: Evidence from the Sargasso Sea. *Geochemistry, Geophysics, Geosystems*, *8*(10).

Wang, R., Balkanski, Y., Boucher, O., Bopp, L., Chappell, A., Ciais, P., Hauglustaine, D., Peñuelas, J., & Tao, S. (2015). Sources, transport and deposition of iron in the global atmosphere, *Atmospheric Chemistry and Physics*, *15*, 6247-6270, doi:10.5194/acp-15-

# 6 General conclusions

This work first reports the concentrations and microphysical properties (size distribution and mixing state) of light-absorbing anthropogenic $FeO_x$ aerosols, in East Asian continental outflow, urban environments, and the Arctic region. For obtaining these $FeO_x$ aerosols observational data, the LII technique was developed and used for short-duration, real-time measurement of $FeO_x$ aerosols.

The developed LII technique using the SP2 establishes quantification of individual $FeO_x$ particles, discriminated from BC. The size-resolved concentration of these $FeO_x$ aerosols can be observed with high time resolution. This is the key novelty of this new method. In addition, the particle's scattering cross section and incandescence onset timing measured by the SP2 can provide information to help determine whether the detected $FeO_x$ particles are anthropogenic or natural.

I used the developed LII technique to detect $FeO_x$ aerosols in Hedo, located in the East Asian continental outflow, in spring 2016. The majority of measured $FeO_x$ aerosols were of anthropogenic origin, based on the quantities measured by the SP2 (incandescence onset position $t_{oi}$ and scattering cross section $C_s(t_{oi})$) and the particle morphologies and compositions analyzed by TEM. The developed LII provides the capability to obtain hourly concentration and size distributions. This time resolution is considerably shorter than the several-day time resolution of conventionally used measurement techniques based on filtration. Data acquisition by the LII technique in such high time resolution provides the capability to obtain statistically significant mass concentration data and to draw clear positive correlations between mass concentrations of $FeO_x$ and BC ($R^2 = 0.717$) and of $FeO_x$ and CO ($R^2 = 0.718$) in air masses originating from China. These correlations indicate that the emission sources of $FeO_x$ aerosols are spatially similar to those of BC and CO in China. Based on the correlation between $FeO_x$ and BC, the mass concentration of $FeO_x$ aerosols from China is approximately 30% that of BC.

Based on the slopes of correlation between mass concentrations of $FeO_x$ and BC or CO, emission strengths of anthropogenic $FeO_x$ aerosols were estimated by the top-down method. The annual emission strength of anthropogenic $FeO_x$ aerosols from China was estimated to be 0.49 FeTg/yr. An alternative estimate of 0.21 FeTg/yr was based on the slopes of correlation between mass concentrations of $FeO_x$ and CO.

The developed LII was further used to examine $FeO_x$ aerosols in East Asian continental outflow, urban environments in Japan, and the remote Arctic region through both ground and aircraft measurements. The majority of $FeO_x$ aerosols in all observations were anthropogenic. The shapes of the $FeO_x$ size distributions, especially of the number size distributions, are similar among all observations. The mass concentrations were ~100–400 ng/m$^3$ in the East Asian continental outflow and urban environments but only ~5–25 ng/m$^3$ in the Arctic region. Despite the difference in mass concentration, $FeO_x$/BC mass concentration ratios were within 20–50% for all observation locations. $FeO_x$ concentrations are well correlated with BC and CO concentrations measured in all observations. These results indicate that the $FeO_x$ aerosols have emission sources spatially similar to BC and CO emission sources, and that the $FeO_x$/BC mass ratio ranges from approximately 20% to 50% in the northern hemisphere.

In addition to the concentration and size distribution, the mixing state of $FeO_x$ aerosols can be evaluated using the LII technique. My analysis indicates that the $FeO_x$ aerosols in the northern hemisphere experience atmospheric aging processes, with coating thickness gradually increasing as well as BC. The internal mixing of $FeO_x$ with major acidic aerosol compositions, such as sulfate, can enhance light absorption, promote wet removal in precipitating clouds, and increase the solubility of Fe. Thus, the mixing state of $FeO_x$ aerosols should be represented in chemical transport models to improve the assessment of their effect on atmospheric radiation and ocean biogeochemistry.

In all these ways, the developed LII technique provides quantitative observational data regarding the abundance and microphysical properties of $FeO_x$ aerosols, which can be used for

aerosol transport model simulation of iron aerosols. When the measured $FeO_x$/BC mass concentration ratios and size distributions observed in A-FORCE 2013W were used to constrain the emission of anthropogenic iron aerosols (top-down approach), the constrained emission strength and calculated atmospheric abundance of anthropogenic iron aerosols became respectively 5.0 times and 7.7 times larger than estimates in previous studies, in which no atmospheric iron aerosol observational data of was included [*Luo et al.,* 2008]. Moreover, the simulation suggests that anthropogenic iron aerosol is an important component in soluble iron deposition flux especially over the southern ocean (HNLC region). In addition to deposition flux, the simulation calculated DRF of anthropogenic iron oxide aerosols and showed that this value was comparable to that of BrC. This result suggests that anthropogenic iron oxide aerosols should be considered when evaluating the aerosol-radiation interaction.

Emission strengths of anthropogenic iron aerosols estimated in top-down way using $FeO_x$ measurement data for Hedo (Section 3.6) and the A-FORCE 2013W (Section 5.2) observation campaigns indicate that currently reported bottom-up estimates of emission strength are underestimates. This underestimation could be due to the scarcity of observational studies constraining the Fe content in aerosols from individual emission sources. In addition, missing emission sources of anthropogenic iron aerosols may play a role in underestimation. In fact, $FeO_x$ measurements in Tokyo and Chiba suggest that vehicles are an important source for anthropogenic iron aerosols in urban environments (Section 5.1). Therefore, further measurements constraining emission sources of anthropogenic iron aerosols are important.

Quantitative $FeO_x$ measurement using the developed LII technique, along with further data analysis and model simulation, suggests that emission strength, atmospheric burden, iron deposition flux to the surface ocean, and radiative effect have been underestimated for $FeO_x$. Furthermore, these analyses and simulations suggest that anthropogenic iron aerosols have a more important role on short time scales (radiative effect) and long time scales (global carbon cycle) than previously thought. However, uncertainty remains on these points because of the

following three issues. First, $FeO_x$ observations have been conducted in limited regions and seasons. No $FeO_x$ measurement was conducted over HNLC regions (North Pacific, Equatorial Pacific, and southern ocean). In particular, in the southern ocean, anthropogenic iron aerosols can be more important for soluble iron deposition than iron aerosols from mineral dust and biomass burning (Section 5.2). Thus, it is especially important to measure anthropogenic $FeO_x$ aerosols over the southern ocean. Moreover, it is also necessary to obtain more three-dimensional data of $FeO_x$ aerosols because altitude profiles are important observational data to understand transport and removal processes of aerosol [*e.g. Kondo et al.,* 2016]. Secondly, the current SP2 can measure $FeO_x$ aerosols with $D_m$ < 2100 nm; extrapolated curve fitting to the measured size distribution was used to estimate the abundance of large $FeO_x$ aerosols ($D_m$ > 2100 nm). Thus, extending the detectable size range of $FeO_x$ aerosols is an important challenge. Finally, the mass ratio of $FeO_x$ to total iron, assumed to be 40% in this study (Section 3.7 and 5.2), is based on only a few experiments. To reduce the uncertainty of the ratio of $FeO_x$ to total iron mass, further experiments are needed for various emission sources. In addition, it remains a fundamental challenge to modify the LII technique to measure a wider variety of iron oxide components beyond magnetite and hematite. The current LII technique measures only strongly light-absorbing iron oxides (e.g., magnetite and hematite) that can emit incandescence light in the laser beam. To measure other components, a critical solution could be provided by a light source with more intense power and adequate coverage of wavelengths at which iron oxides efficiently absorb light. The wavelength of the currently used Nd:YAG laser beam is 1064 nm, not an optimal wavelength for light absorption by iron oxide, especially hematite and goethite (Figure 2-4). To confirm this deficiency, I constructed an optical system using a high-power visible laser beam to measure incandescent light from various iron oxides, resulting in success in detecting goethite particles, which are not measured by the SP2. Thus, modifying the light sources in the LII technique can reduce uncertainties in the mass ratio of $FeO_x$ to total iron. Moreover, this modification probably would help refine the measurement of large $FeO_x$

particles ($D_m$ > 2100), since the upper limit of the size range is due mainly to the inability of the current light source to generate sufficient heat in large particle to cause it to emit incandescent light. Furthermore, this modification is important for measuring natural iron oxide (mineral dust) in addition to anthropogenic iron oxide because goethite is the major iron oxide component of natural iron. Current measurement techniques for mineral dust aerosols are based on filtration, which is the critical reason why no previous study has used a top-down method to report on the emission strength of natural iron aerosols. Therefore, further modification of the LII technique and further measurements of atmospheric iron oxide aerosols will improve our understanding of the atmospheric abundance of anthropogenic and natural iron aerosols and their impact on climate on short time scales (atmospheric radiation) and long time scales (global carbon cycle).

## References

Kondo, Y., Moteki, N., Oshima, N., Ohata, S., Koike, M., Shibano, Y., ... & Kita, K. (2016). Effects of wet deposition on the abundance and size distribution of black carbon in East Asia. *Journal of Geophysical Research: Atmospheres*, *121*(9), 4691-4712.

Luo, C., Mahowald, N., Bond, T., Chuang, P., Artaxo, P., Siefert, R., Chen, Y., & Schauer, J. (2008). Combustion iron distribution and deposition, *Global Biogeochemical Cycles*, *22*(1), doi:10.1029/2007GB002964

# Acknowledgments

I would like to thank my supervisor Prof. M. Koike at the University of Tokyo for his consistent and kind support. I am also deeply grateful to Dr. N. Moteki at the University of Tokyo for his dedicated guidance and support. I am also thankful to Dr. S. Ohata at the Nagoya University for discussion, advice and technical supports on my study. I would like to thank all co-workers in the aerosol measurement campaigns for their support. Special thanks are given to my colleagues: Y. Ozawa, T. Mori, C. Ong, S. Yamaguchi, T. Iwata, Y. Takasago, R. Yasui, K. Fukuzawa, S. Kido, Y. Minamihara, A. Takahashi, M. Kurisu, and. C. Miyamoto. Finally, I would like to thank my family and friends for generous and considerable support in this very intense academic year.

# Publication list

**Yoshida, A.**, Moteki, N., Ohata, S., Mori, T., Tada, R., Dagsson-Waldhauserová, P. & Kondo, Y. (2016). Detection of light-absorbing iron oxide particles using a modified single-particle soot photometer, *Aerosol Science and Technology* (*Aerosol Research Letter*), 50, i-iv

Moteki, N., Adachi, K., Ohata, S., **Yoshida, A.**, Harigaya, T., Koike, M. & Kondo, Y., Anthropogenic iron oxide aerosols enhance atmospheric heating (2017). *Nature Communications*, doi10.1038/ncomms15329, 2017

Matsui, H., Mahowald, N., Moteki, N., Hamilton, D., Ohata, S., **Yoshida, A.**, Koike, M., Scanza, R. & Flanner, M. (2018). Anthropogenic combustion iron as a complex climate forcer. *Nature Communications*. 9, 1, 1593. doi:10.1038/s41467-018-03997-0

Ohata, S., **Yoshida, A**., Moteki, N., Adachi, K., Takahashi, Y., Kurisu, M., & Koike, M. (2018). Abundance of light-absorbing anthropogenic iron oxide aerosols in the urban atmosphere and their emission sources. *Journal of Geophysical Research: Atmospheres*, 123,8115−8134. https://doi.org/10.1029/2018JD028363

**Yoshida, A.**, Ohata, S., Moteki, N., Adachi, K., Mori, T., Koike, M., & Takami, A. (2018). Abundance and emission flux of the anthropogenic iron oxide aerosols from the East Asian continental outflow. *Journal of Geophysical Research: Atmospheres*, 123. https://doi.org/10.1029/2018JD028665

**Yoshida, A.**, Moteki, N., Ohata, S., Mori, T., Koike, M., Kondo, Y., Matsui, H., Oshima, N., Takami, A., & Kita, K. (under review in *Journal of Geophysical Research: Atmospheres*). Abundances and microphysical properties of light-absorbing iron oxide and black carbon aerosols over East Asia and the Arctic